Chapter 1

Modification of the Electromagnetic Field in the Photonic Crystal Medium and New Ways of Applying the Photonic Band Gap Materials

Renat Gainutdinov, Marat Khamadeev,
Albert Akhmadeev and Myakzyum Salakhov

Additional information is available at the end of the chapter

http://dx.doi.org/10.5772/intechopen.71367

Abstract

Photonic crystals (PCs) are periodic systems that consist of dielectrics with different refractive indices. Photonic crystals have many potential technological applications. These applications are mainly based on the photonic bang gap effect. However the band gap is not only effect that follows from the periodic changing of the refractive index in the photonic crystal. The periodic change of the photon-matter interaction in photonic crystal medium gives rise to the fact that the mass of an electron in the photonic crystal must differ from its mass in vacuum. Anisotropy of a photonic crystal results in the dependence of the electromagnetic mass correction on the orientation of the electron momentum in a photonic crystal. This orientation dependence in turn gives rise to the significant correction to the transition frequencies in an atom placed in air voids of a photonic crystal. These corrections are shown to be comparable to the atomic optical frequencies. This effect allows one to control the structure of the atomic energy levels and hence to control resonance processes. It can serve as the basis for new line spectrum sources. The effect provides new ways of realization of quantum interference between decay channels that can be important for quantum information science.

Keywords: photonic crystals, electron mass, anisotropic vacuum, electromagnetic field, Lamb shift

1. Introduction

Photonic crystals (PCs) are a major field of research having many potential applications [1–15]. These applications are mainly based on the photonic bang gap effect in the photonic crystal. In Ref. [16], it has been shown that a strong modification of the electromagnetic interaction in photonic crystals results in the fact that the electron mass changes its value. Actually in this

case, we deal with a quantum electrodynamical (QED) effect that does not manifest itself in the free space. In fact, the interaction of an electron with its own radiation field gives rise to a contribution to its physical mass m_{ph} known as the electromagnetic mass of the electron m_{em}. Nonrenormalizable ultraviolet divergences do not allow one to calculate the electron electromagnetic mass. However, fortunately, only physical mass m_{ph} is observable, and hence m_{em} can be included into it. On the other hand, the modification of the electromagnetic interaction in PC medium gives rise to a correction to the electromagnetic mass m_{em}. This correction δm_{pc} cannot be hidden in the physical mass of the electron and hence is an observable. Thus in PC medium, the novel observable δm_{pc} comes into play. A remarkable feature of δm_{pc} is its dependence on the orientation of the electron momentum in a PC, and this dependence gives rise to significant corrections to the transition frequencies in an atom placed in air voids of a photonic crystal, being comparable to the ordinary atomic frequencies. Such an effect is a consequence of the fact that in the case of atoms in the PC medium, the most contribution comes from the self-energy of electrons associated with mass correction m_{em}^{pc} rather than from the self-energy of atoms associated with the Lamb shift being the QED corrections to the nucleus-electrons coupling. In this chapter, we discuss the origins of the effect of the change in the electron mass caused by the modification of the electromagnetic interaction in a PC and its possible applications.

2. Lamb shift in hydrogen atom in the free space

The processes of the interaction of charged particles with their own radiation field play the important role in the modern physics. These processes give rise to the fact that actually we deal with the particles dressed by a cloud consisting of virtual particles (photons, electron-positron pairs, and so on). In the case of electrons or muons bound to an atomic nucleus, the self-interaction results in the Lamb shift of the atomic energy levels. The results of the recent measurements of the Lamb shift in muonic hydrogen [17, 18] have allowed to determine the value of the root-mean-square charge radius of the proton r_p which is 4% smaller than the radius determined by electron-proton experiments [19, 20] and precision spectroscopy of the ordinary atomic hydrogen [21–27]. This discrepancy known as the "proton radius puzzle" has not been explained yet. Solving the puzzle may require new insights into the problem of the description of the self-energy of the electron and the Lamb shift.

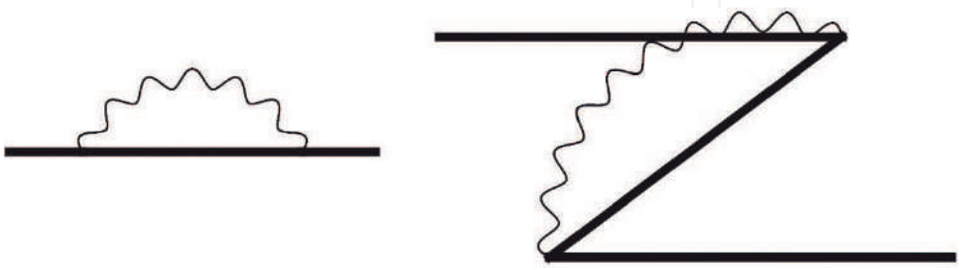

Figure 1. The time-ordered diagrams describing the dominant contribution to the Lamb shift. The thick line denotes the electron (positron) propagating in the Coulomb field; the wavy line denotes emission and reabsorption of a virtual photon.

http://dx.doi.org/10.5772/intechopen.71367

The Lamb shift consists of the self-energy and vacuum polarization contributions. The modification of the vacuum polarization contribution in the PC medium is negligible, and for this reason, we will focus only on the self-energy one. At leading order self-energy of the electron, which is bound in a hydrogen-like atom, is defined by the process in which a photon is emitted and then is reabsorbed by the electron or positron. This process is described by the time-ordered diagrams in **Figure 1**.

In quantum electrodynamics the corresponding contribution to the Lamb shift in hydrogen-like atoms is given by the term that appears in the second-order perturbation theory and in the Furry picture can be written as

$$\Delta E_{L,n} = \langle n|H_I \frac{1}{E_n^{(0)} - H_0^F} H_I|n\rangle, \tag{1}$$

where H_0^F is the unperturbed Dirac-Coulomb Hamiltonian in the Furry picture ($H_0^F|n\rangle = E_n^{(0)}|n\rangle$), $|n\rangle$ is an atomic state, and

$$H = H_0 + \int d^3x H_I(t=0,\mathbf{x}), \tag{2}$$

with $H_I(t,\mathbf{x})$ being the interaction Hamiltonian density:

$$H_I(t,\mathbf{x}) = \frac{e}{2} A_\mu(t,\mathbf{x}) \left[\overline{\Psi}(t,\mathbf{x}), \gamma^\mu \Psi(t,\mathbf{x})\right]. \tag{3}$$

Here $\Psi(x)$ is the Dirac field in the Furry picture. Usually the contributions to the Lamb shift (1) are separated into the low and high energy parts. For the reasons explained bellow, we will focus on the low-energy part of the shift [28]:

$$\Delta E_{L,n}^{<} = \frac{2\pi\alpha}{3m_e^2} \int_0^\Lambda \frac{d^3k}{2|\mathbf{k}|(2\pi)^3} \sum_m \frac{|\langle n|\mathbf{p}|m\rangle|^2}{E_n - |\mathbf{k}| - E_m}, \tag{4}$$

where $\mathbf{p}$ is the operator of the electron momentum and the cutoff Λ limits the energies of virtual photons in the processes of their emission and reabsorption. The cutoff must be much less than typical electron momenta but much larger than the atomic binding energies:

$$(Z\alpha)^2 m_e << \Lambda << (Z\alpha) m_e. \tag{5}$$

Here and below the natural unit system is used, where $\hbar = c = \varepsilon_0 = 1$. This is the reason why one can use the nonrelativistic Hamiltonian:

$$H = \frac{1}{2m_e}[\mathbf{p} - e\mathbf{A}]^2 \tag{6}$$

instead of the Hamiltonian defined in Eqs. (2) and (3). Eq. (4) can be rewritten in the form:

$$\Delta E_{L,n} = -\frac{\Delta m_e^{<}}{2m_e^2}\langle n|\mathbf{p}^2|n\rangle + \Delta E_L^{<}, \tag{7}$$

where

$$\Delta m_e^{<} = \frac{\alpha}{p^2\pi^2}\sum_{\lambda=1}^{2}\int_0^{\Lambda}\frac{d^3k}{2|\mathbf{k}|^2}|\mathbf{p}\cdot\varepsilon_\lambda(\mathbf{k})|^2 \tag{8}$$

is the low-energy electron mass correction caused by its self-interaction [29]. It should be noted that $\Delta E_{L,n}$ does not contain a term describing the electromagnetic correction to the electron mass. This is the result of making use of the nonrelativistic Hamiltonian (6), and for this reason, the mass correction is extracted from the first term on the right-hand part of Eq. (7) describing the correction to the kinetic energy. Thus, in this case the electromagnetic mass correction is regarded to be included into the physical mass of the electron. The first term on the right-hand part of Eq. (7) must be also included into the physical mass. In this way we arrive at the ordinary expression for the low-energy Lamb shift in hydrogen-like atoms:

$$\Delta E_{L,m}^{<} = \frac{\alpha}{6\pi^2 m_e^2}\sum_m\int_0^{\Lambda}\frac{d^3k}{2|\mathbf{k}|^2}\,\frac{|\langle n|\mathbf{p}|m\rangle|^2}{E_n - |\mathbf{k}| - E_m}(E_n - E_m). \tag{9}$$

Adding to $\Delta E_L^{<}$ the high energy contribution [28]:

$$\Delta E_L^{>} = \frac{4\alpha}{3}\frac{Z\alpha}{m^2}\left|\Psi_{nlmj}(0)\right|^2\left(\ln\frac{m_e}{2\Lambda} + \frac{11}{24} - \frac{1}{5}\right), \tag{10}$$

where n, l, m, j, and $\Psi_{nlmj}(x)$ being, respectively, the main quantum number, orbital quantum number, magnetic quantum number, inner quantum number, and the wave function, we get the expression to the total Lamb shift of the energies of the states of the hydrogen-like atoms. In the S-state it reads

$$\Delta E_{L,n} = \frac{4\alpha(Z\alpha)^4}{3\pi n^2}\left(\ln\frac{m_e}{2\overline{E}} + \frac{11}{24} - \frac{1}{5}\right)m_e + o(Z\alpha)^4, \tag{11}$$

where $\overline{E} = \alpha^2 m_e$.

3. The Lamb shift in atoms placed in a PC

Investigation of the Lamb shift in hydrogen atom placed in a PC attracts much attention for a long time since the Lamb shift is (historically and in practice) the most important phenomenon of quantum electrodynamics. Interestingly, the calculation results obtained in different works differed strongly in order of magnitude, and the significance of interaction with vacuum, depending on which model of the dispersion of a photon in a photonic crystal, was used.

The first attempt was made by John and Wang [4] by using the solution of the scalar wave equation in one dimension. Thus, the photon dispersion relation was chosen to be isotropic and satisfy the transcendental equation:

$$4n\cos(kL) = (1+n)^2\cos[(2na+b)\omega_k] - (1-n)^2\cos[(2na-b)\omega_k]. \tag{12}$$

Using this dispersion relation, the authors predicted anomalous Lamb shift affecting the odd-parity $2P_{1/2}$ state and not the even-parity $2S_{1/2}$. Magnitude of the effect makes it detectable using microwave. The fact that the anomalous Lamb shift of the $2P_{1/2}$ state is larger than the ordinary Lamb shift of the $2S_{1/2}$ state originates from the dimension of the phase space occupied by band edge photons of vanishing group velocity. John and Wang overestimated this phase space by assuming that $d\omega_k/dk$ vanishes over the entire sphere $|\mathbf{k}| = \pi/L$. At the same time for the case of real photonic crystals, the shift was expected to be comparable to the ordinary Lamb shift of the $2S_{1/2}$ level.

The authors of work [30] noted that a real photonic crystal in general has an anisotropic structure in momentum space and a three-dimensional dispersion relation is required because the density of states (DOS) in isotropic or one-dimensional case has a singularity near band edge. In this study the atomic transition frequency ω is assumed to be near the band edge ω_c and the dispersion relation was approximated by the expression.

$$\omega_k = \omega_c + A\left|\mathbf{k} - \mathbf{k}_0^i\right|^2, \tag{13}$$

where A is a model-dependent constant and $\mathbf{k}_0^i$ is a finite set of symmetrically placed points leading to a three-dimensional band structure. Using this model the Schrödinger equation was solved, and analytical expression for the Lamb shift was obtained. The value of the Lamb shift turned out to be smaller than that for a hydrogen atom in an ordinary vacuum. Authors explained this result by the fact that the DOS in the photonic crystals with three-dimensional dispersion relations is much lower than that in the ordinary vacuum. This result is also very different from that from the one-dimensional case where DOS has a singularity or from the two-dimensional case where DOS has a sudden jump.

In paper [31] all previous approaches to calculate Lamb shift in photonic crystal were criticized, because they are basically scalar. Authors of this work demonstrated the rigorous solution of the problem of calculation of the Lamb shift in atomic hydrogen in a 3D photonic crystal and showed that the presence of a photonic band gap (PBG) at optical wavelengths can hardly change the Lamb shift. The correction to the energy of electronic state $|m\rangle$ was calculated in the second order of perturbation theory. The quantization of EM fields in a 3D photonic crystal was made by expanding the EM fields in a set of eigenmodes (Bloch states). These states can be solved numerically by means of a plane-wave expansion method. Finally, it was given an expression for the energy shift containing the local density of states (LDOS):

$$\Delta\mathrm{E} = \frac{e^2\hbar}{u_0^2 m_e^2}\sum_n E_{nm}\left|p_{mn}\right|^2\int_0^\infty d\omega\,\frac{\rho(\omega,\mathbf{r})}{\omega^3(E_{nm}+\hbar\omega)}, \tag{14}$$

with $\rho(\omega, \mathbf{r})$ being LDOS:

$$\rho(\omega, \mathbf{r}) = \frac{u_0^2 c^2}{2\hbar\varepsilon_0 (2\pi)^3 \varepsilon^2(\mathbf{r})} \sum_n \int_{BZ} d^3k \frac{|\nabla \times \mathbf{H}_{n\mathbf{k}}(\mathbf{r})|^2}{3\omega_{n\mathbf{k}}} \delta(\omega - \omega_{n\mathbf{k}}), \tag{15}$$

where u_0 is dipole moment, $\varepsilon(\mathbf{r})$ is dielectric constant function, and $\mathbf{H}_{n\mathbf{k}}(\mathbf{r})$ is magnetic field distribution of the Bloch states with energy $\hbar\omega_{n\mathbf{k}}$. The authors estimated the magnitude of the Lamb shift and concluded that PBG at optical wavelengths will not cause an appreciable variation to the energy-level shift induced by self-interaction for different atom positions and different variations of the LDOS.

Vats with colleagues used the anisotropic band edge model and pseudogap model to calculate the Lamb shift in an atom placed in photonic crystal [32]. In the first case near the band edge, dispersion relation (13) was used and corresponding DOS derived. Calculated Lamb shift was an order of magnitude larger than the free space Lamb shift. Then authors treated the case of a pseudogap, for which the stop band does not extend over all propagation directions, thus resulting in a suppression of the DOS rather than the formation of a full PBG:

$$N(\omega) = \omega^2 \left[1 - h\exp\left(-\frac{(\omega - \omega_0)^2}{\Gamma^2} \right) \right]. \tag{16}$$

Here, h and Γ are parameters describing the depth and width of the pseudogap, respectively, and ω_0 is the central frequency of the pseudogap. Vats with coworkers concluded that for a sufficiently strong pseudogap, the maximal value of Lamb shift may be on the order of 15% of the free space value.

The authors of work [33] using method of Green functions developed a general formalism for calculating the Lamb shift in multilevel atoms. The radiative correction to the bound level l is determined by the expression

$$\omega - \omega_l = \sum_j \frac{\alpha_{lj}}{2\pi} (\omega - \omega_j) \beta(\mathbf{r}, \omega - \omega_j), \tag{17}$$

where

$$\alpha_{lj} = \frac{e^2 \left| \mathbf{p}_{lj} \right|^2}{3\pi m_e^2 \varepsilon_0 \hbar c^3} \tag{18}$$

is the relative linewidth of the atomic radiation from the l state to the j state in vacuum

$$\beta(\mathbf{r}, \omega - \omega_j) = P \int_0^{m_e c^2/\hbar} d\omega' \frac{g(\mathbf{r}, \omega')}{(\omega - \omega_j - \omega')\omega'}. \tag{19}$$

The function $g(\mathbf{r}, \omega)$ is the local spectral response function (LSRF) proportional to the photon LDOS:

$$g(\mathbf{r},\omega)=\frac{c^3V_{pc}}{2\pi\omega}\sum_n\int_{BZ}d^3k|\mathbf{E}_{n\mathbf{k}}(\mathbf{r})|^2\delta(\omega-\omega_{n\mathbf{k}}) \tag{20}$$

with V_{pc} being the PC volume and $\mathbf{E}_{n\mathbf{k}}(\mathbf{r})$ being the electromagnetic eigenmodes. Authors revealed that in a 3D PC, real photons make a dominant contribution to the value of the Lamb shift, while the contribution from interaction with virtual photons is small. This differs significantly from the free space case. It was shown that the PC structure can lead to a giant Lamb shift, that is, up to two orders of magnitude larger than that for an ordinary vacuum [34]. The Lamb shift is sensitive to both the position of an atom in PCs and the transition frequency of the related excited level.

4. Photonic crystal medium corrections to the electron rest mass

For a long time in investigations of QED effects in the PC medium, researches focused on study of the Lamb shift in hydrogen atom placed in a PC. In all the listed studies, the subtraction of the modified by PC medium self-energy of the free electron from the modified self-energy of the bound electron was used. This procedure was correct, if this self-energy could be included into the electron physical mass. However this is not the case, because the electromagnetic mass of the electron in a PC differs from that in the free space and cannot be hidden in the physical mass. In fact

$$m_{em}^{pc}=m_{em}+\delta m_{pc} \tag{21}$$

and hence the total electron mass m_e^{pc} in a PC is

$$m_e^{pc}=m_e+\delta m_{pc}. \tag{22}$$

Thus, the modification of the interaction of the electron with its own radiation field in the PC medium results in the change in its mass. Let us now determine the mass correction δm_{pc}. For this we have to generalize our analysis of the electron self-energy to the case where it is in the PC medium. It is natural to start from determining of a quantized vector potential of electromagnetic field inside PC. It could be made by taking into account that photon states in periodic dielectric media have Bloch structure. Photonic Bloch states $|\mathbf{k}n\rangle$ can be obtained by means of the plane-wave expansion method [35]. By introducing the operators $\widehat{a}_{\mathbf{k}n}^{+}$ and $\widehat{a}_{\mathbf{k}n}$ that describe the creation and annihilation of the photon in the state $|\mathbf{k}n\rangle$, respectively ($\widehat{a}^{\mathbf{k}n+}|0\rangle=|\mathbf{k}n\rangle$ and $\widehat{a}_{\mathbf{k}n}|\mathbf{k}n\rangle=|0\rangle$), we can construct a modified vector potential:

$$\mathbf{A}_{pc}(\mathbf{r},t)=\sum_{\mathbf{k}n}\left[\mathbf{A}_{\mathbf{k}n}(\mathbf{r})\widehat{a}_{\mathbf{k}n}e^{-i\omega_{\mathbf{k}n}t}+\mathbf{A}_{\mathbf{k}n}^{*}(\mathbf{r})\widehat{a}_{\mathbf{k}n}^{+}e^{i\omega_{\mathbf{k}n}t}\right], \tag{23}$$

where $\mathbf{A}_{\mathbf{k}n}(\mathbf{r})=\sqrt{1/V\omega_{\mathbf{k}n}}\mathbf{E}_{\mathbf{k}n}(\mathbf{r})$ with $\mathbf{E}_{\mathbf{k}n}(\mathbf{r})$ being the Bloch eigenfunctions satisfying the following orthonormality condition:

$$\int_V d^3r\varepsilon(\mathbf{r})\mathbf{E}_{\mathbf{k}n}(\mathbf{r})\mathbf{E}^*_{\mathbf{k}'n'}(\mathbf{r}) = V\delta_{\mathbf{k}\mathbf{k}'}\delta_{nn'}. \tag{24}$$

Using vector potential (23) we can define nonrelativistic interaction Hamiltonian in the form

$$H_I^{pc} = -\frac{e}{m_e}\mathbf{p}\cdot\mathbf{A}_{pc}. \tag{25}$$

The matrix element $\langle \mathbf{p}'; \mathbf{k}, n|H_I^{pc}|\mathbf{p}\rangle$ of this Hamiltonian can be represented in the form

$$\langle \mathbf{p}'; \mathbf{k}, n|H_I^{pc}|\mathbf{p}\rangle = -\frac{e}{m_e}\int d^3r\Psi^*_{\mathbf{p}'}(\mathbf{r})(-i\nabla_{\mathbf{r}}\mathbf{A}_{\mathbf{k}n}(\mathbf{r}))\Psi_{\mathbf{p}}(\mathbf{r}) = \frac{e}{m_e V^{3/2}\sqrt{\omega_{\mathbf{k}n}}}\int d^3re^{-i\mathbf{p}'\mathbf{r}}(i\nabla_{\mathbf{r}}\mathbf{E}_{\mathbf{k}n}(\mathbf{r}))e^{i\mathbf{p}\mathbf{r}} \tag{26}$$

with $\Psi_{\mathbf{p}}(\mathbf{r})$ being the normalized wave function of the electron state $\Psi_{\mathbf{p}}(\mathbf{r}) = \langle \mathbf{r}|\,\mathbf{p}\rangle$. Here we have taken into account that $\Psi_{\mathbf{p}} = e^{i\mathbf{p}\mathbf{r}}/\sqrt{V}$ for $\mathbf{r}\in V$ and $\Psi_{\mathbf{p}} = 0$ for $\mathbf{r}\notin V$. Taking also into account that $\mathbf{E}_{\mathbf{k}n}(\mathbf{r})$ can be expanded as

$$\mathbf{E}_{\mathbf{k}n}(\mathbf{r}) = \sum_{\mathbf{G}}\mathbf{E}_{\mathbf{k}n}(\mathbf{G})e^{i(\mathbf{k}+\mathbf{G})\cdot\mathbf{r}} \tag{27}$$

with $\mathbf{G}$ being the reciprocal lattice vector of the photonic crystal ($\mathbf{G} = N_1\mathbf{b}_1 + N_2\mathbf{b}_2 + N_3\mathbf{b}_3$ where $\mathbf{b}_i$ is the basis vector of a reciprocal lattice), for $\langle \mathbf{p}'; \mathbf{k}, n|H_I^{pc}|\mathbf{p}\rangle$ we get

$$\langle \mathbf{p}'; \mathbf{k}, n|H_I^{pc}|\mathbf{p}\rangle = -\frac{e}{m_e}\frac{1}{\sqrt{V\omega_{\mathbf{k}n}}}\sum_{\mathbf{G}}\mathbf{p}\cdot\mathbf{E}_{\mathbf{k}n}(\mathbf{G})\delta_{\mathbf{p},\mathbf{q}} \tag{28}$$

with $\mathbf{q} = \mathbf{p}' + \mathbf{k} + \mathbf{G}$. For $\langle \mathbf{p}|H_I^{pc}|\mathbf{p}'; \mathbf{k}, n\rangle$ we find

$$\langle \mathbf{p}|H_I^{pc}|\mathbf{p}'; \mathbf{k}, n\rangle = -\frac{e}{m_e}\frac{1}{\sqrt{V\omega_{\mathbf{k}n}}}\sum_{\mathbf{G}}\mathbf{p}\cdot\mathbf{E}^*_{\mathbf{k}n}(\mathbf{G})\delta_{\mathbf{p},\mathbf{q}}. \tag{29}$$

Using these matrix elements, we can determine the mass correction δm_{pc} as a difference of the electromagnetic masses in PC and free space:

$$\delta m_{pc} = -\frac{2e^2}{\mathbf{p}^2V}\left(\sum_{\mathbf{G}}\sum_{\mathbf{k}n}\frac{1}{\omega_{\mathbf{k}n}}\frac{|\mathbf{p}\cdot\mathbf{E}_{\mathbf{k}n}(\mathbf{G})|^2}{\frac{\mathbf{p}^2}{2m_e} - \frac{(\mathbf{p}-\mathbf{k}-\mathbf{G})^2}{2m_e} - \omega_{\mathbf{k}n}} - \sum_{\mathbf{k}}\sum_{\lambda=1}^{2}\frac{1}{2|\mathbf{k}|}\frac{|\mathbf{p}\cdot\varepsilon_\lambda(\mathbf{k})|^2}{\frac{\mathbf{p}^2}{2m_e} - \frac{(\mathbf{p}-\mathbf{k})^2}{2m_e} - |\mathbf{k}|}\right). \tag{30}$$

It should be noted that this expression has a natural cutoff because dielectric constant vanishes at higher optical energies. Taking into account that electron momentum is much higher that photon momentum, Eq. (30) can be rewritten in the form

$$\delta m_{pc} = \frac{2e^2}{\mathbf{p}^2V}\left(\sum_{\mathbf{G}}\sum_{\mathbf{k}n}\frac{|\mathbf{p}\cdot\mathbf{E}_{\mathbf{k}n}(\mathbf{G})|^2}{\omega^2_{\mathbf{k}n}} - \sum_{\mathbf{k}}\sum_{\lambda=1}^{2}\frac{|\mathbf{p}\cdot\varepsilon_\lambda(\mathbf{k})|^2}{2\mathbf{k}^2}\right). \tag{31}$$

Now in the expression of δm_{pc}, we can replace the discreet sums by integrals:

$$\int d^3k \sum_{\mathbf{k}n} \to \frac{V}{(2\pi)^3} \sum_n \int d^3k, \quad \sum_{\mathbf{k}} \to \frac{V}{(2\pi)^3} \int d^3k. \tag{32}$$

In this way we get

$$\delta m_{pc} = \frac{\alpha}{\pi^2} \left[\sum_n \int\limits_{FBZ} \frac{d^3k}{\omega_{\mathbf{k}n}^2} \sum_{\mathbf{G}} \left| \frac{\mathbf{p}}{|\mathbf{p}|} \cdot \mathbf{E}_{\mathbf{k}n}(\mathbf{G}) \right|^2 - \int \frac{d^3k}{2\mathbf{k}^2} \sum_{\lambda=1}^{2} \left| \frac{\mathbf{p}}{|\mathbf{p}|} \cdot \varepsilon_\lambda(\mathbf{k}) \right|^2 \right]. \tag{33}$$

Accounting for the effect under study for the energy of an electron in the PC medium, we get

$$E_p = m_e + \delta m_e \left(\widehat{\mathbf{p}/|\mathbf{p}|} \right) + \frac{\mathbf{p}^2}{2m_e} \delta m_{pc} \left(\widehat{\mathbf{p}/|\mathbf{p}|} \right) + o\left(\frac{|\mathbf{p}|^4}{m_e^4} \right) m_e. \tag{34}$$

In dealing with an atomic electron, we have also to take into account that its momentum should be described by the momentum operator $\widehat{\mathbf{p}}$ and hence δm_{pc} should be described by the corresponding operator $\delta m_{pc} \left(\widehat{\mathbf{p}/|\mathbf{p}|} \right)$. In this way we arrive at the following expression for the mass correction ΔE_i^{mc} to energies of the states of a hydrogen-like atom:

$$\Delta E_i^{mc} = \left\langle i \left| \delta m_e \left(\widehat{\mathbf{p}/|\mathbf{p}|} \right) \right| i \right\rangle + \left\langle i \left| \frac{|\mathbf{p}|^2}{2m_e} \delta m_e \left(\widehat{\mathbf{p}/|\mathbf{p}|} \right) \right| i \right\rangle + o(\cdots) m_e. \tag{35}$$

In the ground S-state $|S\rangle$, the mean value of the operator $\delta m_{pc} \left(\widehat{\mathbf{p}/|\mathbf{p}|} \right)$ is

$$\left\langle \delta m_{pc} \right\rangle_S = \frac{4\alpha}{3\pi} \int d\omega \frac{N(\omega) - \omega^2}{\omega^2}, \tag{36}$$

where $N(\omega) = N_{DOS}(\omega) D(\omega)$ and $N_{DOS}(\omega)$ is the photon density of states

$$N_{DOS}(\omega) = \frac{1}{4\pi} \sum_n \int\limits_{FBZ} d^3k \delta(\omega - \omega_{\mathbf{k}n}) \tag{37}$$

and

$$D(\omega) = \sum_{\mathbf{G}} |\mathbf{E}_{\mathbf{k}n}(\mathbf{G})|^2_{|\omega_{\mathbf{k}n} = \omega.}} \tag{38}$$

The function $N(\omega)$ is closely associated with DOS of the PC. The exact calculation of this function is challenging for 3D PC; therefore we will use a model having the form

$$N(\omega) = \omega^2 n_{eff}^3 \left[1 - h \exp\left(-\frac{(\omega - \omega_0)^2}{\sigma^2} \right) \right] F(\omega), \tag{39}$$

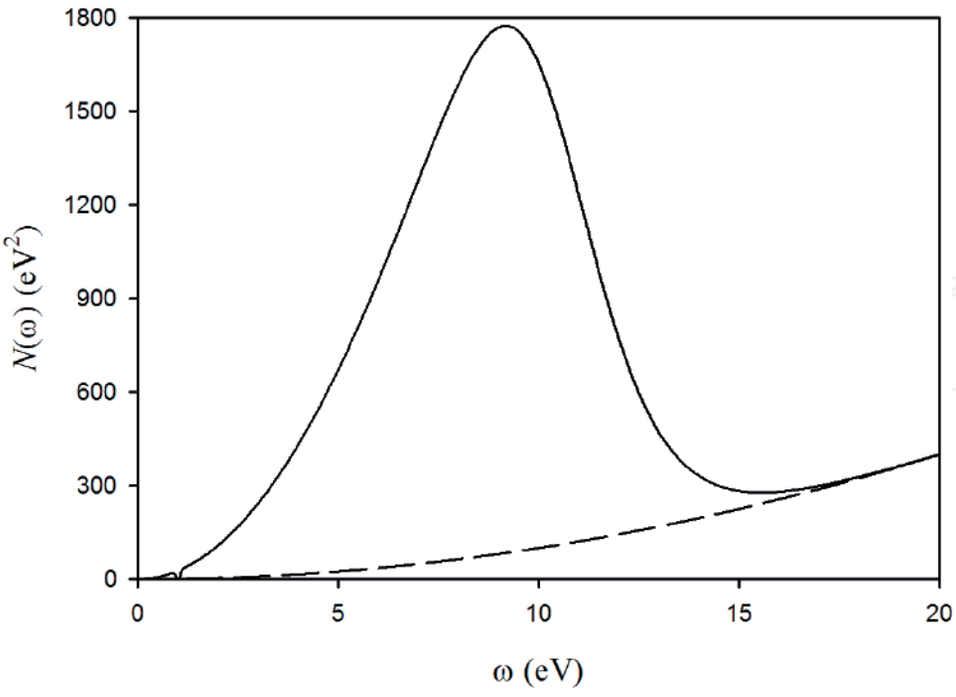

Figure 2. The model $N(\omega)$ determined by the Eq. (39) with $n_{eff}=3$, $h=0.96$, $\sigma=0.07$ eV, $\mu=15$ eV, $\tau=0.01$ eV, and $\omega_0=1$ eV. Dashed line denotes the free space DOS.

where the factor $F(\omega)=n_{eff}^{-3}+\left(1-n_{eff}^{-3}\right)/\left(\exp\left\{(\omega-\mu)/\tau\right\}+1\right)$ with $n_{eff}\equiv\sqrt{\overline{\varepsilon}}$. $\overline{\varepsilon}=\varepsilon\cdot f+(1-f)$ is an average dielectric constant with ε being the dielectric constant of the host material and f being the dielectric fraction in the PC. This model can recapture the existence of photonic band gap, optical density of dielectric host of PC sample, and the fact that at high enough photon energies, $N(\omega)$ must approach the free space DOS (**Figure 2**). For the parameters which were used in **Figure 2**, our calculations have given $\langle\delta m_{pc}\rangle_S=2.4\cdot10^{-6}m_e$.

Let us now consider the effect of the change in the electron mass on the energies of the atomic states and the transition frequencies. Here we will restrict ourselves to the hydrogen-like atoms. In the free space, the energy of the atoms in the state $|a\rangle=|n,j,l,m\rangle$ is the sum of the energy derived from the solution of the Dirac equation $E^D=m_eR_{nj}$ and the Lamb shift of the energy in this state:

$$E_{njl}=m_eR_{nj}+\Delta E_{L,a}, \tag{40}$$

where

$$R_{nj}=\left[1+\left(\frac{Z\alpha}{n-(j+1/2)+\sqrt{(j+1/2)^2-\alpha^2}}\right)^2\right]^{-1/2} \tag{41}$$

and $\Delta E_{L,a}$ is the Lamb shift of the energy of the state $|a\rangle$. The transition frequency between this state and the state $|b\rangle=|n',j',l',m\rangle$ is given by

$$\omega_{ab} = m_e\left(R_{nj} - R_{n'j'}\right) + (\Delta E_{L,a} - \Delta E_{L,b}). \tag{42}$$

When the atom is placed in the void of a PC, the transition frequencies ω_{ab}^{PC} are modified as follows:

$$\omega_{ab}^{PC} = \left(m_e + \left\langle a\middle|\delta m_e^{PC}\left(\widehat{\mathbf{p}/|\mathbf{p}|}\right)\middle|a\right\rangle\right)R_{nj} + \Delta E_{L,a}^{PC} - \left(m_e + \left\langle b\middle|\delta m_e^{PC}\left(\widehat{\mathbf{p}/|\mathbf{p}|}\right)\middle|b\right\rangle\right)R_{n'j'} - \Delta E_{L,b}^{PC}. \tag{43}$$

In the case when the atom is light, Eq. (43) is reduced to the following expression:

$$\begin{aligned}\omega_{ab}^{PC} &= \left\langle a\middle|\delta m_e^{PC}\left(\widehat{\mathbf{p}/|\mathbf{p}|}\right)\middle|a\right\rangle\left(1 - \frac{Z^2\alpha^2}{2n^2}\right) - \left\langle b\middle|\delta m_e^{PC}\left(\widehat{\mathbf{p}/|\mathbf{p}|}\right)\middle|b\right\rangle^2\left(1 - \frac{Z^2\alpha^2}{2n^2}\right)\\ &+ \frac{m_e Z\alpha^2}{2}\left(\frac{1}{n^2} - \frac{1}{(n')^2}\right) + \Delta E_{L,a}^{PC} - \Delta E_{L,b}^{PC} = \frac{m_e Z\alpha^2}{2}\left(\frac{1}{n^2} - \frac{1}{(n')^2}\right) + \Delta\omega_{ab}^{PC} + o\left(Z^2\alpha^4\right)m_e,\end{aligned} \tag{44}$$

where $\Delta\omega_{ab}^{PC}$ is the correction to the transition frequency in the PC medium given by

$$\Delta\omega_{ab}^{PC} = \left\langle a\middle|\delta m_e^{PC}\left(\widehat{\mathbf{p}/|\mathbf{p}|}\right)\middle|a\right\rangle - \left\langle b\middle|\delta m_e^{PC}\left(\widehat{\mathbf{p}/|\mathbf{p}|}\right)\middle|b\right\rangle. \tag{45}$$

As we have shown, the values of the mass corrections $\left\langle i\middle|\delta m_{PC}\left(\widehat{\mathbf{p}/|\mathbf{p}|}\right)\middle|i\right\rangle$ may be of order $10^{-6}m_e$, and hence the corrections to the transition frequencies are comparable to the atomic optical frequencies.

5. Experimental observation

Since spectra remain discrete when the PC medium affects interaction between atoms and their own emission fields, it would be logical to conduct an experiment in which we could observe this effect. This could be accomplished by observing the classical spectra of the atoms in the gas phase, pumped into PC cavities. From a theoretical point of view, it would be best to conduct the experiment with hydrogen atoms, since they are the simplest physical system. However, the handling of atomic hydrogen creates a number of technical difficulties; from a practical point of view, the best candidates for the role of such atoms are those of the noble gases, for example, helium. With respect to the requirements for a PC sample, it is first of all obvious that it should have cavities that are sufficiently interconnected to ensure the possibility of pumping gas. Second, the material of the PC sample should have the largest possible refractive index in the widest possible range of energies, since the effect depends strongly on the optical contrast [36]. Finally, the larger the amount of material filling the PC volume, the greater the effect. At the same time, the cavities must remain large enough to meet the condition that the atoms are free to move. It should be noted that an increase in the relative shift of the lines $\delta\omega/\omega$, along with an increase in the main quantum number n, is unequivocal confirmation of the effect, since the predicted shift of the lines does not depend on it.

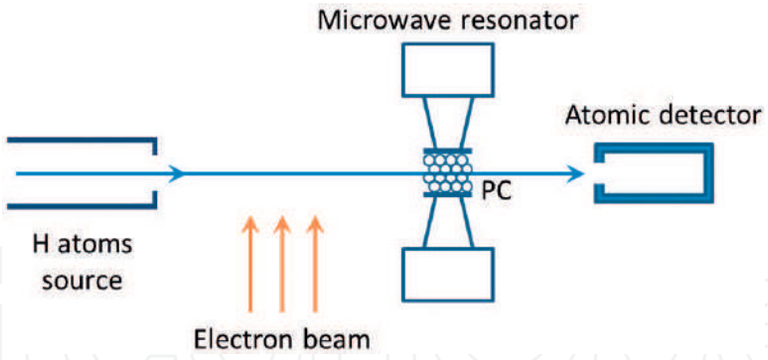

Figure 3. Scheme of modified Lamb shift experiment.

As a simple and natural way to confirm the considered effect, we propose to use a modified experiment to measure Lamb shift in hydrogen atom placed in the voids of photonic crystal (**Figure 3**). In the experiment the hydrogen atoms are exposed to electromagnetic radiation of a certain frequency, and if this frequency corresponds to the difference between the $2S_{1/2}$ and $2P_{1/2}$ energy levels (~1058 MHz without PC medium), no excited atoms will reach the detector. However taking into account the influence of the photonic crystal on the energy levels of atoms the Lamb shift will differ from 1058 MHz, the excited atoms will appear on the detector which will confirm the effect. Then we can measure new Lamb shift by adjusting the frequency of electromagnetic radiation.

There are a number of technical issues which need to be resolved. First, all exposed atoms must be within the photonic crystal, that is, electromagnetic radiation should be concentrated in a relatively small volume of a photonic crystal using antennas or waveguides. Second, as already noted, there are many requirements to the sample of photonic crystal, including the quality of the structure and possibility of free passage of hydrogen atoms through the PC medium. To solve the last one, we propose to use photonic crystals with inverted opal structure [37], the volume fraction of air voids which is approximately 74%. Such structures are fabricated from synthetic opals by filling voids between spherical particles with any desired material. After that initial particles are removed leaving a framework with spherical air voids. However, the resulting structures have a large number of defects and have significant limitations in linear dimensions.

6. Prospects of applications of the effect

The most surprising feature of the effect under study is that the electromagnetic mass of the electron comes into play when an atom is placed in the voids of a PC. There are no analogs of such QED effect in the free space. The correction to the electromagnetic mass caused by the modification of the electromagnetic interaction strongly changes the character of processes of the spontaneous emission and the absorption of atoms placed in the PC medium, and this can open up new possibilities for applying PCs. For the first time, one can change the transitions on the value comparable to the ordinary atomic transition frequencies. This effect becomes possible due to the dependence of the electromagnetic mass correction on the orientation of the

electron momentum in the PC medium. This provides a way to control the structure of the atomic energy levels. In this way, in particular, light sources with the line spectrum of a new type could be developed.

The line spectrum sources such as He-Ne laser play an important role in physics and technologies. However, the corresponding transition frequencies in the optical range are limited. The mass-change effect under study opens possibilities to tune the energy levels of He and Ne and, as a consequence, to increase the slope efficiency. It allows one to create the new He-Ne-like lasers.

One of the most perspective applications of the effect is a realization of quantum interference. Quantum interference among different decay channels caused by the anisotropic vacuum is the major field of research. Several ways have been proposed to create the anisotropy and to provide interference between atomic levels in such materials as negative-index materials [38–43], metasurfaces [44], hyperbolic metamaterials [45], metallic nanostructures [46, 47], topological insulators [48], and external fields [49–51]. The possibility for making use of anisotropy in the PC medium for these purposes has been investigated in Refs. [52–55]. The authors of the listed papers based themselves on the idea voiced by Agarwal [56] who pointed that the anisotropy of the vacuum can cause the quantum interference between nearest energy levels (e.g., Zeeman sublevels) having orthogonal dipole moments. The effect of the change in the electron mass in a PC provides new possibilities to create conditions at which quantum interference becomes possible via nonradiative transitions between atomic levels with breaking the strict selection rules.

7. Conclusion

The QED effects on which we focused play an important role in the physics of PCs. The Lamb shift in atoms that is one of the most important phenomena of the QED becomes larger in the case when the atom is placed in the air voids of PCs. But what is especially important is that in the case where an atom is placed in the artificial PC medium, we face a phenomenon that does not manifest itself in vacuum. This phenomenon consists in the fact that the part of the electromagnetic mass m_{em} of the electron that together with the bare mass m_0 constitutes the physical mass $m_{ph}=m_0+m_{em}$ becomes observable. In vacuum only m_{ph} is observable. This fact is used in the renormalization theory that is of the central importance in QED. The renormalization procedure implies that the terms describing the self-energy of the free electron should be removed from any expressions describing the processes in which the electron takes place. This is an explanation of the fact that for long time, this subtraction procedure was used in describing the Lamb shift in atoms placed in PCs despite that the electromagnetic interaction in the PC medium is significantly modified. The correction $\delta m_{pc}=m_{em}^{pc}-m_{em}$ to the electromagnetic mass of the electron caused by this modification cannot be hidden in the physical mass of the electron and for this reason is observable. Thus, in the case of the artificial PC medium, the electromagnetic mass (more precisely its part δm_{pc}) comes into play. In contrast to the Lamb shift that is relatively small correction to the atomic energy levels, the

electromagnetic mass correction δm_{pc} can have a significant effect not only on the energy levels of atoms placed in the PC medium but also on the physical processes in these atoms. The key point is that δm_{pc} depends on the orientation of the electron momentum in a PC and actually is an operator $\delta m_{pc}\left(\widehat{\mathbf{p}/|\mathbf{p}|}\right)$ whose diagonal matrix elements determine the corrections to the transition frequencies that are comparable to the atomic frequencies in the free space. The nondiagonal matrix elements determine nonradiative transitions between the states with breaking the strict selection rules. These transitions give rise to the quantum interference between the different decay channels. The possibility of controlling these quantum-interference processes can be important for quantum information science.

Author details

Renat Gainutdinov[1]*, Marat Khamadeev[1,2], Albert Akhmadeev[1,2] and Myakzyum Salakhov[1,2]

*Address all correspondence to: renat.gainutdinov@kpfu.ru

1 Institute of Physics, Kazan Federal University, Kazan, Russian Federation

2 Tatarstan Academy of Sciences, Kazan, Russian Federation

References

[1] Yablonovitch E. Inhibited spontaneous emission in solid-state physics and electronics. Physical Review Letters. 1987;**58**(20):2059-2062. DOI: 10.1103/PhysRevLett.58.2059

[2] John S. Strong localization of photons in certain disordered dielectric superlattices. Physical Review Letters. 1987;**58**(23):2486-2489. DOI: 10.1103/PhysRevLett.58.2486

[3] Quang T, Woldeyohannes M, John S, Agarwal GS. Coherent control of spontaneous emission near a photonic band edge: A single-atom optical memory device. Physical Review Letters. 1997;**79**(26):5238-5241. DOI: 10.1103/PhysRevLett.79.5238

[4] John S, Wang J. Quantum electrodynamics near a photonic band gap: Photon bound states and dressed atoms. Physical Review Letters. 1990;**64**(20):2418-2421. DOI: 10.1103/PhysRevLett.64.2418

[5] John S, Wang J. Quantum optics of localized light in a photonic band gap. Physical Review B. 1991;**43**(16):12772-12789. DOI: 10.1103/PhysRevB.43.12772

[6] Bay S, Lambropoulos P, Mølmer K. Fluorescence into flat and structured radiation continua: An atomic density matrix without a master equation. Physical Review Letters. 1997;**79**(14):2654-2657. DOI: 10.1103/PhysRevLett.79.2654

[7] Bay S, Lambropoulos P, Mølmer K. Atom-atom interaction in strongly modified reservoirs. Physical Review A. 1997;**55**(2):1485-1496. DOI: 10.1103/PhysRevA.55.1485

[8] Busch K, Vats N, John S, Sanders BC. Radiating dipoles in photonic crystals. Physical Review E. 2000;**62**:4251-4260. DOI: 10.1103/PhysRevE.62.4251

[9] Zhu S-Y, Chen H, Huang H. Quantum interference effects in spontaneous emission from an atom embedded in a photonic band gap structure. Physical Review Letters. 1997;**79** (2):205-208. DOI: 10.1103/PhysRevLett.79.205

[10] John S, Quang T. Localization of superradiance near a photonic band gap. Physical Review Letters. 1995;**74**(17):3419-3422. DOI: 10.1103/PhysRevLett.74.3419

[11] Lopez C. Materials aspects of photonic crystals. Advanced Materials. 2003;**15**:1679-1704. DOI: 10.1002/adma.200300386

[12] Mateos L, Molina P, Galisteo J, López C, Bausá LE, Ramírez MO. Simultaneous generation of second to fifth harmonic conical beams in a two dimensional nonlinear photonic crystal. Optics Express. 2012;**20**:29940-29948. DOI: 10.1364/OE.20.029940

[13] Pinto AMR, Lopez-Amo M. Photonic crystal fibers for sensing applications. Journal of Sensors. 2012;**2012**:598178. DOI: 10.1155/2012/598178

[14] Tuyen LD, Liu AC, Huang C-C, Tsai PC, Lin JH, C-W W, Chau L-K, Yang TS, Minh LQ, Kan H-C, Hsu CC. Doubly resonant surface-enhanced Raman scattering on gold nanorod decorated inverse opal photonic crystals. Optics Express. 2012;**20**:29266-29275. DOI: 10.1364/OE.20.029266

[15] Callahan DM, Munday JN, Atwater HA. Solar cell light trapping beyond the ray optic limit. Nano Letters. 2012;**12**:214-218. DOI: 10.1021/nl203351k

[16] Gainutdinov RK, Khamadeev MA, Salakhov MK. Electron rest mass and energy levels of atoms in the photonic crystal medium. Physical Review A. 2012;**85**(5):053836(1-7). DOI: 10.1103/PhysRevA.85.053836

[17] Pohl R, Gilman R, Miller GA, Pachucki K. Muonic hydrogen and the proton radius puzzle. Annual Review of Nuclear and Particle Science. 2013;**63**:175-204. DOI: 10.1146/annurev-nucl-102212-170627

[18] Carlson CE. The proton radius puzzle. Progress in Particle and Nuclear Physics. 2045;**82**:59-77. DOI: 10.1016/j.ppnp.2015.01.002

[19] Sick I. On the rms-radius of the proton. Physics Letters B. 2003;**576**:62-67. DOI: 10.1016/j.physletb.2003.09.092

[20] Bernauer JC et al. (A1 collaboration). High-precision determination of the electric and magnetic form factors of the proton. Physical Review Letters. 2010;**105**:242001. DOI: 10.1103/PhysRevLett.105.242001

[21] Niering M, Holzwarth R, Reichert J, Pokasov P, Udem T, Weitz M, Hänsch TW, Lemonde P, Santarelli G, Abgrall M, Laurent P, Salomon C, Clairon A. Measurement of the hydrogen 1S-2S transition frequency by phase coherent comparison with a microwave Cesium fountain clock. Physical Review Letters. 2000;**84**:5496. DOI: 10.1103/PhysRevLett.84.5496

[22] Fischer M, Kolachevsky N, Zimmermann M, Holzwarth R, Udem T, Hänsch TW, Abgrall M, Grünert J, Maksimovic I, Bize S, Marion H, Pereira dos Santos F, Lemonde P, Santarelli G, Laurent P, Clairon A, Salomon C, Haas M, Jentschura UD, Keitel CH. New limits on the drift of fundamental constants from laboratory measurements. Physical Review Letters. 2004;**92**:230802. DOI: 10.1103/PhysRevLett.92.230802

[23] Parthey CG, Matveev A, Alnis J, Bernhard B, Beyer A, Holzwarth R, Maistrou A, Pohl R, Predehl K, Udem T, Wilken T, Kolachevsky N, Abgrall M, Rovera D, Salomon C, Laurent P, Hänsch TW. Improved measurement of the hydrogen 1S-2S transition frequency. Physical Review Letters. 2011;**107**:203001. DOI: 10.1103/PhysRevLett.107.203001

[24] Schwob C, Jozefowski L, de Beauvoir B, Hilico L, Nez F, Julien L, Biraben F, Acef O, Zondy JJ, Clairon A. Optical frequency measurement of the 2S-12D transitions in hydrogen and deuterium: Rydberg constant and lamb shift determinations. Physical Review Letters. 1999;**82**:4960. DOI: 10.1103/PhysRevLett.82.4960

[25] de Beauvoir B, Nez F, Julien L, Cagnac B, Biraben F, Touahri D, Hilico L, Acef O, Clairon A, Zondy JJ. Absolute frequency measurement of the 2S-8S/D transitions in hydrogen and deuterium: New determination of the Rydberg constant. Physical Review Letters. 1997;**78**:440. DOI: 10.1103/PhysRevLett.78.440

[26] de Beauvoir B, Schwob C, Acef O, Jozefowski L, Hilico L, Nez F, Julien L, Clairon A, Biraben F. Metrology of the hydrogen and deuterium atoms: Determination of the Rydberg constant and lamb shifts. European Physical Journal D: Atomic, Molecular, Optical and Plasma Physics. 2000;**12**:61-93. DOI: 10.1007/s100530070043

[27] Arnoult O, Nez F, Julien L, Biraben F. Optical frequency measurement of the 1S-3S two-photon transition in hydrogen. European Physical Journal D: Atomic, Molecular, Optical and Plasma Physics. 2010;**60**:243-256. DOI: 10.1140/epjd/e2010-00249-6

[28] Bjorken JD, Drell SD. Relativistic Quantum Mechanics. Vol. 1. New York: McGraw-Hill; 1964. 311 p

[29] Schweber SS. An Introduction to Relativistic Quantum Field Theory. New York: Dover; 2005. 928 p

[30] Zhu S-Y, Yang Y, Chen H, Zheng H, Zubairy MS. Spontaneous radiation and lamb shift in three-dimensional photonic crystals. Physical Review Letters. 2000;**84**(10):2136-2139. DOI: 10.1103/PhysRevLett.84.2136

[31] Li Z-Y, Xia Y. Optical photonic band gaps and the lamb shift. Physical Review. B, Condensed Matter and Materials physics. 2001;**63**(12):121305(1-4). DOI: 10.1103/PhysRevB.63.121305

[32] Vats N, John S, Busch K. Theory of fluorescence in photonic crystals. Physical Review A. 2002;**65**(4):43808(1-13). DOI: 10.1103/PhysRevA.65.043808

[33] Wang X-H, Kivshar YS, Gu B-Y. Giant lamb shift in photonic crystals. Physical Review Letters. 2004;**93**(7):073901(1-4). DOI: 10.1103/PhysRevLett93.073901

[34] Wang X-H, B-Y G, Kivshar YS. Spontaneous emission and lame shift in photonic crystals. Science and Technology of Advanced Materials. 2005;**6**(7):814-822. DOI: 10.1016/j.stam.2005.06.025

[35] Sakoda K. Optical Properties of Photonic Crystals. Berlin: Springer; 2001. 227 p. DOI: 10.1007/978-3-662-14324-7

[36] Gainutdinov RK, Salakhov MK, Khamadeev MA. Optical contrast of a photonic crystal and the self energy shift of the energy levels of atoms. Bulletin of the Russian Academy of Sciences: Physics. 2012;**76**(12):1301-1305. DOI: 10.3103/S106287381212012X

[37] Khokhlov PE, Sinitskii AS, Tretyakov YD. Inverse photonic crystals based on silica. Doklady Chemistry. 2006;**408**(1):61-64. DOI: 10.1134/S0012500806050028

[38] Li G-X, Evers J, Keitel CH. Spontaneous emission interference in negative-refractive-index waveguides. Physical Review. B, Condensed Matter and Materials Physics. 2009;**80**(4):045102 (1-7). DOI: 10.1103/PhysRevB.80.045102

[39] Zeng X, Xu J, Yang Y. Spontaneous emission interference enhancement with a μ-negative metamaterial slab. Physical Review A. 2011;**84**(3):033834(1-5). DOI: 10.1103/PhysRevA.84.033834

[40] Yang Y, Xu J, Chen H, Zhu S. Quantum interference enhancement with left-handed materials. Physical Review Letters. 2008;**100**(4):043601(1-4). DOI: 10.1103/PhysRevLett.100.043601

[41] Xu J, Chang S, Yang Y, Al-Amri M. Casimir-polder force on a v-type three-level atom near a structure containing left-handed materials. Physical Review A. 2016;**93**(1):012514 (1-8). DOI: 10.1103/PhysRevA.93.012514

[42] Zeng X, Yu M, Wang D, Xu J, Yang Y. Spontaneous emission spectrum of a V-type three-level atom in a fabry-perot cavity containing left-handed materials. Journal of the Optical Society of America B: Optical Physics. 2011;**28**(9):2253-2259. DOI: 10.1364/JOSAB.28.002253

[43] Xu J-P, Yang Y-P. Quantum interference of V-type three-level atom in structures made of left-handed materials and mirrors. Physical Review A. 2010;**81**(1):013816(1-8). DOI: 10.1103/PhysRevA.81.013816

[44] Jha PK, Ni X, Wu C, Wang Y, Zhang X. Metasurface-enabled remote quantum interference. Physical Review Letters. 2015;**115**(2):025501(1-5). DOI: 10.1103/PhysRevLett.115.025501

[45] Sun L, Jiang C. Quantum interference in a single anisotropic quantum dot near hyperbolic metamaterials. Optics Express. 2016;**24**(7):7719-7727. DOI: 10.1364/OE.24.007719

[46] Yannopapas V, Paspalakis E, Vitanov NV. Plasmon-induced enhancement of quantum interference near metallic nanostructures. Physical Review Letters. 2009;**103**(6):063602(1-4). DOI: 10.1103/PhysRevLett.103.063602

[47] Evangelou S, Yannopapas V, Paspalakis E. Simulating quantum interference in spontaneous decay near plasmonic nanostructures: Population dynamics. Physical Review A. 2011;**83**(5):055805(1-4). DOI: 10.1103/PhysRevA.83.055805

[48] Fang W, Yang Z-X, Li G-X. Quantum properties of an atom in a cavity constructed by topological insulators. Journal of Physics B: Atomic, Molecular and Optical Physics. 2015;**48**(24):245504(1-10). DOI: 10.1088/0953-4075/48/24/245504

[49] Mortezapour A, Saleh A, Mahmoudi M. Birefringence enhancement via quantum interference in the presence of a static magnetic field. Laser Physics. 2013;**23**(6):065201(1-7). DOI: 10.1088/1054-660X/23/6/065201

[50] Ficek Z, Swain S. Simulating quantum interference in a three-level system with perpendicular transition dipole moments. Physical Review A. 2004;**69**(2):023401(1-10). DOI: 10.1103/PhysRevA.69.023401

[51] Tan H-T, Xia H-X, Li G-X. Quantum interference and phase-dependent fluorescence spectrum of a four-level atom with antiparallel dipole moments. Journal of Physics B: Atomic, Molecular and Optical Physics. 2009;**42**(12):125502(1-6). DOI: 10.1088/0953-4075/42/12/125502

[52] J-P X, Wang L-G, Yang Y-P, Lin Q, Zhu S-Y. Quantum interference between two orthogonal transitions of an atom in one-dimensional photonic crystals. Optics Letters. 2008;**33**(17):2005-2007. DOI: 10.1364/OL.33.002005

[53] Li G-X, Li F-L, Zhu S-Y. Quantum interference between decay channels of a three-level atom in a multilayer dielectric medium. Physical Review A. 2001;**64**(1):013819(1-10). DOI: 10.1103/PhysRevA.64.013819

[54] Zhang HZ, Tang SH, Dong P, He J. Spontaneous emission spectrum from a V-type three-level atom in a double-band photonic crystal. Journal of Optics B: Quantum and Semiclassical Optics. 2002;**4**(5):300-307. DOI: 10.1088/1464-4266/4/5/312

[55] Zhang HZ, Tang SH, Dong P, He J. Quantum interference in spontaneous emission of an atom embedded in a double-band photonic crystal. Physical Review A. 2002;**65**(6A):063802(1-8). DOI: 10.1103/PhysRevA.65.063802

[56] Agarwal GS. Anisotropic vacuum-induced interference in decay channels. Physical Review Letters. 2000;**84**(24):5500-5503. DOI: 10.1103/PhysRevLett.84.5500

Chapter 2

Anomalous Transmission Properties Modulated by Photonic Crystal Bands

Guoyan Dong

Additional information is available at the end of the chapter

http://dx.doi.org/10.5772/intechopen.71403

Abstract

Photonic crystals (PhCs) can be utilized to control the propagation behaviors of light within a frequency band (i.e., conduction band or stop band) for their periodic arrangements of dielectric. Utilizing the effect of band gap one may introduce defects in a photonic crystal to limit or guide the electromagnetic wave with the frequency in stop gaps. Furthermore, based on synthetic periodic dielectric materials photonic crystals can exhibit various anomalous transmission properties, such as negative refraction, self-focusing, zero phase delay or effective-zero-index properties that are determined by the characteristics of their band structures and equal frequency contours (EFC). These extraordinary results contributing to the design of novel PhC devices and the development of PhC application are demonstrated in this chapter.

Keywords: photonic crystal, photonic band gap, negative refraction, zero phase delay, Dirac-like point

1. Introduction

Photonic crystals (PhCs) are structures in which the dielectric constant is periodically modulated on a length scale comparable to the desired wavelength of operation [1, 2], and the resultant photonic dispersion may exhibit photonic band gaps (PBGs) and anomalous propagation behaviors which are useful in controlling light behavior according to different theoretical principles. Based on the PBG effect we may introduce a line defect in a photonic crystal to guide the electromagnetic waves with the frequency in stop gap [3]. The line defect is called a photonic crystal waveguide (PCW), which is very compact (with the typical width is around half-wavelength) and allows sharp bends without losses for its all-dielectric structure [4]. Many attempts have been made to fabricate materials with complete photonic

band gaps (PBGs) at near-infrared [5] and visible frequencies [6], such as semiconductor microfabrication [7], self-assembly of colloidal particles [8], electron-beam lithography [9], multiphoton polymerization [10], holographic lithography (HL) [11], and so on. Among them, HL is a very promising technique for the inexpensive fabrication of high-quality two- and three-dimensional (2D and 3D) PhC templates with the unique advantages of one-step recording, the ability to obtain an inverse lattice by using a template, inexpensive volume recording and rapid prototyping. The PhCs formed by HL which usually have irregular "atoms" or columns. Since the PBG property of resultant structure varies with the shape of "atoms" or columns, thus the PBGs and propagation properties for PhCs made by HL will be different from those of regular structures.

Veselago predicted a kind of materials with negative refractive index in 1968 [12] which has attracted lots of attention in recent years. Such materials are generally referred to as left-handed materials (LHMs), double negative materials [13], or backward-wave media et al. [14], whose best known characteristic is to refract light in opposite direction. Shelby et al. have accomplished one of the first experiments to demonstrate the negative-index behavior [15]. However, the absorption loss of the metal limits its potential optical applications. Different from LHMs, PhCs made of periodic all-dielectric materials can exhibit an fascinating dispersion such as negative refraction and self-focusing properties which are determined by the properties of their band structures and equal frequency contours (EFC) [16, 17].

In this chapter, the maximal complete relative photonic band gaps of 22.1% and 25.1% are introduced how to be achieved in 2D- and 3D photonic crystals formed by HL method. The symmetry mismatch between the incident wave and the Bloch modes of PhC can be used to guide light efficiently. The unique features of negative refraction, dual-negative refraction, triple refraction phenomena, and special collimation effects of symmetrical positive-negative refraction have been verified by numerical simulations or experiments. Effective measurement method has been proposed to identify the Dirac-like point of finite PhC arrays accurately. A mechanism for generation of efficient zero phase delay of electromagnetic wave propagation based on wavefront modulation is investigated with parallel wavefronts (or phasefronts) extending along the direction of energy flow. The band structures of PBG are calculated by the plane-wave expansion method [18], and a finite-difference time-domain (FDTD) method [19] is used to calculate the transmission property of the guided mode. The method of wave-vector diagram is generally used to predict the properties of beam propagation in PhCs.

2. Characteristics of photonic band gap in 2D- and 3D-PhCs

2.1. Photonic band gap in 2D-PhCs

Since the shape and size of lattice columns in 2D case or atoms in 3D case are usually determined by the isointensity surfaces of the interference field, the columns or atoms formed by this way often are of irregular shapes [20, 21]. Consequently, the PBG property of resultant structure is closely related to the fabrication process. Therefore the complete PBG can be obtained and improved by proper designs of the shape and size of lattice cells [22]. Compared with the 3D

case, the 2D PhCs are easier to fabricate and study theoretically for the fact that, the wave propagation of 2D PhCs can be investigated separately for two orthogonal polarizations known as TM and TE. They have important practical significance because they offer the possibility of guiding and manipulating light in planar defect circuits [23], photonic crystal fibers [24] and controlling polarization through their anisotropic band structures.

A kind of 2D 3-fold PhCs conforming to the hybrid triangular configuration formed by HL was proposed [20]. This kind of hybrid triangular lattice is formed by two sets of triangular lattices, as depicted in **Figure 1**, with the big dots indicating the triangular lattice sites with lattice constant a, while the small dots with the same lattice structure shifting $\sqrt{3}a/3$ in y direction. Different from the 6-fold rotational symmetry of regular triangular lattice structure, this hybrid structure has 3-fold rotational symmetry.

The basis vectors of the hybrid triangular lattice may be chosen as $\boldsymbol{a}_1 = a(1/2, \sqrt{3}/2)$ and $\boldsymbol{a}_2 = a(-1, 0)$. To produce this 2D hybrid triangular lattice holographically, we may use the following intensity of interference field,

$$I = 3 + \cos\left[\frac{2\pi}{a}\left(x - \frac{y}{\sqrt{3}}\right)\right] + \cos\left[\frac{2\pi}{a}\left(x + \frac{y}{\sqrt{3}}\right)\right] + \cos\left(\frac{4\pi}{\sqrt{3}a}y\right)$$
$$+c\left\{\cos\left[\frac{2\pi}{a}\left(x - \left(\frac{y}{\sqrt{3}} - \frac{1}{3}\right)\right)\right] + \cos\left[\frac{2\pi}{a}\left(x + \left(\frac{y}{\sqrt{3}} - \frac{1}{3}\right)\right)\right] + \cos\left(\frac{4\pi}{\sqrt{3}a}\left(y - \frac{\sqrt{3}}{3}\right)\right)\right\}, \tag{1}$$

where the first constant has no essential effect, which can be changed by adjusting the light intensity threshold I_t. The former and latter three cosine terms in this formula define the above mentioned two sets of triangular lattices, respectively. The constant c is a modulation coefficient which has a considerable effect on the final structure and thus the corresponding PBGs.

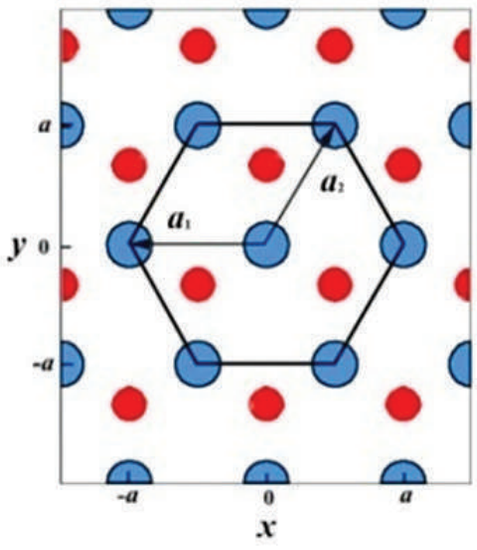

Figure 1. Hybrid triangular lattice with the big dots define a triangular lattice while the small dots compose a same one with a shift of $\sqrt{3}a/3$ in y direction.

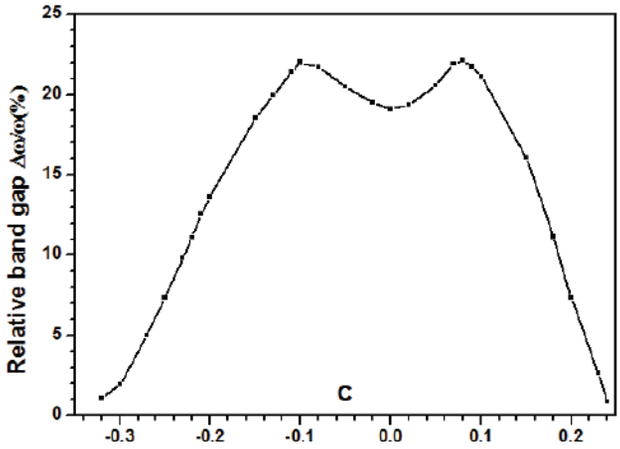

Figure 2. Relation between the value of c and the corresponding maximum relative band width when $\varepsilon = 13.6$. The two peaks of relative band gap occur at $c = -0.1$ and 0.08.

It is clear that the factors of c and I_t can be modulated to control the PBGs. For a given c, a certain lattice structure can be formed by washing away the region of $I < I_t$. If we fill this structure with a material of high refractive index, such as GaAs, and then remove the template, an inverse structure can be achieved as has been successfully demonstrated in Ref. [25]. **Figure 2** represents the relative gap size of optimized structures as a function of c for the dielectric constant contrast of 13.6 to 1 corresponding to GaAs in air. Obviously, the band gaps of PhCs made by HL may be widened from 18.9 to 22.1% by introducing irregularity of the columns and lowering the symmetry of the structure.

In addition, another kind of 2D 6-fold hybrid triangular configuration formed holographically is proposed [21], in which the complete PBGs can be found even with much lower dielectric constant ($\varepsilon = 3.8$). This 2D periodic structure is a hybrid triangular lattice combining two sets of triangular sublattices as depicted in **Figure 3**, where the red dots denote a triangular sublattice with lattice constant a, while the blue dots denote another set with the lattice constant of $a/\sqrt{3}$ which is rotated by an angle of 30° with respect to the former.

For the triangular structure formed holographically the complete PBGs always appear in inverse structures (air columns in dielectric material) with high dielectric constant instead of normal structures [26]. However, the complete PBG may be obtained for normal structure (dielectric column in air background) with lower dielectric contrast ($\varepsilon = 3.8$). **Figure 4** indicates the relations of relative band gap $\Delta\omega/\omega$ with maximum peak value to filling ratio f for different dielectric contrasts. Computations show that the peak value of optimum relative PBG not always augments with the increase of dielectric constant ε for normal structure, instead, the peak value reaches the maximum at about $\varepsilon = 8.9$, such as 9.9% with $f = 15.9\%$ for $\varepsilon = 8.9$ and $c = 1.2$, which is larger than the result (8.8%) of best designed pincushion columns with the same dielectric constant [27]. Specially, in this kind of normal structures, the required minimum permittivity to open a complete photonic band gap with $\Delta\omega/\omega > 1\%$ is near 3.8, which is much lower than the value of 6.4 in the case of pincushion columns [27] and lower than all the results of 2D photonic crystals ever reported before. In addition, the complete PBGs of this

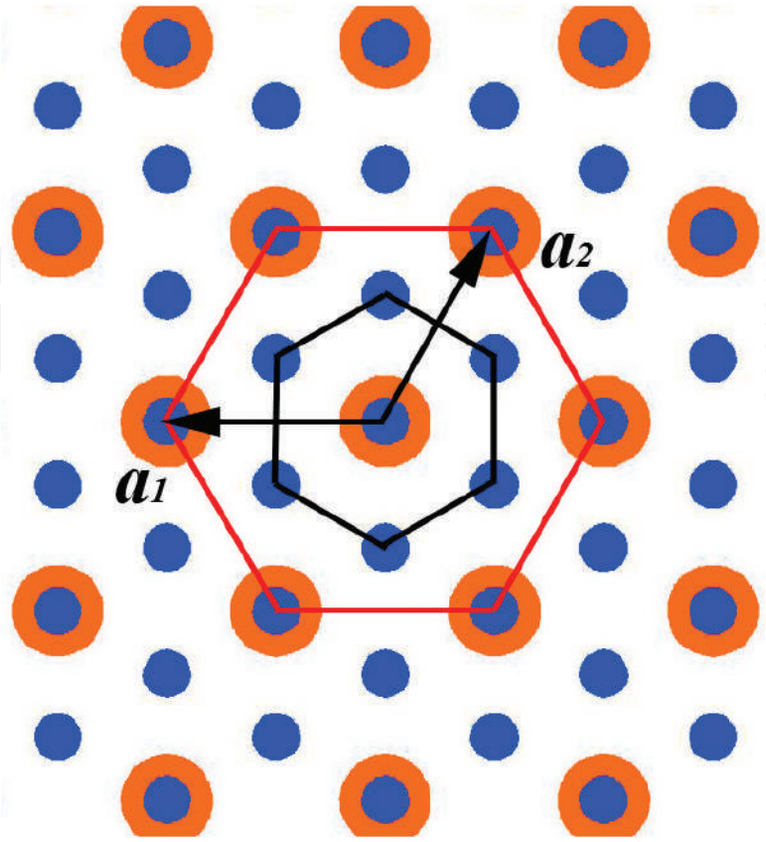

Figure 3. The hybrid triangular lattice, where red dots define triangular sublattice, blue dots define another group with lattice constant $a/\sqrt{3}$ rotated 30°.

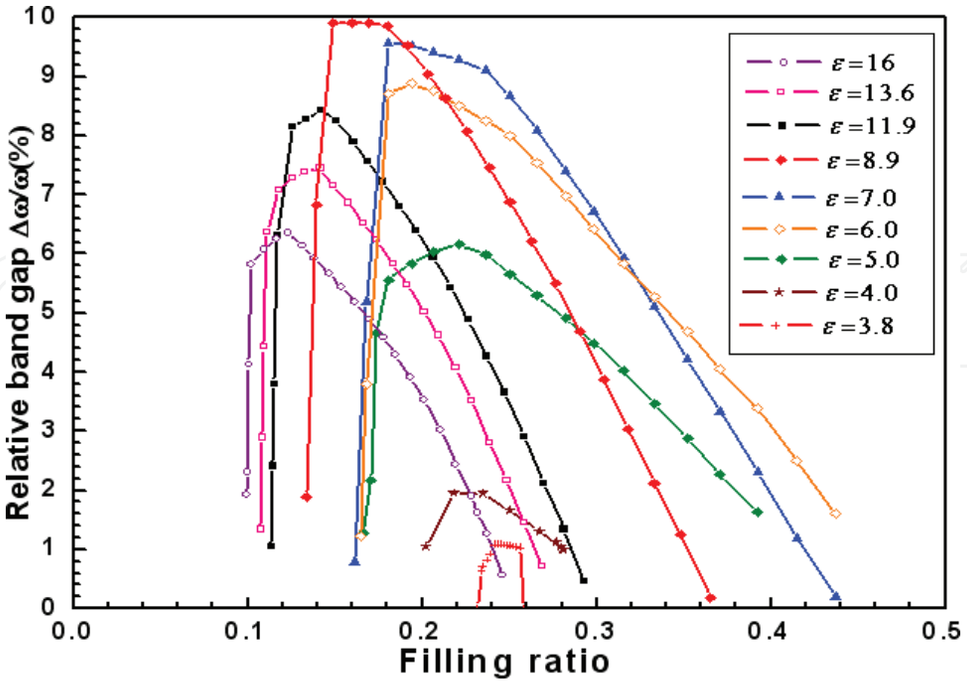

Figure 4. The relations of relative band gaps to different filling ratios *f*.

normal structure exist over wide ranges of coefficient c, filling ratio f and dielectric constant, which can relax the experimental conditions greatly.

2.2. Photonic band gap in 3D-PhCs

An important way to make 3D PhCs by HL is the interference of four umbrellalike beams (IFUB) where three ambient beams (A-beams) form the same apex angle θ with a central beam (C-beam), as shown in **Figure 5** [28, 29]. The possible lattices that IFUB may produce and the polarization optimization in the formation of different lattices have been discussed in the previous works [30, 31]. As a special case of IFUB, the symmetric umbrella configuration, where any two of the three A-beams also form the same angle, is widely used in HL since it can be conveniently realized with the use of a diffraction beam splitter (DBS). The continuous increasing of apex angle θ leads to continuous variation of primitive vectors, reciprocal vectors and the irreducible Brillouin zone of the resultant structure.

The interference of four noncoplanar plane waves of the same frequency will result in an intensity distribution

$$I = I_0 + 2\Delta I(\boldsymbol{r}), \tag{2}$$

where

$$I_0 = \sum_{j=1}^{4} E_j^2, \quad \Delta I(\boldsymbol{r}) = \sum_{i<j} E_i E_j e_{ij} \cos\left[\left(\boldsymbol{K}_i - \boldsymbol{K}_j\right) \cdot \boldsymbol{r} + \phi_{i0} - \phi_{j0} + \sigma_{ij}\right], \tag{3}$$

I_0 is the background intensity, ΔI is the spatial variation of intensity, φ_{j0} is initial phase of the jth wave, $e_{ij} = |\boldsymbol{e}_i \cdot \boldsymbol{e}_j^*|$, and $\sigma_{ij} = \arg(\boldsymbol{e}_i \cdot \boldsymbol{e}_j^*)$. The four wave vectors are expressed as functions of the apex angle θ,

$$\begin{aligned}
\boldsymbol{K}_1 &= (2\pi/\lambda)\left(\left(\sqrt{3}/2\right)\sin\theta, -(1/2)\sin\theta, \cos\theta\right),\\
\boldsymbol{K}_2 &= (2\pi/\lambda)\left(-\left(\sqrt{3}/2\right)\sin\theta, -(1/2)\sin\theta, \cos\theta\right),\\
\boldsymbol{K}_3 &= (2\pi/\lambda)(0, \sin\theta, \cos\theta),\\
\boldsymbol{K}_4 &= (2\pi/\lambda)(0, 0, 1).
\end{aligned} \tag{4}$$

With the angle θ increasing from zero to 180°, the shape of Brillouin zone changes from a small hexangular plane spreading out on xy plane to a simple cubic at $\theta = 70.53°$ and finally to a long hexangular pillar along z axis. **Figure 6** gives the lattice structure and the Brillouin zone calculated at the special angles θ. The special case of $\theta = 38.94°$ corresponds to the fcc structure which belongs to space group No. 166 ($R\bar{3}m$), the structure of $\theta = 109.47°$ is approximate to Schwarz's triply periodic minimal D surface [32].

The plane-wave expansion method [18] was used to study the PBG properties of structures of this kind and search for the corresponding optimum volume filling ratio f yielding maximum relative PBGs. **Figure 7** shows the maximum size of the relative PBG for the optimum filling ratio at different apex angle θ. The complete PBGs exist over a very

http://dx.doi.org/10.5772/intechopen.71403

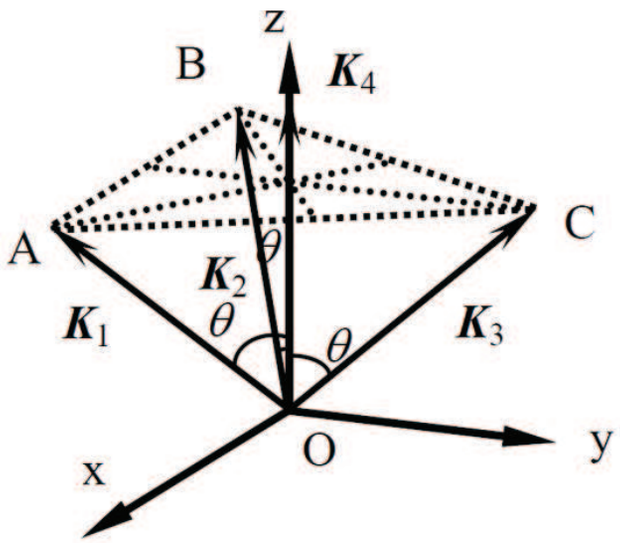

Figure 5. Symmetric umbrella recording geometry and the coordinate system used for calculations.

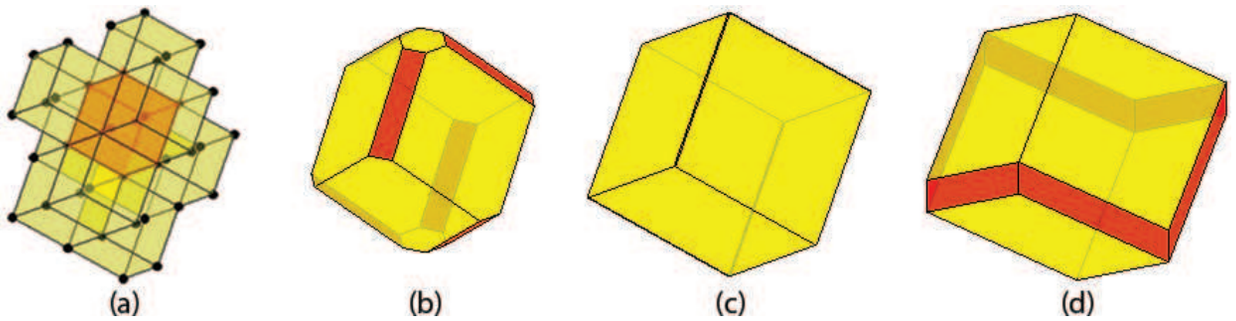

Figure 6. (a) The lattice structure at $\theta = 70.53°$ and (b) the irreducible Brillouin zones of rhombohedral structures for $\theta = 60°$, (c) $\theta = 70.53°$ and (d) $\theta = 80°$.

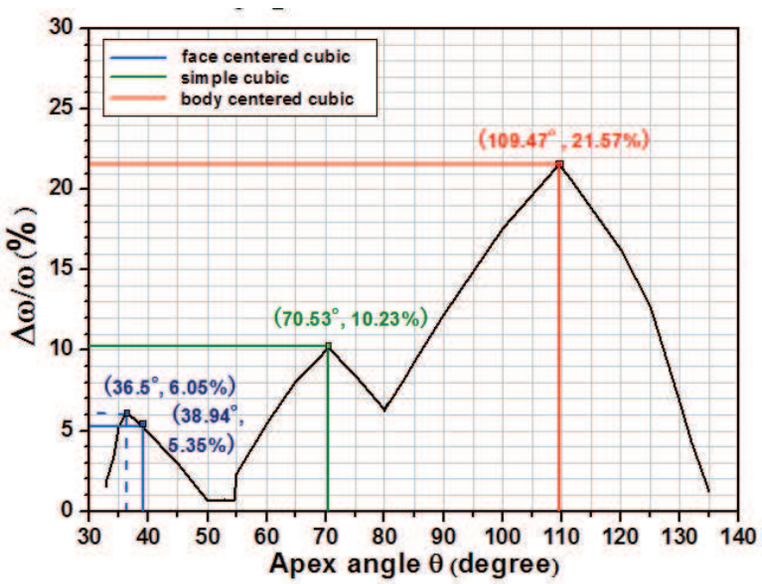

Figure 7. Relative band gap of optimized structures as function of apex angle for $33° < \theta < 135°$ when $\varepsilon = 11.9$.

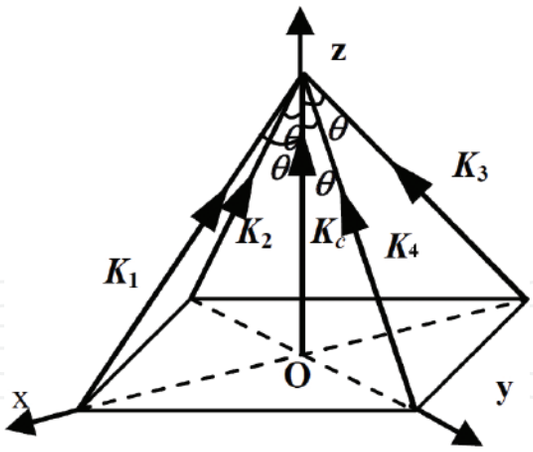

Figure 8. Symmetric umbrella recording geometry and the coordinate system used for calculations.

wide range of apex angle from 33 to 135° except the narrow region from 49 to 55°, and the resultant PBGs of simple cubic-sc, face centered cubic-fcc and body centered cubic-bcc accord with the previous works nicely [32]. The relative PBG width is a continuous function of apex angle with three peaks, and the PBG gradually decreases to zero at θ = 33° and 135°. The first peak of 6.05% corresponds to the rhombohedral structure appears at θ = 36.5°. The second of 10.23% corresponding to the sc structure occurs at θ = 70.53°; and the third one of 21.57% corresponds to the bcc structure at θ = 109.47°.

As mentioned above, the fcc lattice can be obtained by the interference of one central beam and three ambient beams symmetrically scattered around the former, but the structure made in this geometry has only quite a narrow PBG of 5.35%. An alternative beam design was proposed to fabricate the fcc lattice with a large complete PBG, but it requires four beams incident from two opposite surfaces of a sample [33], making it difficult to realize in practice. So a five-beam symmetric umbrella configuration is proposed to make 3D PhCs with large complete PBGs. The proposed recording geometry of five-beam symmetric umbrella configuration is shown in **Figure 8**, where the central beam (C-beam) is set along the z direction, while the four ambient beams (A-beams) are in the *yoz* and *xoz* planes, respectively, to form the same apex angle θ. The above mentioned five wave vectors can be expressed as,

$$\begin{aligned} &\boldsymbol{K}_1 = (2\pi/\lambda)(-\sin\theta,\ 0,\ \cos\theta), \quad \boldsymbol{K}_2 = (2\pi/\lambda)(0,\ \sin\theta,\ \cos\theta), \\ &\boldsymbol{K}_3 = (2\pi/\lambda)(\sin\theta,\ 0,\ \cos\theta), \quad \boldsymbol{K}_4 = (2\pi/\lambda)(0,\ -\sin\theta,\ \cos\theta), \\ &\boldsymbol{K}_c = (2\pi/\lambda)(0,\ 0,\ 1). \end{aligned} \tag{5}$$

This geometry can be realized by using a DBS to obtain a zero-order diffracted beam and four symmetric first-order diffracted beams. The polarization of the central beam is circularly polarized and all the four A-beams are linearly polarized. The unit polarization vectors of five beams are

$$\boldsymbol{e}_1 = \boldsymbol{e}_3 = (0,\ 1,\ 0) \quad , \quad \boldsymbol{e}_2 = \boldsymbol{e}_4 = (1,\ 0,\ 0) \quad , \quad \boldsymbol{e}_c = \frac{1}{\sqrt{2}}(1,\ -i,\ 0), \text{respectively} \tag{6}$$

In general, the lattice structures are tetragonal symmetric structures. The continuous increase of apex angle θ leads to continuous variation of primitive vectors, reciprocal vectors and the

irreducible Brillouin zone of the resultant structure. At $\theta = 70.53°$, the structure is fcc symmetry with respect to diamond structure. Around 70.53°, the lattice is face-centered-tetragonal (fct) symmetry. **Figure 9(a)** and **(b)** show the real fcc structure and its primitive cell fabricated by five-beam symmetric umbrella configuration at $\theta = 70.53°$, which obviously differ from the rhombohedral structure of fcc symmetry and its primitive cell formed by four-beam symmetric umbrella configuration at $\theta = 38.94°$, as shown in **Figure 9(c)** and **(d)**. At the apex angle of $\theta = 90°$, the body-centered-cubic (bcc) lattice can be obtained. For value of θ is near 90°, the structure has body-centered-tetragonal (bct) symmetry.

Full photonic band gaps exist over a very wide range of apex angle with a relatively low refractive index contrast. **Figure 10** represents the relative gap sizes of optimized structures for the apex angle range of $50° < \theta < 115°$ with a dielectric constant contrast of 11.9 to 1 corresponding to silicon in air. It is clear that there are complete PBGs above 10% in the range of $52° < \theta < 112°$, and even larger PBGs above 20% for $59° < \theta < 92°$. The maximum relative gap size of 25.1% appears at $\theta = 70.53°$ corresponding to fcc structure, and the relative gap size of

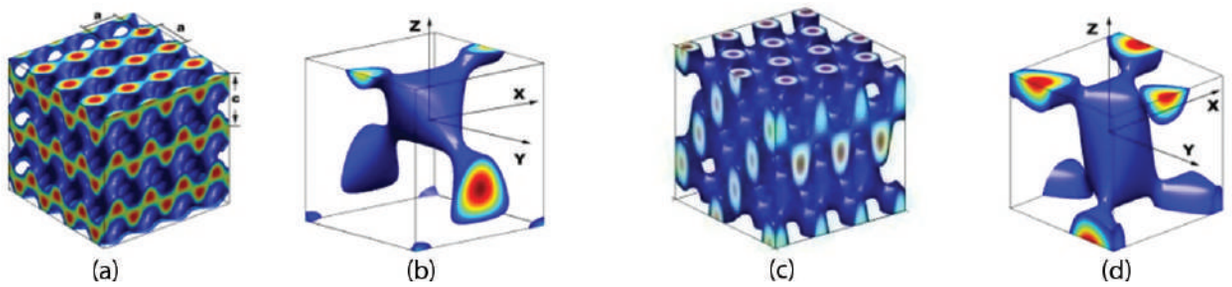

Figure 9. (a) The real fcc structure formed by five-beam symmetric umbrella configuration at $\theta = 70.53°$ and $I_t = 1.39$; (b) the primitive cell of fcc structure; (c) the rhombohedral structure of fcc symmetry constructed by four-beam symmetric umbrella configuration for $\theta = 38.94°$; and (d) the primitive cell of the lattice structure of (c).

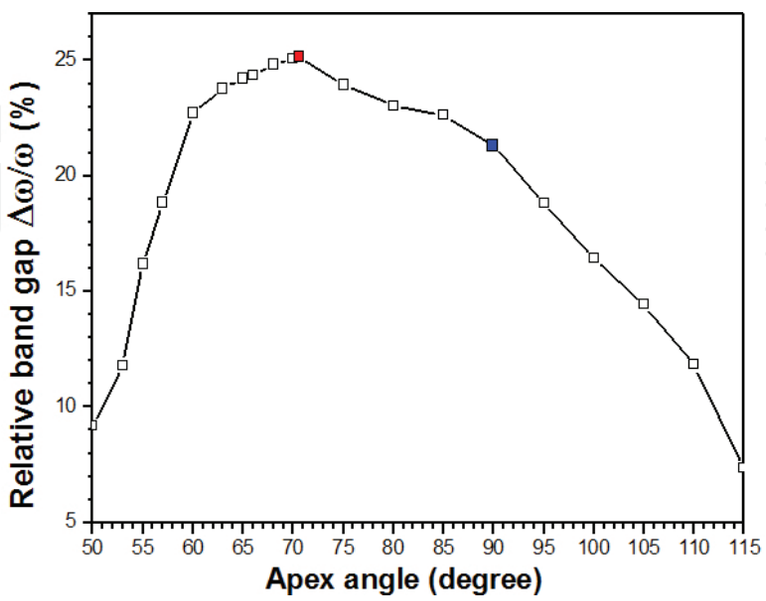

Figure 10. Relative band gap for $50° < \theta < 115°$ when $\varepsilon = 11.9$. The solid symbols are the date for fcc and bcc structures at $\theta = 70.53°$ and 90°, respectively.

bcc structure is 21.3% at $\theta = 90°$. **Figure 11** gives the band structure of the fcc lattice with a large PBG from 0.330 to 0.425$\omega a/2\pi c$ between the second and third bands. Comparing with the four-beam symmetric umbrella configuration, one can find that two results have the similar PBGs of 21.3% for the bcc lattice structures, and the biggest PBG of 25.1% for fcc lattice structure formed by five umbrellalike beams is much larger than the value of 5.35% formed by four umbrellalike beams for the shape reason of PhC lattice cell.

2.3. Photonic crystal waveguide

A waveguide can be created in the PhC slab by introducing a linear defect in the in-plane 2D periodic structure [34, 35]. Since the ability to guide light waves around sharp corners with high efficiency is crucial for photonic integrated circuits, many studies have been carried out concerning waveguide bends through sharp bends in 2D PhC slabs [36, 37]. However, all these works limit the studies to the structures formed by air rods with regular circular cross sections. PBGs for PhCs made by HL may be different from those of regular structures, so will the propagation properties.

When the 2D periodic structure is a triangular Bravais lattice formed by the interference technique of three noncoplanar beams [26], the structure was filled with a material of high refractive index and then removing the template, an inverse structure can be obtained. When the intensity threshold I_t changes from 3.0 to 2.1, the shape of air holes of this inverse structure changes gradually from a circle to a hexagon approximately. a waveguide with two 60° bends are shown in **Figure 12(a)** with the distance between two bends of 9*a*.

Some peaks of transmission may result from the resonance between two bends in the waveguide of ordinary PhCs with circular air holes [38]. The band diagram of the PhC configuration has been calculated with the intensity threshold of $I_t = 2.5$ and filling ratio of $f = 48.7\%$ for the TE-like mode. **Figure 12(b)** indicates the transmission and reflection spectra of the waveguide.

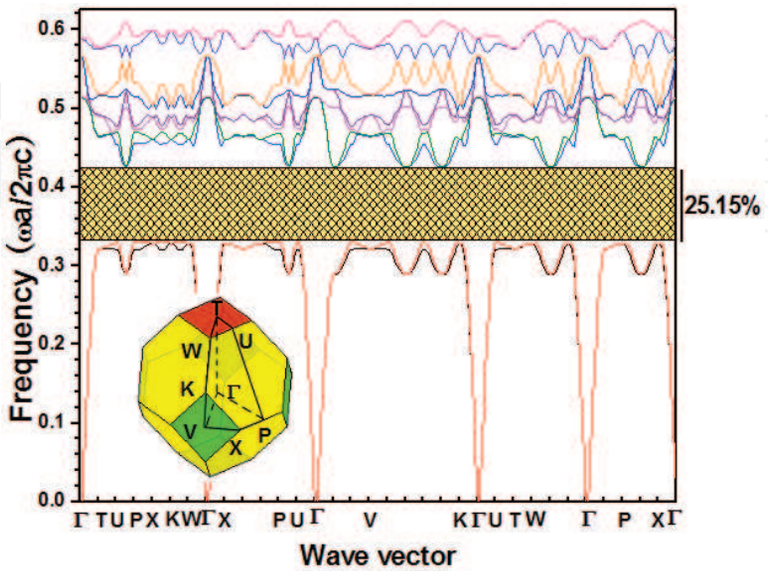

Figure 11. Photonic band structure for the fcc structure with θ = 70.53°. The position of the high symmetry points together with the irreducible Brillouin zone are shown in the inset.

http://dx.doi.org/10.5772/intechopen.71403

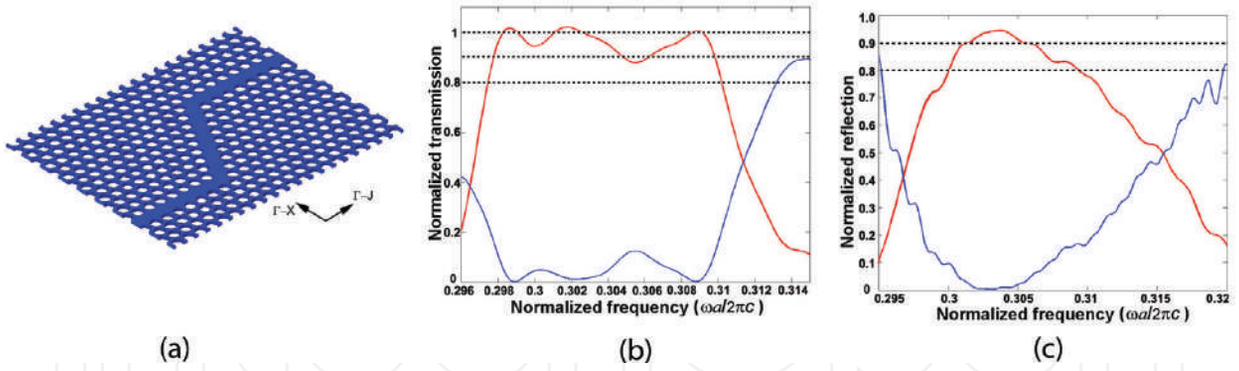

Figure 12. (a) Schematic of a 2D PhC waveguide with two 60° bends and transmission (red curve) and reflection spectra (blue curve) of the PhC waveguide (b) with two bends and (c) one bend.

The red curve here corresponds to the transmission spectra and the blue one to the reflection spectra. High transmission of more than 90% can be obtained in a wide frequency range from 0.298 to 0.310 ($\omega a/2\pi c$). The transmission spectrum of similar PCW with sole 60° bend is shown in **Figure 12(b)**. It is clear that the frequency range of high transmission (>90%) of **Figure 12(b)** is much wider than **Figure 12(c)**. This difference convincingly demonstrates that the existing resonance between two bends induce strong effect on the transmission property of the PCW, which can be used to optimize the PCW design effectively.

Different from the total internal reflection and photonic crystal fibers (PCF) with full 2D PBGs by introducing line defect, a 2D photonic crystal waveguide (PCW) formed by an air core and two identical semi-infinite layers of left-handed holographic PhC is proposed to confine light in air waveguide. As shown in **Figure 13**, The EFCs plot and wave-vector diagram of TM2 band in the HL photonic crystal indicate the PhC is left-handed. Considering the symmetry of Bloch modes of this PhC, the incident interface can be placed in ΓM or ΓK directions. Simulations have demonstrated that the incident beam can readily travel through the PhC slab with the input surface interface normal to ΓM direction, but restrained in ΓK direction, which may originate from the symmetry mismatch between the external incident wave and the Bloch mode of this PhC structure [39].

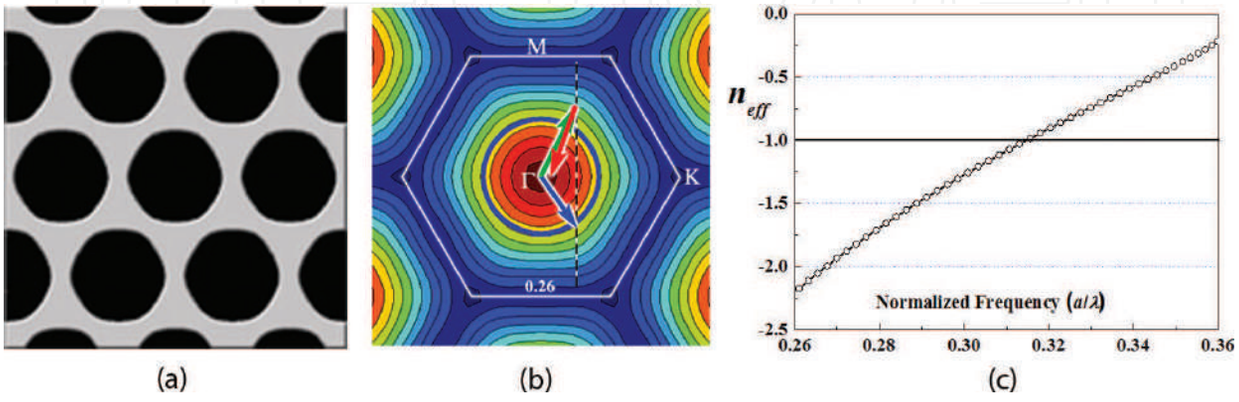

Figure 13. (a) The dielectric pattern of cross section with $I_t = 2.33$; (b) EFC plot and wave-vector diagram of TM2 band; (c) effective index of TM2 band vs. the normalized frequency.

An air waveguide is introduced in the PhC along ΓK direction, as shown in **Figure 14(a)**, with the length 50*a* of PCW. The power flow can become negative in the PhC cladding when $\varepsilon_x < 0$, but remain positive in the air core. By reducing the air width to a critical thickness for TM mode at certain frequency, the group velocity decreases to zero due to the energy flow in the air core was offset by the energy flow of the PhC cladding [39]. According to the result of Ref. [40] the wave vector of guided waves can be given by $k_z = m\pi/d$ with $m = 1,2,\ldots$, and the guided waves can pass through the super waveguide composed of one air layer and LHM for the width of air waveguide $d > \lambda_0/2$ (λ_0 is the wavelength in air). The larger d is, the more modes are guided in the super waveguide. To satisfy the guided condition the width of air layer d is chosen to be equal or greater than that of 2 layers. A Gaussian pulse with the frequency spanning from 0.26 to 0.38 is excited at the input (left) side of the waveguide to investigate the transmission properties of this holographic PCW. The transmission spectrums of different widths of air waveguides are shown in **Figure 14(b)**. Obviously, a high transmission (>90%) happened in the frequency regime from 0.315 to 0.365 through the air waveguide with the width of 4 layers, corresponding to $0 < |n_{eff}| < 1$, which verifies the oscillating modes has a real propagation constant [40]. With the width of air waveguide reducing from 4 to 2 layers, the group velocities decrease gradually and backscattering loss becomes the dominant factor [41], the critical excitation frequency changes from 0.315 to 0.334 and the transmittance decreases gradually for the backscattering loss weakening the guided Bloch mode.

Figure 15 shows TM field in the waveguide with 3 layers of air width for the cases when frequencies are (a) 0.28, (b) 0.315 and (c) 0.33 respectively, light attenuation can be seen clearly in **Figure 15(a)** as a result of vertical scattering loss. Since air thickness decreases from 4 layers to 3 layers, the group velocities slow down and the backscattering loss becomes a dominant loss factor. The light with the frequency of 0.315 display a low transmission in the waveguide as shown in **Figure 15(b)**. **Figure 15(c)** verifies that the incident wave with frequency beyond the minimum critical excitation frequency can be well confined to the air waveguide. Based on the symmetry mismatch between the incident wave and the Bloch modes of the holographic PhC, a holographic PCW without PBGs can also efficiently guide light in a wide frequency region with high transmission efficiency.

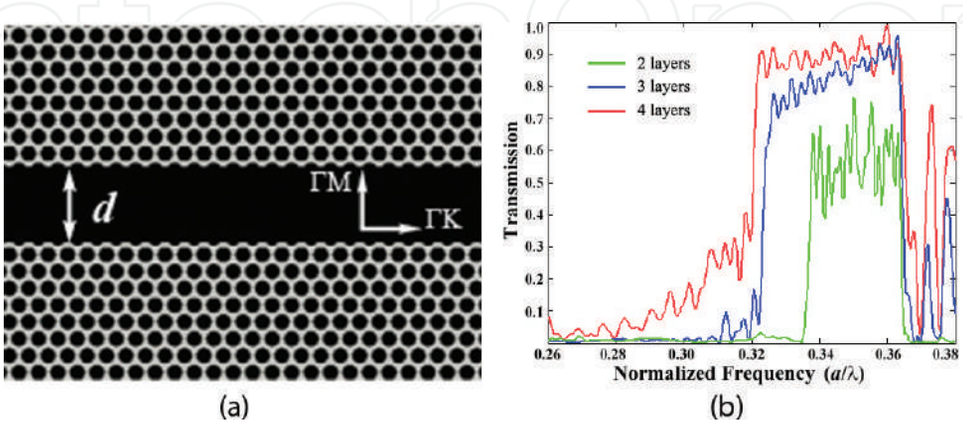

Figure 14. (a) Schematic of the holographic PhC waveguide with a 4 layers width; (b) variation of transmission spectrum for the holographic PCW with different air width.

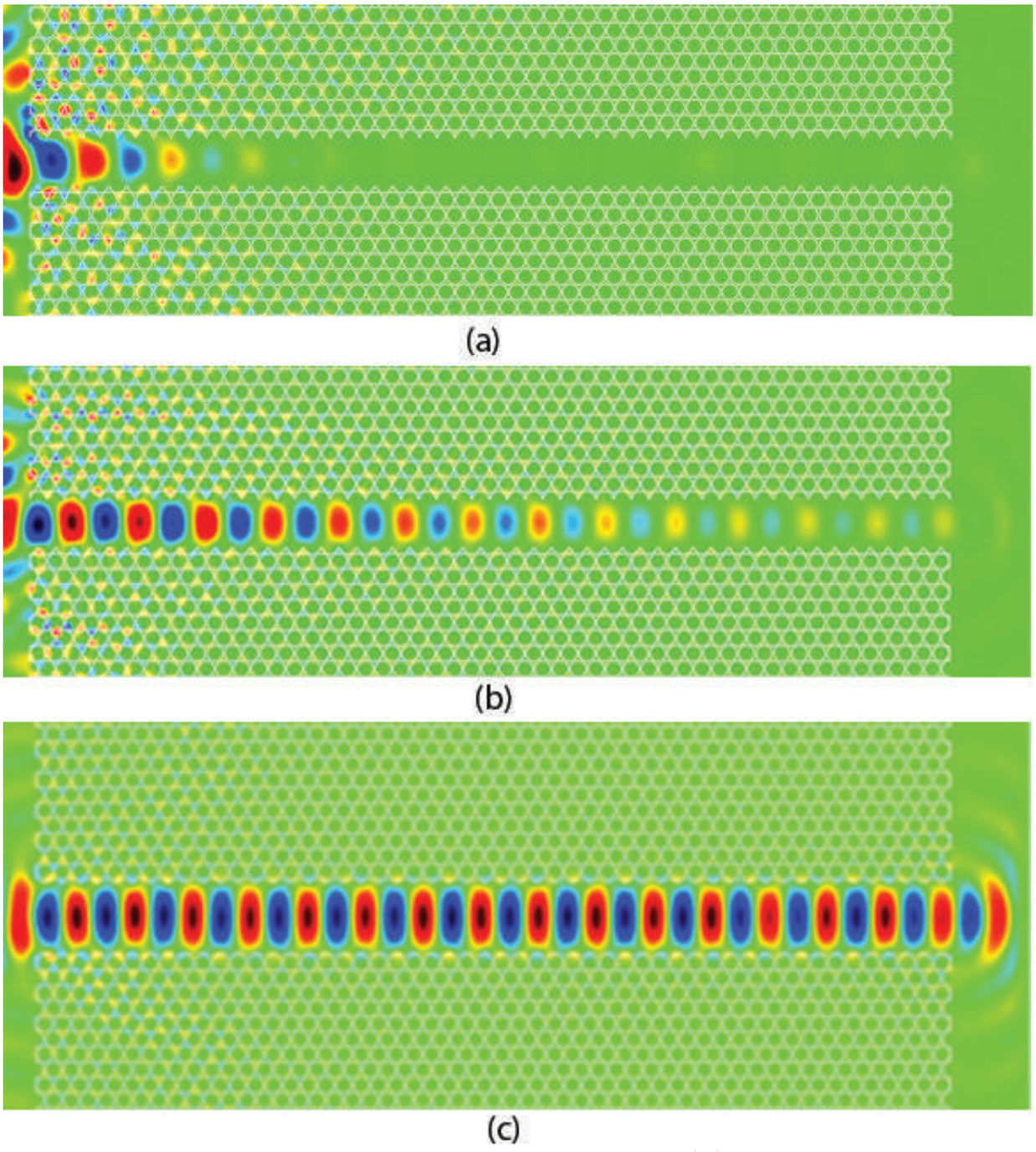

Figure 15. Snapshots of the propagations of TM polarization monochromatic wave at the frequencies of (a) 0.28, (b) 0.315 and (c) 0.33 in the holographic PCW of I_t = 2.33 with 3 layers width.

3. Anomalous refraction behaviors modulated by PhC bands

Photonic crystals can exhibit an extraordinarily high, nonlinear dispersion such as negative refraction and self-focusing properties that are solely determined by the characteristics of their band structures and equal frequency contours (EFC) [42–44]. The 2D honeycomb structures

formed by single-exposure interference fabrication methods is used to investigate a series of HL PhC structures in order to obtain comprehensive understanding of the anomalous refractive properties in PhCs.

The filling ratio of the HL PhC is determined by the ratio of the total exposure dose. Silicon with $\varepsilon = 11.56$ (i.e., $n = 3.4$) is used to analyze the dispersion characteristics of the holographic PhCs. **Figure 16(a)** gives the cross section of the HL PhC sample. The EFCs plot and wave-vector diagram of TM2 band in **Figure 16(b)** illustrated the EFCs around point Γ are convex and shrink with increasing frequency, indicating the PhC is left-handed. Due to the symmetry mismatch between the external plane wave at normal incidence and the Bloch modes of this PhC as mentioned above, the interface between PhC and free space is arranged along the ΓK direction.

As shown in **Figure 16(a)**, the surface of dielectric PhC slab with the trigonal flange (cut $0.4a$) was disposed to reduce the reflection and scattering losses effectively [45], because of the effective index gradually varying to match with free space. A continuous monochromatic TM polarization plane wave at the desired frequency $\omega = 0.348$ incidents on the PhC slab with the incident angles of $\theta = 30^\circ$ and 60°. The wave patterns are shown in **Figure 16(c)** and **(d)**, respectively, with the refracted beams and incident beams symmetrically located on the same side of normals, which illustrate the effective refractive index of this PhC is $n_{\text{eff}} = -1$, and the phenomenon of negative refraction in this PhC is an absolute left-handed behavior with $\boldsymbol{K}_{\text{r}} \cdot \boldsymbol{V}_{\text{gr}} < 0$.

For a continuous point source of $\omega = 0.348$ located on the upper side of the PhC slab with the distance of $d_{\text{o1}} = 8.0a$ away from the upper interface (i.e., the object distance), as shown in **Figure 17(a)**, the image point approximately locates at the edge of the lower surface with the image distance $d_{\text{i1}} = 0$. In **Figure 17(b)**, the relevant image distance becomes $d_{\text{i2}} \approx 4.6a$ for the object distance of $d_{\text{o2}} = 3.5a$. Obviously, the sum of d_{o} and d_{i} in this PhC slab is nearly a constant and satisfies the Snell's law of a flat lens with $n_{\text{eff}} = 1$. In addition, note that there is an internal focus inside the PhC slab of **Figure 17(b)**, which is a clear evidence of LHMs following the geometric optics rules.

Multi-refraction effects in the 2D triangular PhC have also been found [43]. The special EFC distributions of different bands can be used to predicate the propagating properties of incident electromagnetic wave (EMW). The EFC plot of the second band is shown in **Figure 18(a)** with almost straight EFC in the ΓK direction at the frequency of 0.26 a/λ. The group velocity v_{gr} of refracted waves ought to be perpendicular to the incident surface among the incident angle region from 0 to 35°, which have been demonstrated by the simulation results in **Figure 18(b)–(d)**. This unusual collimation effect has a series of exciting potential applications, such as spatial light modulator and optical collimator.

The k-conservation relation is observed in wave-vector diagrams [44]. Traditional EMWs propagate in media with their wavefronts perpendicular to the energy flow direction. Here, the EMW of 0.36 a/λ incident upon the ΓK surface at $\theta_{inc} = 25^\circ$, the wavefronts of refracted wave are modulated by the periodic PhC to parallel to the energy flow direction with $\boldsymbol{k} \cdot \boldsymbol{v}_{gr} = 0$. **Figure 19(a)** gives the analysis of EFC plot and wave-vector diagram. FDTD simulations of electric field distribution in **Figure 19(b)** prove with the certainty of theory analysis results with the parallel wavefronts extending along the transmission line.

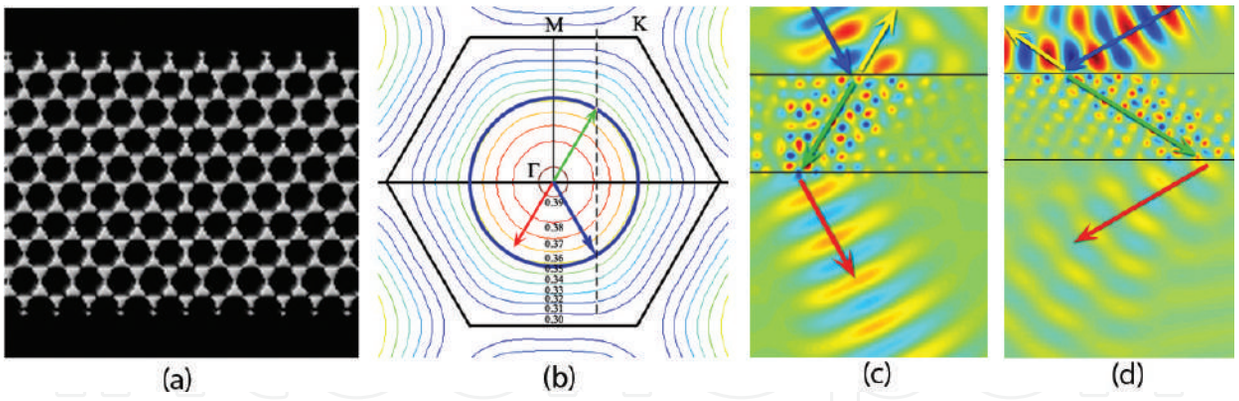

Figure 16. (a) Schematic view of the HL PhC slab with the trigonal dielectric flange; and (b) the wave patterns of negative refractions for different incident angles of (c) $\theta = 30^\circ$ and (d) $\theta = 60^\circ$.

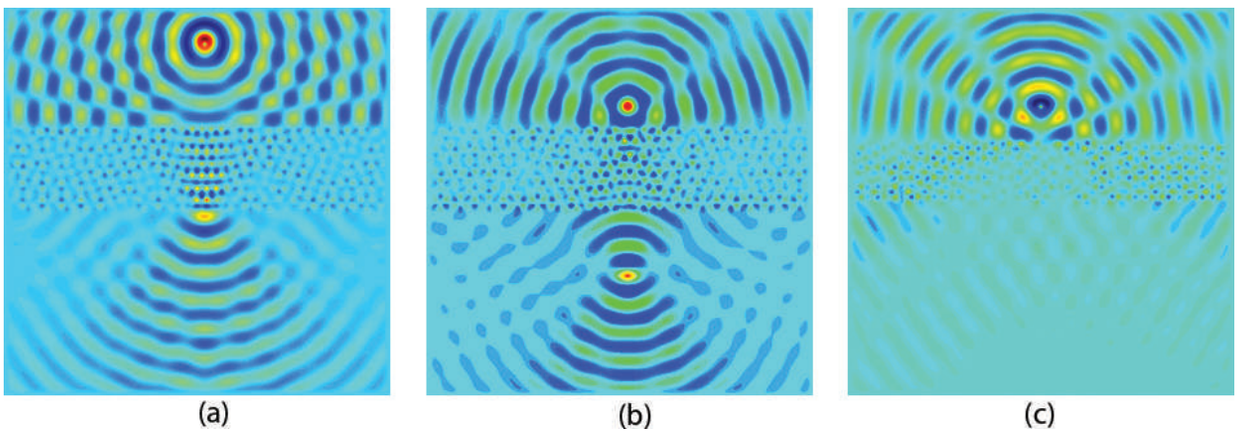

Figure 17. Field patterns for the flat superlens. The object distance is 8.5*a* (a) and 3.5*a* (b) for the interface normal to ΓM direction, and (c) 3.5*a* for the interface normal to ΓK direction.

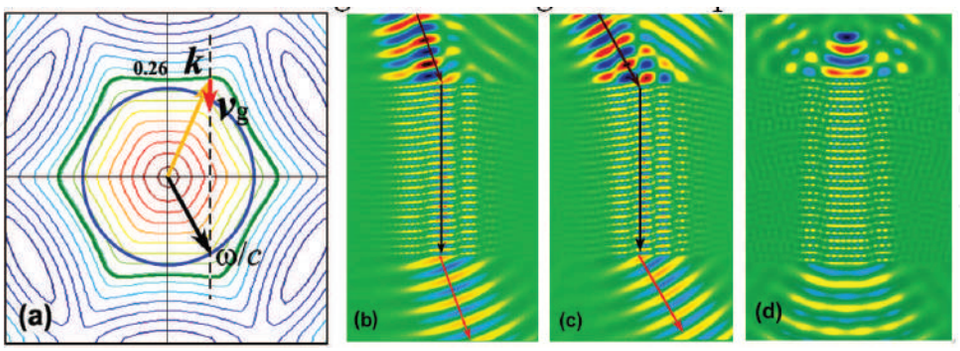

Figure 18. (a) EFC plot of the second band with the wave-vector diagrams at 0.26a/λ and the FDTD simulations of electric field distributions with different incident angles of (b) 20°, (c) 30° and (d) point source incident.

For the normal HL structure with triangular lattice symmetry of $I_t = 1.90$ (or $f = 82.8\%$), the EFC plots of TM2 and TM3 bands are calculated [46]. Different from the EFCs of inverse HL structure, TM2 and TM3 bands intersect in the frequencies regime from 0.225 to 0.343.

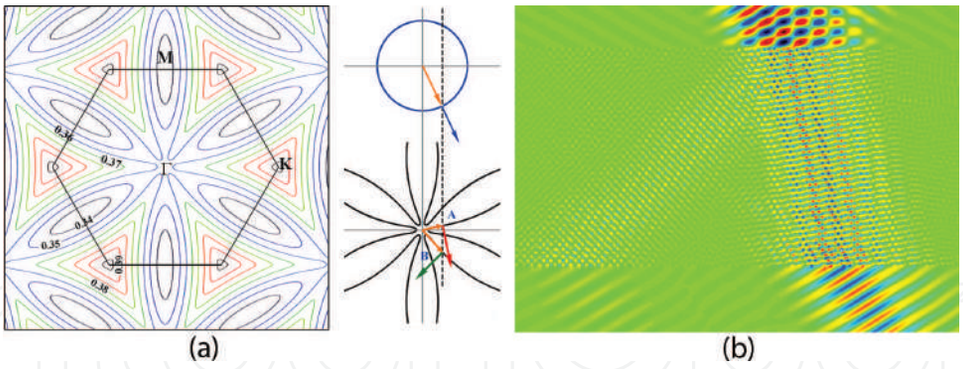

Figure 19. (a) EFC plot of the fourth band and wave-vector diagram at 0.36a/λ with $\theta_{inc} = 25°$; (b) the FDTD simulations of electric field distributions.

When a Gaussian beam of $\omega = 0.31$ incidents on the ΓK surface at $\theta = 25°$, the wave-vector diagram is shown in **Figure 20(a)** with the blue circle representing the EFC in air, the brown ring denoting the EFC of TM2 band, and the green hexagram corresponding to the EFC of TM3 band. Obviously, the dashed conservation line intersects with EFCs of TM2 and TM3 simultaneously to excite two beams of left-handed negative refraction with different refractive angles, because of the unique EFC features, as shown in **Figure 20(b)** to verify this result.

The more complicated refraction behaviors can be excited in the higher band regions based on the intricate undulation of one band or the overlap of different bands. As shown in **Figure 21(a)**, the sixth band has dual parallel EFCs with opposite curvatures by the red rings within the frequency range from 0.44 to 0.47 a/λ within a wide scope of incident angle. As an example, when the working frequency is chosen to be 0.46a/λ, the incident wave at $\theta_{inc} = 30°$ can excite positive and negative refracted waves have the symmetrical refractive angles of ±30°. The seventh band has more frequency undulations circled by the blue rings which lead to the more intricate triple refraction within the frequency scope from 0.488 to 0.50 a/λ (**Figure 21(b)**).

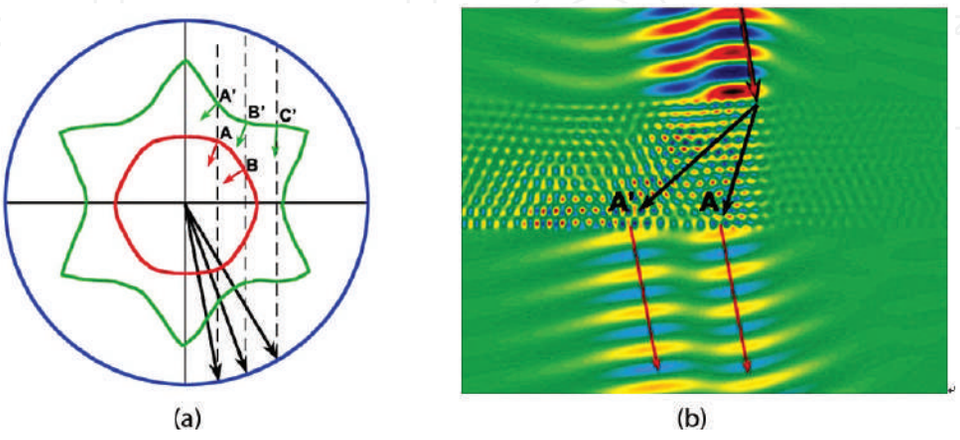

Figure 20. (a) Wave-vector diagram of $\omega = 0.31$ for TM2 (brown ring) and TM3 (green hexagram); (b) field pattern with the incident beam of $\omega = 0.31$ at the incident angle of 25°.

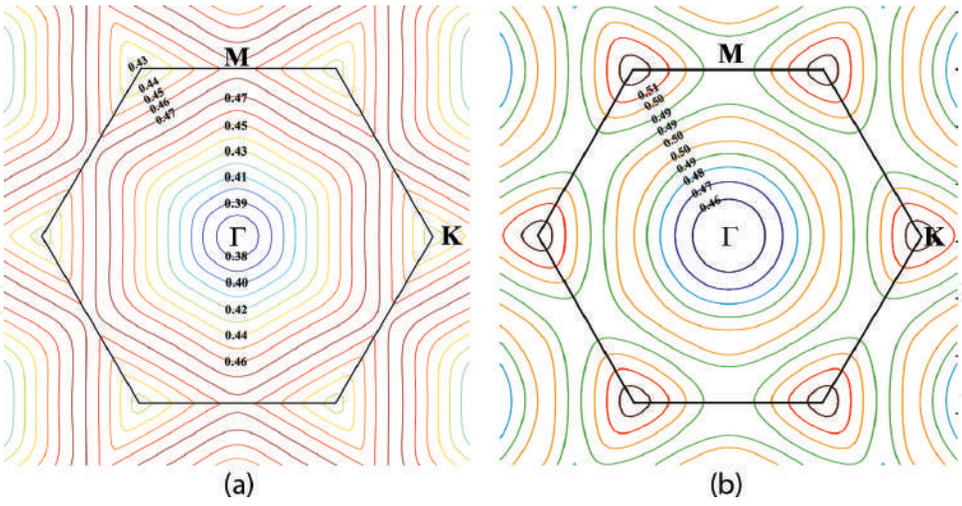

Figure 21. EFC plots of (a) the sixth band and (b) the seventh band.

4. Phenomena of zero phase delay in PhCs and application

Recently, materials with zero or near-zero-n has attracted great focus for the characteristics of uniform phase and infinite wavelength [47–50]. A series of exciting potential applications have been found in zero-n materials, such as wavefront reshaping [51], beam self-collimation [52], extremely convergent lenses [53], etc. One of their best known applications is optical links in lumped nanophotonic circuits over hundreds of wavelengths without introducing phase shifts so as to reduce the unwanted frequency dispersion. Different strategies have been provided to realize zero permittivity ε. One is to use metallic metamaterial structures with effective zero permittivity and/or permeability [54, 55]. However, these metamaterials suffer from the strong absorption loss of the metals and hence with greatly deteriorated transmittance. Some alternative approaches have been provided, include the combination of negative- and positive-index materials [52], the microwave waveguides below cutoff [56] or the periodic superlattice formed by positive index homogeneous dielectric media and negative index photonic crystals (PhCs) [57].

A plane wave can be described as $\tilde{E}(\boldsymbol{r}) = A\exp\left[i(\boldsymbol{k}\cdot\boldsymbol{r}+\varphi_0)\right]$, where the symbols of A, $\boldsymbol{k}$, $\boldsymbol{r}$, ϕ_0 denote wave amplitude, wave vector, position vector and initial phase. The spatial phase shift is determined by the spatial phase factor $\boldsymbol{k}\cdot\boldsymbol{r}$, with the traditional wave vector $\boldsymbol{k}$ pointing to the direction of energy flow (i.e. the direction of group velocity $\boldsymbol{v}_{gr}$). Assuming the condition of $\boldsymbol{k}\cdot\boldsymbol{r}=0$ is satisfied, the wave vector $\boldsymbol{k}$ is perpendicular to the energy flow with the wavefronts extending along the propagation direction with the stationary spatial phase along the direction of energy flow $\boldsymbol{S}$. In general, it is difficult to modulate the direction of wavefronts in homogeneous materials. Since this formula of $\boldsymbol{k}\cdot\boldsymbol{r}=0$ can also be expressed as $\boldsymbol{k}\cdot\boldsymbol{v}_{gr}=0$, by the definition of group velocity $\boldsymbol{v}_{gr}=\nabla_{\boldsymbol{k}}\omega$ in PhCs, the group velocity vector is perpendicular to EFCs pointing to the frequency-increasing direction. Hence, by adjusting the EFC distribution, the condition of zero phase delay with $\boldsymbol{k}\cdot\boldsymbol{r}=0$ can be satisfied.

The PhC sample of triangular lattice is composed of dielectric rods with ε_r = 10, diameter d = 10 mm, height h = 10 mm and lattice constant a = 10 mm. When the beam of the frequency ω = 0.376 is incident upon the ΓK surface with the incident angle of θ_{inc} = 30°. The wave-vector diagram of the fourth band is shown in **Figure 22**. According to the condition of boundary conservation, two refracted waves can be excited in the PhC. The condition of $\boldsymbol{k} \cdot \boldsymbol{r} = 0$ is satisfied for the positive refracted wave. Simulations and experiments in a near-field scanning system have demonstrated that the wavefronts exactly are parallel to the energy flow with zero phase delay, as shown in **Figure 23(a)** and **(b)**. The measured phase contrast image is shown in **Figure 23(c)** at 11.213 GHz. Obviously, the incident wave and the exit wave can be connected directly as if the PhC slab did not exist. Since the PhC structure can be engineered readily with the large design flexibility, the frequency and incident angle of zero phase delay can be adjustable in a relaxed PhC configuration design.

Another approach to realize zero phase delay in PhCs is based on the accidental degeneracy of two dipolar modes and a single monopole mode generates at the Dirac-like point (DLP) with the linear dispersions of Dirac cone at the Brillouin zone center of PhCs [58]. At the DLP shown in **Figure 24(a)**, the PhC can mimic the zero-index medium (ZIM) with the characteristics of uniform field distribution. Linear dispersions near the center point induced by the triple degeneracy display many unique scattering properties, such as conical diffraction [59], wave shaping and cloaking [60]. The dispersion properties obeying the 1/L scaling law near the DLP in the normal propagation direction have been verified theoretically and experimentally [61] through the dielectric PhC ribbons with the finite thicknesses, however, it is difficult to distinguish the precise crossing point from the wide extremum range just relying on the transmittance spectrum.

A Gaussian pulse source of TM mode was placed in front of a PhC square-lattice array with the incident angle of 90°, thus three transmission spectrums can be measured outside the other three output interface of the PhC array with one in parallel direction and two in perpendicular upward and downward directions. As long as the size is large enough, the PhC array can be

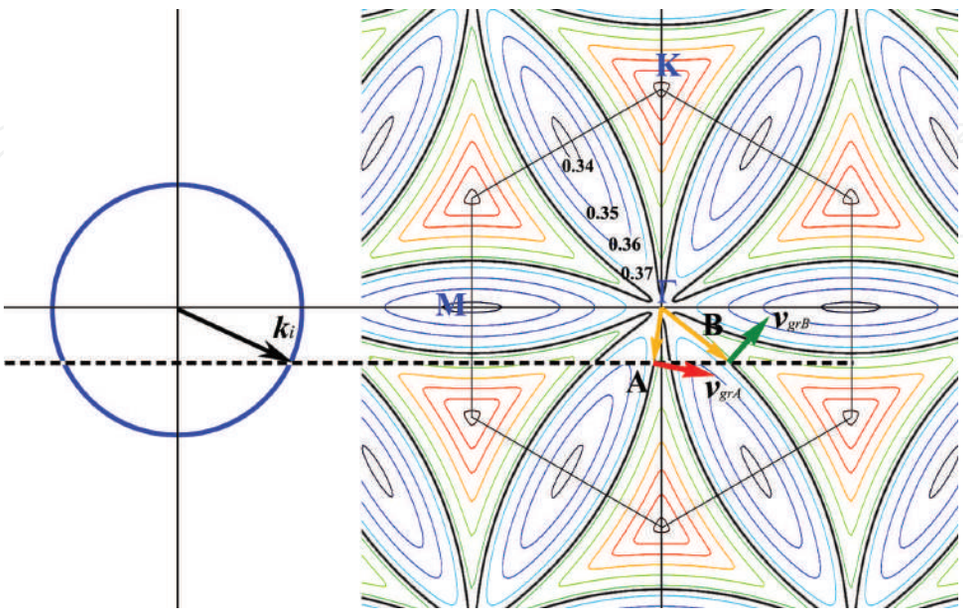

Figure 22. EFCs plot of the fourth band with the wave-vector diagram at $\omega = 0.376a/\lambda$ with θ_{inc} = 30°.

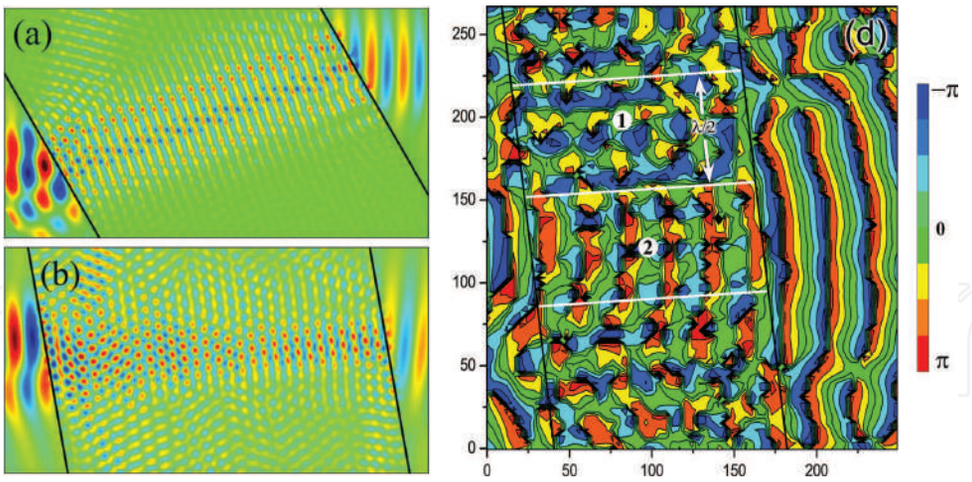

Figure 23. (a, b) Wavefront distribution in the PhC slab with different incident angles; (c) measured phase contrast image.

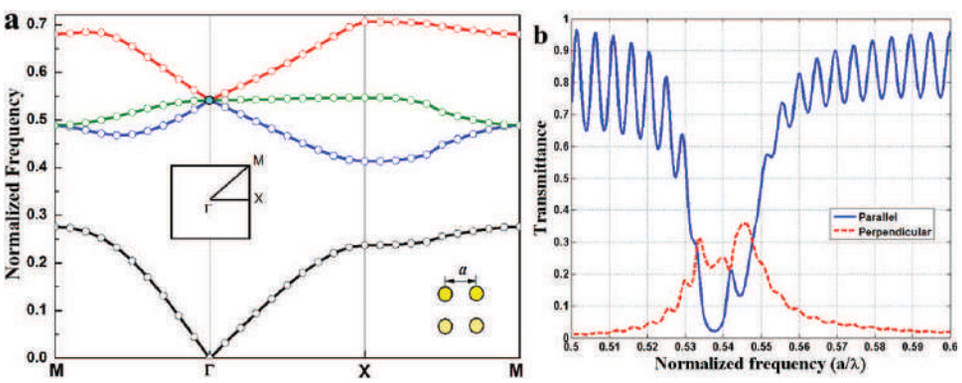

Figure 24. (a) Band structure of TM waves for the 2D square-lattice PhC at the normalized frequency $\omega_D = 0.541$. (b) The simulated transmission spectra in the directions parallel and perpendicular to the incident propagation direction.

regarded as an infinite PhC with the similar transmittance at the different exit boundaries with the same interface structure. As shown in **Figure 24(b)**, the upward and downward sharp cusps embedded in the parallel and perpendicular extremum transmittance spectra intersect at the DLP frequency, therefore, the DLP can be identified accurately due to the property of uniform field distribution of PhC with effective zero index at DLP.

5. Conclusion

In summary, some novel kinds of 3- and 2-D lattices formed by holographic lithography have been investigated to find that the complete PBG over wide ranges of system parameters can be achieved by proper design. The beam design for making this structure is also derived. By using the interference of symmetric four umbrellalike beams one can obtain complete PBGs over a very wide range of apex angle, three special lattice structures of fcc, sc and bcc were achieved with different complete PBGs of 5.35%, 10.23% and 21.57%. The similar PBG of 21.3% for the bcc lattice structures, and the biggest PBG of 25.1% for fcc lattice structure were achieved by five

umbrellalike beams, which is much larger than the value of 5.35% formed by four umbrellalike beams for the shape reason of PhC lattice cell. The holographic PCW can efficiently guide light in a wide range of frequency around sharp corners and the resonance between the two bends has a close relation with the configuration of PhC which can be regarded as an important factor to improve the transmission property of 2D PCW. Since the absolute refractive index 1 of the air guiding core is larger than the effective index of PhC cladding, the total internal reflections can be achieved approximately with a high transmittance in the PhC waveguide with the effective refraction index near zero. For PhC waveguide when the width of air layer is greater than the critical thickness, the problems of scattering loss can be avoided. The proposed left-handed holographic PCW is more suitable for many applications in the area of photonic integrated circuits, and the idea and method of analysis here open a new freedom for PCW engineering.

Different from the anomalous phenomena of PhCs in the high bands, the PhCs of honeycomb-lattice in the lower band region are more suitable to realize the effect of all-angle left-handed negative refraction. For the straight EFCs distribution in special directions, the regular PhC can be applied to the design of optical collimator. Moreover, multi-refraction has been found in the higher bands. There are two ways to realize multi-refractions, one arises from a single band with intricate undulations and another originates from the overlap of multi-bands. The unique phenomena of dual-negative refraction and positive-negative refraction have been found in the higher bands of PhC. Based on the design flexibility of PhC, the transmission properties of PhC can be engineered with a large freedom. These results are important and useful for the design of PhC device.

An efficient way to achieve EMW propagation with zero phase delay is to modulate the wavefronts paralleling to the direction of energy flow. This method can be extended from 2D to 3D cases or other artificially engineered materials, which opens a new door to obtain perfect zero-phase-delay propagation of EMW and has significant potential in many applications. Furthermore, the research found that the Dirac-like point of PhC can be identified accurately by measuring the transmission spectra through a finite photonic crystal square array.

All these results can be extended to the fabrication of other artificially engineered materials and provide guidelines to the design of new type optical devices.

Acknowledgements

This work was supported by National Natural Science Foundation of China (11574311, 51532004, 61275014)

Author details

Guoyan Dong

Address all correspondence to: gydong@ucas.ac.cn

College of Materials Science and Opto-Electronic Technology, University of Chinese Academy of Sciences, Beijing, China

References

[1] Yablonovitch E. Inhibited spontaneous emission in solid-state physics and electronics. Physical Review Letters. 1987;**58**:2059. DOI: 10.1103/PhysRevLett.58.2059

[2] Joannopoulos JD. et al. Photonic Crystals: Molding the Flow of Light. NJ, USA: Princeton University Press; 2008. DOI: 10.1016/S0038-1098(96)00716-8

[3] Johnson S, Villeneuve P, Fan S, Joannopoulos J. Linear waveguides in photonic-crystal slabs. Physical Review B. 2000;**62**:8212-8222. DOI: 10.1103/PhysRevB.62.8212

[4] Mekis A, Chen J, Kurland I, Fan S, Villeneuve P, Joannopoulos J. High transmission through sharp bends in photonic crystal waveguides. Physical Review Letters. 1996;**77**:3787. DOI: 10.1103/PhysRevLett.77.3787

[5] Krauss T, Rue R, Brand S. Two-dimensional photonic-bandgap structures operating at near-infrared wavelengths. Nature. 1996;**383**:699-702. DOI: 10.1038/383699a0

[6] Zhang X, Jackson T, Lafond E, Deymier P, Vasseur J. Evidence of surface acoustic wave band gaps in the phononic crystals created on thin plates. Applied Physics Letters. 2006;**88**:041911. DOI: 10.1063/1.2167794

[7] Aoki K, Miyazaki H, Hirayama H, Inoshita K, Baba T, Sakoda K, Shinya N, Aoyagi Y. Microassembly of semiconductor three-dimensional photonic crystals. Nature Materials. 2003;**2**:117-121. DOI: 10.1038/nmat802

[8] Moroz A. Three-dimensional complete photonic-band-gap structures in the visible. Physical Review Letters. 1999;**83**:5274-5277. DOI: 10.1103/PhysRevLett.83.5274

[9] Liu K, Avouris P, Bucchignano J, Martel R, Sun S, Michl J. Simple fabrication scheme for sub-10 nm electrode gaps using electron-beam lithography. Applied Physics Letters. 2002;**80**:865-867. DOI: 10.1063/1.1436275

[10] Farsari M, Vamvakaki M, Chichkov B. Multiphoton polymerization of hybrid materials. Journal of Optics. 2010;**12**:124001. DOI: 10.1088/2040-8978/12/12/124001

[11] Miklyaev Y, Meisel D, Blanco A, Freymann G. Three-dimensional face-centered-cubic photonic crystal templates by laser holography: Fabrication, optical characterization, and band-structure calculations. Applied Physics Letters. 2003;**82**:1284-1286. DOI: 10.1063/1.1557328

[12] Veselago V, Lebedev P. The electrodynamics of substances with simultaneously negative values of ε and μ. Soviet Physics Uspekhi. 1968;**10**:509-514. DOI: 10.1070/PU1968v010n04ABEH003699

[13] Ziolkowski R, Heyman E. Wave propagation in media having negative permittivity and permeability. Physical Review E. 2001;**64**:056625. DOI: 10.1103/PhysRevE.64.056625

[14] Lindell I, Tretyakov S, Nikoskinen K, Ilvonen S. BW media—media with negative parameters, capable of supporting backward waves. Microwave & Optical Technology Letters. 2001;**31**:129-133. DOI: 10.1002/mop.1378

[15] Shelby R, Smith D, Schultz S. Experimental verification of a negative index of refraction. Science. 2001;**292**:77-79. DOI: 10.1126/science.1058847

[16] Rakich P, Dahlem M, Tandon S, et al. Achieving centimetre-scale supercollimation in a large-area two-dimensional photonic crystal. Nature Materials. 2006;**5**:93. DOI: 10.1038/005093a0

[17] Vasić B, Gajić R. Self-focusing media using graded photonic crystals: Focusing, Fourier transforming and imaging, directive emission, and directional cloaking. Journal of Applied Physics. 2011;**110**:1771-1180. DOI: 10.1063/1.3630116

[18] Cao Y, Hou Z, Liu Y. Convergence problem of plane-wave expansion method for phononic crystals. Physics Letters A. 2004;**327**:247-253. DOI: 10.1016/j.physleta.2004.05.030

[19] Bondeson A, Rylander T, Ingelström P. The finite-difference time-domain method. In: Computational Electromagnetics. Vol. 51. New York, NY: Springer; 2001. pp. 57-86. DOI: 10.1007/0-387-26160-5_5

[20] Dong G, Yang X, Cai L, Shen X, Meng X, Xu X, Wang Y. Band gap analysis and holographic design of 3-fold hybrid triangular photonic crystals of irregular columns with large full band gaps. Journal of Optics A: Pure and Applied Optics. 2007;**9**:531. DOI: 10.1088/1464-4258/9/5/017

[21] Dong G, Yang X, Cai L, Shen X, Meng X, Xu X, Zhang H. Six-fold hybrid photonic crystal formed holographically with full band gap for low refractive index. EPL. 2007;**80**:14006. DOI: 10.1209/0295-5075/80/14006

[22] Cai L, Dong G, Feng C, Yang X, Shen X, Meng X. Holographic design of a two-dimensional photonic crystal of square lattice with a large two-dimensional complete bandgap. Journal of the Optical Society of America B. 2006;**23**:1708-1711. DOI: 10.1364/JOSAB.23.001708

[23] Joannopoulos J, Villeneuve P, Fan S. Erratum: Photonic crystals: Putting a new twist on light. Nature. 1997;**386**:143-149. DOI: 10.1038/386143a0

[24] Russell P. Photonic crystal fibers. Science. 2003;**299**:358. DOI: 10.1126/science.1079280

[25] Sharp D, Campbell M, Dedman E, Harrison M, Denning R, Turberfield A. Photonic crystals for the visible spectrum by holographic lithography. Nature. 2000;**404**:53. DOI: 10.1038/35003523

[26] Yang X, Cai L, Liu Q. Theoretical bandgap modeling of two-dimensional triangular photonic crystals formed by interference technique of three-noncoplanar beams. Optics Express. 2003;**11**:1050-1055. DOI: 10.1364/OE.11.001050

[27] Cai L, Feng C, He M, Yang X, Meng X, Dong G, Yu X. Holographic design of a two-dimensional photonic crystal of square lattice with pincushion columns and large complete band gaps. Optics Express. 2005;**13**:4325. DOI: 10.1364/OPEX.13.004325

[28] Dong G, Cai L, Yang X, Shen X, Meng X, Xu X, Wang Y. Analysis of structure and band gap evolution of photonic crystals formed holographically by symmetric umbrella configuration

with varying apex angles. Journal of Physics D: Applied Physics. 2006;**39**:3566. DOI: 10.1088/0022-3727/39/16/007

[29] Dong G, Cai L, Yang X, Shen X, Meng X, Xu X, Wang Y. Holographic design and band gap evolution of photonic crystals formed with five-beam symmetric umbrella configuration. Optics Express. 2006;**14**:8096-8102. DOI: 10.1364/OE.14.008096

[30] Cai L, Liu Q, Yang X. Polarization optimization in the interference of four umbrellalike symmetric beams for making three-dimensional periodic microstructures. Applied Optics. 2002;**41**:6894. DOI: 10.1364/AO.41.006894

[31] Cai L, Yang X, Liu Q, Wang Y. What kind of Bravais lattices can be made by the interference of four umbrellalike beams? Optics Communications. 2003;**224**:243-246. DOI: 10.1016/j.optcom.2003.07.004

[32] Meisel D, Wegener M, Busch K. Three-dimensional photonic crystals by holographic lithography using the umbrella configuration: Symmetries and complete photonic band gaps. Physical Review B. 2004;**70**:165104. DOI: 10.1103/PhysRevB.70.165104

[33] Chan T, Toader O, John S. Photonic band gap templating using optical interference lithography. Physical Review E. 2005;**71**:046605. DOI: 10.1103/PhysRevE.71.046605

[34] Dong G, Yang X, Cai L, Shen X, Wang Y. Improvement of transmission properties through two-bend resonance by holographic design for a two-dimensional photonic crystal waveguide. Optics Express. 2008;**16**:15375. DOI: 10.1364/OE.16.015375

[35] Dong G, Yang X, Cai L. Transmission properties of an air waveguide with left-handed holographic photonic crystal cladding. 中国物理快报:英文版. 2011;**28**:014210. DOI: 10.1088/0256-307X/28/1/014210

[36] Cui X, Hafner C, Vahldieck R, Robin F. Sharp trench waveguide bends in dual mode operation with ultra-small photonic crystals for suppressing radiation. Optics Express. 2006;**14**:4351. DOI: 10.1364/OE.14.004351

[37] Smajic J, Hafner C, Erni D. Design and optimization of an achromatic photonic crystal bend. Optics Express. 2003;**11**:1378. DOI: 10.1364/OE.11.001378

[38] Chutinan A, Noda S. Waveguides and waveguide bends in two-dimensional photonic crystal slabs. Physical Review B. 2000;**62**:4488-4492. DOI: 10.1103/PhysRevB.62.4488

[39] Sakoda K. Optical Properties of Photonic Crystals. Berlin, Heidelberg: Springer; 2005. DOI: 10.1007/978-3-662-14324-7

[40] Cheng Q, Cui T. High-power generation and transmission through a left-handed material. Physical Review B. 2005;**72**:113112. DOI: 10.1103/PhysRevB.72.113112

[41] Jiang T, Zhao J, Feng Y. Stopping light by an air waveguide with anisotropic metamaterial cladding. Optics Express. 2009;**17**:170. DOI: 10.1364/OE.17.000170

[42] Dong G, Cai L, Yang X. Anomalous refractive effects in honeycomb lattice photonic crystals formed by holographic lithography. Optics Express. 2010;**18**:16302. DOI: 10.1364/OE.18.016302

[43] Dong G, Zhou J, Yang X, Meng X. Multi-refraction with same polarization state in two dimensional triangular photonic crystals. Progress in Electromagnetics Research. 2012;**128**: 91-103. DOI: 10.2528/PIER12040306

[44] Notomi M. Theory of light propagation in strongly modulated photonic crystals: Refractionlike behavior in the vicinity of the photonic band gap. Physical Review B. 2000; **62**:10696-10705. DOI: 10.1103/PhysRevB.62.10696

[45] Matsumoto T, Eom K, Baba T. Focusing of light by negative refraction in a photonic crystal slab superlens on silicon-on-insulator substrate. Optics Letters. 2006;**31**:2786-2788. DOI: 10.1364/OL.31.002786

[46] Dong G, Zhou J, Yang X, Cai L. Dual-negative refraction in photonic crystals with hexagonal lattices. Optics Express. 2011;**19**:12119-12124. DOI: 10.1364/OE.19.012119

[47] Dong G, Zhou J, Yang X, Meng X. Precise identification of Dirac-like point through a finite photonic crystal square matrix. Scientific Reports. 2016;**6**:36712. DOI: 10.1038/srep36712

[48] Dong G, Zhou J, Cai L. Zero phase delay induced by wavefront modulation in photonic crystals. Physical Review B. 2012;**87**:125107. DOI: 10.1103/PhysRevB.87.125107

[49] Yun S, Jiang Z, Xu Q, Liu Z, Werner D, Mayer T. Low-loss impedance-matched optical metamaterials with zero-phase delay. ACS Nano. 2012;**6**:4475. DOI: 10.1021/nn3012338

[50] Zhang F, Houzet G, Lheurette E, Lippens D, Chaubet M, Zhao X. Negative-zero-positive metamaterial with omega-type metal inclusions. Journal of Applied Physics. 2008;**103**:084 312. DOI: 10.1063/1.2910831

[51] Alù A, Silveirinha MG, Salandrino A, Engheta N. Epsilon-near-zero metamaterials and electromagnetic sources: Tailoring the radiation phase pattern. Physical Review B. 2007;**75**: 155410. DOI: 10.1103/PhysRevB.75.155410

[52] Mocella V, Cabrini S, Chang A, et al. Self-collimation of light over millimeter-scale distance in a quasi-zero-average-index metamaterial. Physical Review Letters. 2009;**102**:133902. DOI: 10.1103/PhysRevLett.102.133902

[53] Silveirinha M, Engheta N. Tunneling of electromagnetic energy through subwavelength channels and bends using epsilon-near-zero materials. Physical Review Letters. 2006;**97**:157403. DOI: 10.1103/PhysRevLett.97.157403

[54] Belov P, Zhao Y, Tse S, et al. Transmission of images with subwavelength resolution to distances of several wavelengths in the microwave range. Physical Review B. 2008;**77**:193 108. DOI: 10.1103/PhysRevB.77.193108

[55] Podolskiy V, Pollard R, Murphy A, et al. Optical nonlocalities and additional waves in epsilon-near-zero metamaterials. Physical Review Letters. 2009;**102**:127405. DOI: 10.1103/ PhysRevLett.102.127405

[56] Edwards B, Alù A, Young M, Silveirinha M, Engheta N. Experimental verification of epsilon-near-zero metamaterial coupling and energy squeezing using a microwave waveguide. Physical Review Letters. 2008;**100**:033903. DOI: 10.1103/PhysRevLett.100.033903

[57] Kocaman S, Aras M, Hsieh P, et al. Zero phase delay in negative-refractive-index photonic crystal superlattices. Nature Photonics. 2011;**5**:499-505. DOI: 10.1038/nphoton.2011.129

[58] Huang X, Lai Y, Hang Z, Zheng H, Chan C. Dirac cones induced by accidental degeneracy in photonic crystals and zero-refractive-index materials. Nature Materials. 2011;**10**:582. DOI: 10.1038/nmat3030

[59] D'Aguanno G, Mattiucci N, Conti C, Bloemer M. Field localization and enhancement near the Dirac point of a finite defectless photonic crystal. Physical Review B. 2013;**87**:085135. DOI: 10.1103/PhysRevB.87.085135

[60] Chan C, Hang Z, Huang X. Dirac dispersion in two-dimensional photonic crystals. Advances in OptoElectronics. 2012;**2012**:313984. DOI: 10.1155/2012/313984

[61] Zandbergen S, de Dood M. Experimental observation of strong edge effects on the pseudodiffusive transport of light in photonic graphene. Physical Review Letters. 2010;**104**:043903. DOI: 10.1103/PhysRevLett.104.043903

IntechOpen

Chapter 3

Dispersion Properties of TM and TE Modes of Gyrotropic Magnetophotonic Crystals

Alexander A. Shmat'ko, Viktoria N. Mizernik, Eugene N. Odarenko and Viktor T. Lysytsya

Additional information is available at the end of the chapter

http://dx.doi.org/10.5772/intechopen.71273

Abstract

This chapter discusses the propagation of TM and TE waves in the one-dimensional gyrotropic magnetophotonic crystals with ferrite and plasma-like layers. Elements of the transfer matrix are calculated in closed analytical form on the base of electrodynamic problem rigorous solution for arbitrary location of the gyrotropic elements on the structure period. Dispersion equation of the layered periodic structure with gyrotropic elements is obtained. Dispersion properties of the structure for TE and TM modes are analyzed for different configurations of magnetophotonic crystals (ferrite and plasma-like layers). Existence areas of transmission bands for surface and bulk waves are obtained. The effect of problem parameters on the dispersion properties of magnetophotonic crystals for TM and TE modes is investigated. Regimes of complete transmission of wave through limited magnetophotonic crystal are analyzed for bulk and surface waves.

Keywords: magnetophotonic crystal, gyrotropic media, dispersion diagrams, TE and TM modes, bulk and surface waves

1. Introduction

Photonic crystals (PCs) are artificial periodic structures with spatially modulated refractive index in one or more coordinates [1, 2]. Their outstanding optical properties are due to the existence of frequency band gaps where the propagation of electromagnetic waves is impossible. Application of these structures became very attractive for modern optoelectronics which uses the various waveguides, resonators, sensors, and other devices on the basis of PC [3, 4]. Moreover, the control of the PC structure characteristics is the important problem that is usually solved using external electric or magnetic fields. These methods of providing controllability are based on the variation of refractive index of special materials such as liquid crystals

and magnetic materials [5, 6]. Since these sensitive materials are anisotropic, then theoretical analysis of their properties is more complicated.

When at least one of the PCs' unit cell components is a magnetically sensitive (gyrotropic) material, they exhibit unique magneto-optical properties and identified as magnetophotonic crystals (MPCs). Investigations of the MPCs are begun for simplest one-dimensional structures [7, 8]. However, one-dimensional MPCs are the basis elements for various active field-controlling applications so far [9, 10]. Changing of the permeability by external magnetic field is one of the main phenomena that allow developing electronically tuned devices in different frequency bands: filters, circulators and so on [11–13].

Along with the properties inherent in conventional PCs, these structures have additional optical and magneto-optical properties which considerably expand their functionality. Kerr effect, Faraday rotation and optical nonlinearity can be enhanced in MPC due to light localization within magnetic multilayer. Magneto-optical system with large Faraday or Kerr rotation can be used for effective optical isolators [14, 15], spatial light-phase modulators [16] and magnetic field and current sensor [17] development. Furthermore, one can obtain stronger enhancement of the magneto-optical phenomena due to resonant effects in the MPCs [18], which characterized by specific polarization properties. Using PCs with magneto-optical layers provides possibility of control of optical bistability threshold in structure based on graphene layer [19]. It should be noted that not only magnetic materials are suitable for MPC. Namely, one-dimensional PC with plasma layers can be tunable by external magnetic field [20].

A number of applications of the MPCs are inspired by their nonreciprocal properties. For example, special spatial structure of the MPC layers provides the asymmetry of dispersion characteristics and, as a result, the effect of unidirectional wave propagation [21]. This phenomenon allows enhancing field amplitude in the MPC without any periodicity defects. In this case, the so-called frozen mode regime occurs instead the defect mode one.

One of the unique properties of gyrotropic materials is the possibility of negative values of material parameters under the certain conditions. Usually, these are so-called single-negative media that are divided into epsilon-negative media (plasma) and mu-negative ones (gyrotropic magnetic materials). The term "double-negative media" or "left-handed materials" is used for media with negative values of both permittivity and permeability and often replaced by term "metamaterials." Application of metamaterials in one-dimensional PC systems results in unusual regularities of bulk and surface wave propagation and is the subject of experimental and theoretical research [22, 23].

Theoretical description of the various types of one-dimensional PCs is usually based on the transfer-matrix method of Abelès [24] that was applied by Yeh et al. to periodic layered media [25]. This method cannot be applied in general case for anisotropic multilayer structures because of mode coupling. However, this is possible in special cases, namely, in two-dimensional model of wave propagation in periodic layered media [26]. This case is considered in this chapter. Such an approach makes it possible to simplify significantly the analysis of physical phenomena in complex layered media with various combinations of gyrotropic and isotropic elements. Moreover using well-known permutation duality principle of Maxwell's

http://dx.doi.org/10.5772/intechopen.71273

equations results in a reduction of unique combinations number. In turn, this allows better understanding of regularities of bulk and surface wave propagation in one-dimensional MPC and finding new modes for applications in modern microwave, terahertz and optical devices.

2. Formulation and solution of the problem for modes of gyrotropic periodic structures

2.1. Basic relationships

We study electromagnetic wave propagation in periodic structure in general case with bigyrotropic layers (one-dimensional MPC) (**Figure 1**). Each of two layers on the structure period $L=a+b$ is an anisotropic medium (plasma or ferrite or their combinations). Their permittivity and permeability are characterized by tensor values of standard form [26]:

$$\overleftrightarrow{\varepsilon}_j = \begin{Vmatrix} \varepsilon_j & -i\varepsilon_{aj} & 0 \\ i\varepsilon_{aj} & \varepsilon_j & 0 \\ 0 & 0 & \varepsilon_{\|j} \end{Vmatrix}, \quad \overleftrightarrow{\mu}_j = \begin{Vmatrix} \mu_j & -i\mu_{aj} & 0 \\ i\mu_{aj} & \mu_j & 0 \\ 0 & 0 & \mu_{\|j} \end{Vmatrix}. \tag{1}$$

For plasma media, the value of the permittivity is tensor, whereas the value of the permeability is scalar. Such media are called electrically gyrotropic. It is opposite for the ferrite media; the permeability is tensor, whereas permittivity is scalar. Such media are usually called magnetically gyrotropic. If the permittivity and permeability are simultaneously described by the tensors (Eq. (1)), such media are called gyrotropic or bigyrotropic. The material parameters included in tensors $\overleftrightarrow{\varepsilon}_j$ and $\overleftrightarrow{\mu}_j$ are defined by the value of the external bias magnetic field $\vec{H}_0 = \vec{z}_0 H_0$, which is directed along Oz axis.

The study of the general case of gyrotropic media with material parameters of form (Eq. (1)) is reasonable, primarily because it allows using the permutation duality principle when obtaining main equations for fields and characteristic Eqs. [26]. According to this principle generalized for gyrotropic media, namely, when simultaneously the substitution of fields

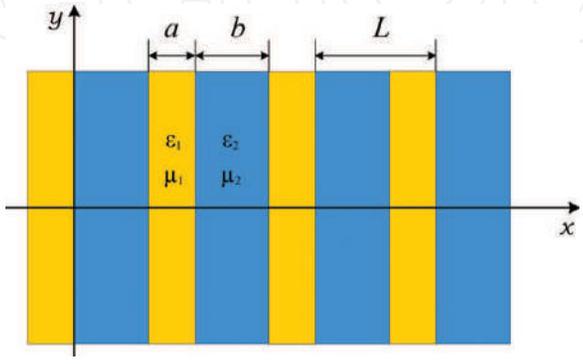

Figure 1: Schematic of the periodic structure.

$\vec{E} \leftrightarrow \vec{H}$ and material parameters $\overleftrightarrow{\varepsilon} \leftrightarrow -\overleftrightarrow{\mu}$ is done, the receiving of general equations, from which the equations for magneto-gyrotropic media (ferrite), electro-gyrotropic media (plasma), and gyrotropic media (bianisotropic media) can be obtained easily, turns to be more simple than in each of the mentioned particular cases separately.

Indeed, it follows from Maxwell equations:

$$rot\ \vec{E} = -\frac{1}{c}\frac{\partial \vec{B}}{\partial t}, \quad rot\ \vec{H} = \frac{1}{c}\frac{\partial \vec{D}}{\partial t}, \tag{2}$$

where $\vec{D} = \overleftrightarrow{\varepsilon}\vec{E}$ is inductance vector of electric field and $\vec{B} = \overleftrightarrow{\mu}\vec{H}$ is inductance vector of magnetic field. Components of these vectors can be written as:

$$D_x = \left(\overleftrightarrow{\varepsilon}\vec{E}\right)_x = \varepsilon E_x - i\varepsilon_a E_y, \quad D_y = \left(\overleftrightarrow{\varepsilon}\vec{E}\right)_y = i\varepsilon_a E_x + \varepsilon E_y, \quad D_z = \left(\overleftrightarrow{\varepsilon}\vec{E}\right)_z = \varepsilon_{\|} E_z,$$

$$B_x = \left(\overleftrightarrow{\mu}\vec{H}\right)_x = \mu H_x - i\mu_a H_y, \quad B_y = \left(\overleftrightarrow{\mu}\vec{H}\right)_y = i\mu_a H_x + \mu H_y, \quad B_z = \left(\overleftrightarrow{\mu}\vec{H}\right)_z = \mu_{\|} H_z.$$

In general case, one can obtain two connected differential equations for longitudinal components of electromagnetic fields E_z and H_z (along Oz axis and the direction of bias magnetic field $\vec{H}_0 = \vec{z}_0 H_0$). In two-dimensional case ($\partial/\partial z = 0$), these equations can be broken up into two independent Helmholtz equations with respect to the selected longitudinal field components E_z and H_z (TM and TE waves) [26]. Indeed, we can show it for two-dimensional case and harmonic dependence $\exp(-i\omega t)$ of the fields on time t.

Using the relation between field components E_z and H_z via transverse field components, one can obtain the Helmholtz equation for two polarizations E_z and H_z, respectively:

$$\frac{\partial^2 E_z}{\partial x^2} + \frac{\partial^2 E_z}{\partial y^2} + k^2 \mu_{\perp} \varepsilon_{\|} E_z = 0, \quad \frac{\partial^2 H_z}{\partial x^2} + \frac{\partial^2 H_z}{\partial y^2} + k^2 \varepsilon_{\perp} \mu_{\|} H_z = 0. \tag{3}$$

Here:

$$\mu_{\perp j} = \mu_j \left(1 - \frac{\mu_{aj}^2}{\mu_j^2}\right), \quad \varepsilon_{\perp j} = \varepsilon_j \left(1 - \frac{\varepsilon_{aj}^2}{\varepsilon_j^2}\right).$$

Eq. (3) describes TM waves (H_x, H_y, E_z), E_z-polarization (s-polarization) and TE waves (E_x, E_y, H_z), H_z-polarization (p-polarization). Therefore, the vector of the electric field for s-polarization is directed perpendicular to the xy plane and the vector of the electric field for the p-polarization is parallel to this plane. It is necessary to use the boundary conditions for the tangential components of the electric and magnetic fields at the media interfaces to solve the boundary electrodynamic problem for the eigenvalues and the eigenfunctions of the Laplace operator. We use the conditions of continuity of the components E_z and H_y for TM waves and H_z and E_y for TE waves.

This analysis shows the important conclusion that in the general case of a gyrotropic medium, the fields of TM and TE waves with respect to the direction of the bias magnetic field $\vec{H}_0$ in the two-dimensional case are divided into two independent solutions of the Maxwell equations. Moreover, Eq. (3) and the expressions for the tangential components of fields E_y and H_y yield the permutation duality principle for the TM and TE waves. These equations are transformed each other after replacing the component of field E_z by H_z, and simultaneously, the effective permeability $\mu_\perp$ should be replaced by the effective permittivity $(-\varepsilon_\perp)$ and $\varepsilon_\parallel$ by $(-\mu_\parallel)$. The boundary conditions for the components E_y and H_y also satisfy the permutation duality principle. Hence, it is possible to simplify this general electrodynamic problem, and we can consider only one type of TM or TE waves for any kind of media in order to obtain a solution for another type of wave. Below, we consider the propagation of E_z-polarized (TM) waves in a gyrotropic PC structure.

To determine the eigenvalues and the corresponding eigenfunctions of the two-layer gyromagnetic MPC, we consider Helmholtz equation for the E_z-polarization with the corresponding boundary conditions for the tangential components of the fields E_z and H_y at the interfaces of the periodic structure layers. For the case of H_z-polarization (TE waves), it is necessary to use the permutation duality principle in the solution for TM waves.

The solution of the Helmholtz equation for TM waves for both tangential components of the fields E_z and H_y can be written in the following form:

$$\begin{aligned} E_z^1(x,y) &= \left(a_{n-1}e^{i\xi_1(x-(n-1)L)} + b_{n-1}e^{-i\xi_1(x-(n-1)L)}\right)e^{i\beta y}, \quad b < x-(n-1)L < L \\ H_y^1(x,y) &= \frac{\xi_1}{-k\mu_{\perp 1}}\left(a_{n-1}g_1^+ e^{i\xi_1(x-(n-1)L)} - b_{n-1}g_1^- e^{-i\xi_1(x-(n-1)L)}\right)e^{i\beta y}, \end{aligned} \tag{4}$$

$$\begin{aligned} E_z^2(x,y) &= \left(c_n e^{i\xi_2(x-nL)} + d_n e^{-i\xi_2(x-nL)}\right)e^{i\beta y}, \quad 0 < x-nL < b \\ H_y^2(x,y) &= \frac{\xi_2}{-k\mu_{\perp 2}}\left(c_n g_2^+ e^{i\xi_2(x-nL)} - d_n g_2^- e^{-i\xi_2(x-nL)}\right)e^{i\beta y}. \end{aligned} \tag{5}$$

Here, $n = 1, 2, \ldots$ is a number of the period; $\xi_j = \sqrt{k^2\mu_{\perp j}\varepsilon_{\parallel j} - \beta^2}$ are the transverse wave numbers in gyrotropic layers in the direction of the Ox axis; β is the longitudinal wave number of the MPC; a_n, b_n, c_n, and d_n are the wave amplitudes in the layers; and $g_j^\pm = 1 \pm i\frac{\mu_{aj}}{\mu_j\xi_j}\beta$.

Let us note one feature in the expressions for the electromagnetic fields (Eqs. (4) and (5)). The presence of gyrotropy in the layers ($\mu_{aj} \neq 0$) leads to the fact that the distributions of the amplitude of the fields in the layers differ by factors $g_j^\pm$ for the forward and backward waves, which propagating in the layers along the direction of periodicity.

To find the dispersion equation that relates the longitudinal wave number β with the structure parameters for a given frequency ω, it is necessary to use the boundary conditions on the interfaces of the layers and the Floquet-Bloch theorem [27, 28] for the periodic structure. Using the conditions of continuity of the E_z and H_y components of the fields at the interfaces $x - (n-1)L = 0$ and $x = nL$, we get matrix equations:

$$\begin{pmatrix} a_{n-1} \\ b_{n-1} \end{pmatrix} = \begin{pmatrix} a_{11} & a_{12} \\ a_{21} & a_{22} \end{pmatrix} \begin{pmatrix} c_n \\ d_n \end{pmatrix}, \qquad \begin{pmatrix} c_n \\ d_n \end{pmatrix} = \begin{pmatrix} b_{11} & b_{12} \\ b_{21} & b_{22} \end{pmatrix} \begin{pmatrix} a_n \\ b_n \end{pmatrix}. \tag{6}$$

where

$$a_{11} = \frac{1}{2}\left(g_1^- + \frac{\xi_2}{\xi_1}\frac{\mu_{\perp 1}}{\mu_{\perp 2}} g_2^+\right) e^{-i\xi_2 L}, \quad a_{12} = \frac{1}{2}\left(g_1^- - \frac{\xi_2}{\xi_1}\frac{\mu_{\perp 1}}{\mu_{\perp 2}} g_2^-\right) e^{i\xi_2 L}, \tag{7}$$

$$a_{21} = \frac{1}{2}\left(g_1^+ - \frac{\xi_2}{\xi_1}\frac{\mu_{\perp 1}}{\mu_{\perp 2}} g_2^+\right) e^{-i\xi_2 L}, \quad a_{22} = \frac{1}{2}\left(g_1^+ + \frac{\xi_2}{\xi_1}\frac{\mu_{\perp 1}}{\mu_{\perp 2}} g_2^-\right) e^{i\xi_2 L}. \tag{8}$$

$$b_{11} = \frac{1}{2}\left(g_2^- + \frac{\xi_1}{\xi_2}\frac{\mu_{\perp 2}}{\mu_{\perp 1}} g_1^+\right) e^{i\xi_2 a} e^{-i\xi_1 a}, \quad b_{12} = \frac{1}{2}\left(g_2^- - \frac{\xi_1}{\xi_2}\frac{\mu_{\perp 2}}{\mu_{\perp 1}} g_1^-\right) e^{i\xi_2 a} e^{i\xi_1 a}, \tag{9}$$

$$b_{21} = \frac{1}{2}\left(g_2^+ - \frac{\xi_1}{\xi_2}\frac{\mu_{\perp 2}}{\mu_{\perp 1}} g_1^+\right) e^{-i\xi_2 a} e^{-i\xi_1 a}, \quad b_{22} = \frac{1}{2}\left(g_2^+ + \frac{\xi_1}{\xi_2}\frac{\mu_{\perp 2}}{\mu_{\perp 1}} g_1^-\right) e^{-i\xi_2 a} e^{i\xi_1 a}. \tag{10}$$

Eliminating the coefficients c_n, d_n in the matrix equations (Eq. (6)), we obtain the relation for the coefficients in identical layers for two neighboring periods of the structure:

$$\begin{pmatrix} a_{n-1} \\ b_{n-1} \end{pmatrix} = \begin{pmatrix} a_{11} & a_{12} \\ a_{21} & a_{22} \end{pmatrix} \begin{pmatrix} c_n \\ d_n \end{pmatrix} = \begin{pmatrix} a_{11} & a_{12} \\ a_{21} & a_{22} \end{pmatrix} \begin{pmatrix} b_{11} & b_{12} \\ b_{21} & b_{22} \end{pmatrix} \begin{pmatrix} a_n \\ b_n \end{pmatrix} = \begin{pmatrix} A & B \\ C & D \end{pmatrix} \begin{pmatrix} a_n \\ b_n \end{pmatrix}. \tag{11}$$

The elements of the ABCD matrix are calculated by the rule of multiplying two matrices. Using the Eqs. (7)–(10), we find the elements of the given transfer matrix, namely:

$$A = \left\{ \cos\xi_2 b - i\frac{1}{2}\left[\frac{\xi_1}{\xi_2}\frac{\mu_{\perp 2}}{\mu_{\perp 1}} + \frac{\xi_2}{\xi_1}\frac{\mu_{\perp 1}}{\mu_{\perp 2}} + \frac{\beta^2}{\xi_1\xi_2}\frac{\mu_{\perp 2}}{\mu_{\perp 1}}\left(\frac{\mu_{a1}}{\mu_1} - \frac{\mu_{\perp 1}}{\mu_{\perp 2}}\frac{\mu_{a2}}{\mu_2}\right)^2\right] \sin\xi_2 b \right\} e^{-i\xi_1 a}, \tag{12}$$

$$D = \left\{ \cos\xi_2 b + i\frac{1}{2}\left[\frac{\xi_1}{\xi_2}\frac{\mu_{\perp 2}}{\mu_{\perp 1}} + \frac{\xi_2}{\xi_1}\frac{\mu_{\perp 1}}{\mu_{\perp 2}} + \frac{\beta^2}{\xi_1\xi_2}\frac{\mu_{\perp 2}}{\mu_{\perp 1}}\left(\frac{\mu_{a1}}{\mu_1} - \frac{\mu_{\perp 1}}{\mu_{\perp 2}}\frac{\mu_{a2}}{\mu_2}\right)^2\right] \sin\xi_2 b \right\} e^{i\xi_1 a}, \tag{13}$$

$$B = i\frac{1}{2}\sin\xi_2 b \left\{ -\frac{\xi_2}{\xi_1}\frac{\mu_{\perp 1}}{\mu_{\perp 2}} + \frac{\xi_1}{\xi_2}\frac{\mu_{\perp 2}}{\mu_{\perp 1}}\left[1 - i\frac{\beta}{\xi_1}\left(\frac{\mu_{a1}}{\mu_1} - \frac{\mu_{a2}}{\mu_2}\frac{\mu_{\perp 1}}{\mu_{\perp 2}}\right)\right]^2 \right\} e^{i\xi_1 a}, \tag{14}$$

$$C = -i\frac{1}{2}\sin\xi_2 b \left\{ -\frac{\xi_2}{\xi_1}\frac{\mu_{\perp 1}}{\mu_{\perp 2}} + \frac{\xi_1}{\xi_2}\frac{\mu_{\perp 2}}{\mu_{\perp 1}}\left[1 + i\frac{\beta}{\xi_1}\left(\frac{\mu_{a1}}{\mu_1} - \frac{\mu_{a2}}{\mu_2}\frac{\mu_{\perp 1}}{\mu_{\perp 2}}\right)\right]^2 \right\} e^{-i\xi_1 a}. \tag{15}$$

An important property of the *ABCD* matrix is the unimodularity property, when the ratio between the elements of the matrix is fulfilled: $AD - BC = 1$. Using the expressions for the elements of the matrix *ABCD*, one can show that this condition is satisfied. We note that when ξ_1 is a real number, then the elements of the matrix $A = D^*$ и $B = C^*$ are pairwise conjugate.

The resulting matrix equation (Eq. (11)), which determines the relationship of the unknown coefficients in two identical layers of different periods of the periodic structure and the

Floquet-Bloch theorem, allows us to find the characteristic (dispersion) equation for determining the previously introduced unknown longitudinal wave number β for a wave propagating along gyrotropic layers (along the *Oy* axis) and the Floquet-Bloch wave number *K*. According to the Floquet-Bloch theorem in its matrix formulation, one can obtain

$$\begin{pmatrix} A & B \\ C & D \end{pmatrix} \begin{pmatrix} a_n \\ b_n \end{pmatrix} = e^{-iKL} \begin{pmatrix} a_n \\ b_n \end{pmatrix}. \tag{16}$$

The phase factor e^{-iKL} is the eigenvalue of the transfer-matrix ABCD, which is determined from the characteristic equation:

$$e^{-iKL} = \frac{1}{2}(A+D) \pm i\sqrt{1-\left[\frac{1}{2}(A+D)\right]^2}. \tag{17}$$

The unknown real values of the roots of the characteristic equation have the form:

$$K_{TM}(\beta) = \frac{1}{L}\arccos\left\{ \cos\xi_2 b \cos\xi_1 a - \frac{1}{2}\left[\begin{array}{l} \dfrac{\xi_1}{\xi_2}\dfrac{\mu_{\perp 2}}{\mu_{\perp 1}} + \dfrac{\xi_2}{\xi_1}\dfrac{\mu_{\perp 1}}{\mu_{\perp 2}} + \\ + \dfrac{\beta^2}{\xi_1\xi_2}\dfrac{\mu_{\perp 2}}{\mu_{\perp 1}}\left(\dfrac{\mu_{a1}}{\mu_1} - \dfrac{\mu_{\perp 1}}{\mu_{\perp 2}}\dfrac{\mu_{a2}}{\mu_2}\right)^2 \end{array} \right] \sin\xi_2 b \sin\xi_1 a \right\}. \tag{18}$$

It is easy to show that this expression is transformed to the well-known solution of the dispersion equation for the case of two magnetodielectric layers ($\mu_{a1} = \mu_{a2} = 0$) [25].

Note that the longitudinal wave number enters into equation as β squared. This indicates that its absolute value is the same for opposite directions of wave propagation along the *Oy* axis. That is, the dispersion is the same for forward and backward waves propagating along the layers. However, the field distributions for the case of gyrotropic media in the direction of periodicity for forward and backward waves are different.

Using the permutation duality principle, we found the solutions of the electrodynamic problem for TE wave propagation in the gyrotropic MPC. For this case, we change the material parameters according to the rule $\overleftrightarrow{\mu} \leftrightarrow -\overleftrightarrow{\varepsilon}$ in the transfer-matrix elements (Eqs. (12)–(15)), in the dispersion relation, and in the solution (Eq. (18)). Then, we obtain

$$A_{TE} = \left\{ \cos\xi_2 b - i\frac{1}{2}\left[\frac{\xi_1}{\xi_2}\frac{\varepsilon_{\perp 2}}{\varepsilon_{\perp 1}} + \frac{\xi_2}{\xi_1}\frac{\varepsilon_{\perp 1}}{\varepsilon_{\perp 2}} + \frac{\beta^2}{\xi_1\xi_2}\frac{\varepsilon_{\perp 2}}{\varepsilon_{\perp 1}}\left(\frac{\varepsilon_{a1}}{\varepsilon_1} - \frac{\varepsilon_{\perp 1}}{\varepsilon_{\perp 2}}\frac{\varepsilon_{a2}}{\varepsilon_2}\right)^2\right] \sin\xi_2 b \right\} e^{-i\xi_1 a}, \tag{19}$$

$$D_{TE} = \left\{ \cos\xi_2 b + i\frac{1}{2}\left[\frac{\xi_1}{\xi_2}\frac{\varepsilon_{\perp 2}}{\varepsilon_{\perp 1}} + \frac{\xi_2}{\xi_1}\frac{\varepsilon_{\perp 1}}{\varepsilon_{\perp 2}} + \frac{\beta^2}{\xi_1\xi_2}\frac{\varepsilon_{\perp 2}}{\varepsilon_{\perp 1}}\left(\frac{\varepsilon_{a1}}{\varepsilon_1} - \frac{\varepsilon_{\perp 1}}{\varepsilon_{\perp 2}}\frac{\varepsilon_{a2}}{\varepsilon_2}\right)^2\right] \sin\xi_2 b \right\} e^{i\xi_1 a}, \tag{20}$$

$$B_{TE} = i\frac{1}{2}\sin\xi_2 b \left\{ -\frac{\xi_2}{\xi_1}\frac{\varepsilon_{\perp 1}}{\varepsilon_{\perp 2}} + \frac{\xi_1}{\xi_2}\frac{\varepsilon_{\perp 2}}{\varepsilon_{\perp 1}}\left[1 - i\frac{\beta}{\xi_1}\left(\frac{\varepsilon_{a1}}{\varepsilon_1} - \frac{\varepsilon_{a2}}{\varepsilon_2}\frac{\varepsilon_{\perp 1}}{\varepsilon_{\perp 2}}\right)\right]^2 \right\} e^{i\xi_1 a}, \tag{21}$$

$$C_{TE} = -i\frac{1}{2}\sin\xi_2 b\left\{-\frac{\xi_2}{\xi_1}\frac{\varepsilon_{\perp 1}}{\varepsilon_{\perp 2}}+\frac{\xi_1}{\xi_2}\frac{\varepsilon_{\perp 2}}{\varepsilon_{\perp 1}}\left[1+i\frac{\beta}{\xi_1}\left(\frac{\varepsilon_{a1}}{\varepsilon_1}-\frac{\varepsilon_{a2}}{\varepsilon_2}\frac{\varepsilon_{\perp 1}}{\varepsilon_{\perp 2}}\right)\right]^2\right\}e^{-i\xi_1 a}. \quad (22)$$

Here $\xi_1 = \sqrt{k^2\varepsilon_{\perp 1}\mu_{\parallel 1}-\beta^2}$ and $\xi_2 = \sqrt{k^2\varepsilon_{\perp 2}\mu_{\parallel 2}-\beta^2}$.

It is apparent that in this case, one can write

$$K_{TE}(\beta) = \frac{1}{L}\arccos\left\{\cos\xi_2 b\cos\xi_1 a-\frac{1}{2}\left[\begin{array}{l}\frac{\xi_1}{\xi_2}\frac{\varepsilon_{\perp 2}}{\varepsilon_{\perp 1}}+\frac{\xi_2}{\xi_1}\frac{\varepsilon_{\perp 1}}{\varepsilon_{\perp 2}}+\\ +\frac{\beta^2}{\xi_1\xi_2}\frac{\varepsilon_{\perp 2}}{\varepsilon_{\perp 1}}\left(\frac{\varepsilon_{a1}}{\varepsilon_1}-\frac{\varepsilon_{\perp 1}}{\varepsilon_{\perp 2}}\frac{\varepsilon_{a2}}{\varepsilon_2}\right)^2\end{array}\right]\sin\xi_2 b\sin\xi_1 a\right\}. \quad (23)$$

In the absence of gyrotropy ($\varepsilon_{aj}=0$), this solution is transformed into the well-known expression for the Bloch wave number for TE waves for the magnetodielectric PC [25].

The given elements of the transfer-matrix *ABCD* and the solutions of the dispersion equations (Eqs. (18) and (23)) for both *s*- and *p*-polarizations (TM and TE waves) are suitable for analysis of wide variety of MPCs with different material parameters: two isotropic layers on the crystal period (dielectric, magnetic, magnetodielectric), one isotropic layer with another anisotropic layer, two gyroelectric layers or gyromagnetic ones or a combination of them, and two gyrotropic layers. Such an abundance of variants makes Eq. (17) universal in terms of analyzing the dispersion characteristics of TE and TM waves and establishing the features of their propagation in various one-dimensional MPCs.

2.2. Eigen regimes of MPCs

We perform the analysis of the features for the propagation of the electromagnetic waves in different MPCs for various eigenmodes. We identified 10 variants of such regimes.

1. *The crystal contains two layers of magnetodielectric*: $\varepsilon_{a1}=\varepsilon_{a2}=\mu_{a1}=\mu_{a2}=0$.

2. *The crystal contains magnetodielectric layer,* $\varepsilon_{a1}=\mu_{a1}=0$, *and the layer of a semiconductor plasma*: $\varepsilon_{a2}\neq 0$ and $\mu_{a2}=0$.

3. *The crystal contains magnetodielectric layer,* $\varepsilon_{a1}=\mu_{a1}=0$, *and the ferrite layer:* $\mu_{a2}\neq 0$ and $\varepsilon_{a2}=0$.

Taking into account the permutation duality principle, we obtain equations analogous to variant 2.

4. *The crystal contains magnetodielectric layer and gyrotropic one*: $\varepsilon_{a1}=\mu_{a1}=0$, $\varepsilon_{a2}\neq 0$, and $\mu_{a2}\neq 0$.

5. *The crystal contains layer of semiconductor plasma:* $\varepsilon_{a1}\neq 0$ *and* $\mu_{a1}=0$ *and the ferrite layer*: $\varepsilon_{a2}=0$ and $\mu_{a2}\neq 0$.

6. *The crystal contains two layers of semiconductor plasma*: $\varepsilon_{a1}\neq 0$, $\varepsilon_{a2}\neq 0$ and $\mu_{a1}=0$, $\mu_{a2}=0$.

7. *The crystal contains two ferrite layers*: $\mu_{a1}\neq 0$, $\mu_{a2}\neq 0$ and $\varepsilon_{a1}=0$, $\varepsilon_{a2}=0$.

Taking into account the permutation duality principle, we obtain equations analogous to variant 6.

8. *The crystal contains the plasma layer and gyrotropic layer*: $\varepsilon_{a1} \neq 0$, $\varepsilon_{a2} \neq 0$ and $\mu_{a1} = 0$, $\mu_{a2} \neq 0$.

9. *The crystal contains the ferrite layer and gyrotropic layer*: $\varepsilon_{a1} = 0$, $\varepsilon_{a2} \neq 0$ and $\mu_{a1} \neq 0$, $\mu_{a2} \neq 0$.

Taking into account the permutation duality principle, we obtain equations analogous to variant 8.

10. *The crystal contains two gyrotropic layers* $\mu_{a1} \neq 0$, $\mu_{a2} \neq 0$ and $\varepsilon_{a1} \neq 0$, $\varepsilon_{a2} \neq 0$

In this case, one can use solutions Eqs. (18) and (23) for TM and TE waves, respectively.

3. Analysis of the propagation of TE and TM waves in MPCs

3.1. General aspects of wave propagation in MPCs

Let us do a physical analysis of the obtained results and determine general rules of electromagnetic wave propagation in MPC. If the wave number $K(\beta)$ is real, then the electromagnetic wave propagates in a MPC without attenuation. These particular Floquet-Bloch wave numbers $K(\beta)$ correspond to the transmission bands and satisfy the condition $|\cos K(\beta)L| \leq 1$. On the other hand, a different behavior is observed when the wave number is complex: $K(\beta) = K'(\beta) + iK''(\beta)$. Such waves cannot propagate in a MPC and thus decay along the direction of periodicity. As a result, the forbidden zones are formed that satisfied the condition $|\cos K(\beta)L| > 1$. This condition allows easy determination of the imaginary part $K''(\beta)$ of the wave number. When $K''(\beta) \neq 0$, then $\sin K'(\beta)L = 0$ and $K'(\beta)L = \pi m$ (where $m = 0, 1, 2\ldots$ are forbidden zone numbers). As a result, we can obtain the equation for $K''(\beta)$: $chK''(\beta)L = (-1)^m \frac{1}{2}(A + D)$.

The value $m = 0$ corresponds to the zeroth forbidden zone where the wave number is purely imaginary. It is important to distinguish two cases: the absence ($\varepsilon_{aj} = 0$, $\mu_{aj} = 0$) and presence ($\varepsilon_{aj} \neq 0$, $\mu_{aj} \neq 0$) of gyrotropy in a MPC. Besides of that, if in j^{th} layer the conditions $k^2\varepsilon_{\perp j}\mu_{\parallel j} - \beta^2 < 0$ or $k^2\mu_{\perp j}\varepsilon_{\parallel j} - \beta^2 < 0$ are satisfied, and in one layer $\varepsilon_{\perp 1} < 0$ (or$\mu_{\perp 1} < 0$) and in another layer $\varepsilon_{\perp 2} > 0 (\mu_{\perp 2} > 0)$, then the wave in such layer would decay in amplitude along the x-axis. This wave is a surface wave and delayed in respect to the speed of light.

3.2. Analysis of dispersion characteristics

Let us consider first the case of a MPC in the absence of gyrotropy ($\varepsilon_{aj} = 0$ and $\mu_{aj} = 0$). This structure is a periodic sequence of magnetodielectric layers. Dispersion equations for these structures were previously considered in a simplified version by many authors. However, the first investigation of such characteristic (dispersion) equations was carried out as early as the nineteenth century by Rayleigh [29] in the solution of the one-dimensional Hill equation. If the medium is periodic, then the latter equation becomes the traditional one-dimensional Helmholtz equation. Further investigations were performed by various researchers, for example, Brillouin [30], Yeh et al. [25], and Bass [31].

The solutions of the dispersion equations for the magnetodielectric periodic structures written out in this section include all possible combinations of the signs and magnitudes of the material

parameters. As an example, let us consider dispersion characteristics of one-dimensional magnetodielectric PCs for several combinations of the parameters.

Figure 2 shows dispersion curves for the value of the longitudinal wave number $\beta = 0.9$. In this case, the periodic structure consists of two dielectrics ($\mu_1 = \mu_2 = \mu_{\|} = 1$) with positive values of permittivity $\varepsilon_1 = \varepsilon_{\|1} = 2$ and $\varepsilon_2 = \varepsilon_{\|2} = 9$. The normalized width of the layers is $a/L = 0.8$ and $b/L = 0.2$. Solid and dotted curves denote the real and imaginary parts of the Floquet-Bloch wave number, respectively. The imaginary parts of the Floquet-Bloch wave number characterize the degree of wave decay in the forbidden bands. The wave decay is different in forbidden zones. Moreover, the maximum attenuation is observed for the zeroth zone.

If we consider a MPC consisting of two different magnetodielectrics, then there are no fundamental differences.

Figure 3 shows the dispersion diagrams for PC with two dielectric layers ($\mu_1 = \mu_2 = 1$) on the structure period and with different signs of the permittivities ($\varepsilon_1 > 0$ and $\varepsilon_2 < 0$), namely, $\varepsilon_1 = \varepsilon_{\|1} = 2$ and $\varepsilon_2 = \varepsilon_{\|2} = -6$. First the problem of wave propagation at the boundary of two half-spaces from dielectrics with opposite signs of permittivity values was considered by Sommerfeld [32].

The existence of surface waves at the boundaries of PC layers is illustrated in the dispersion diagram (**Figure 3**) for TE waves (*p*-polarization). The region of these waves existence is located below the light line $k = \beta(\varepsilon_1)^{-1/2}$ (the solid line on the diagram). Taking into account the identical physical nature of the surface wave existence in PC and Zenneck-Sommerfeld wave for two media [33], this regime can be classified as a modified surface Zenneck-Sommerfeld wave. For this wave, the condition $\beta = k\sqrt{\frac{\varepsilon_1\varepsilon_2}{\varepsilon_1+\varepsilon_2}}$ is satisfied approximately, as follows from the dispersion equation. It should be noted that if we consider PC with magnetic layers, then a surface wave will exist for *s*-polarization.

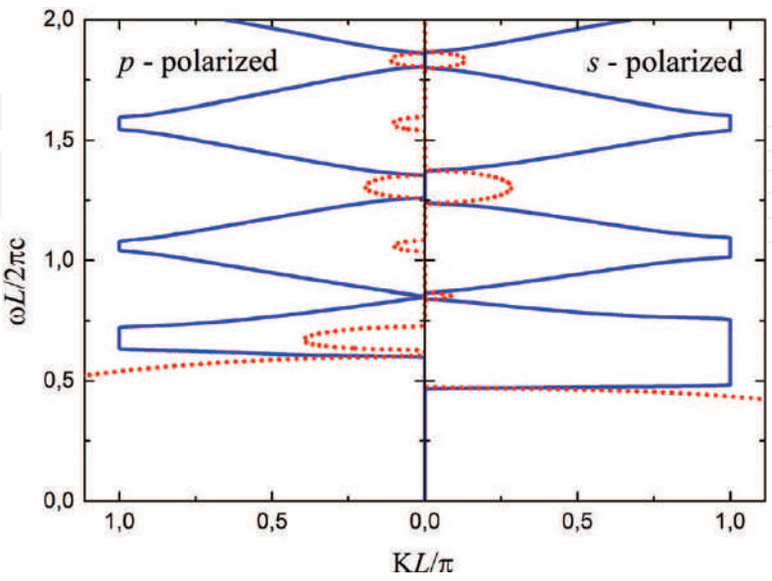

Figure 2: Dispersion characteristics of the one-dimensional photonic crystal.

http://dx.doi.org/10.5772/intechopen.71273

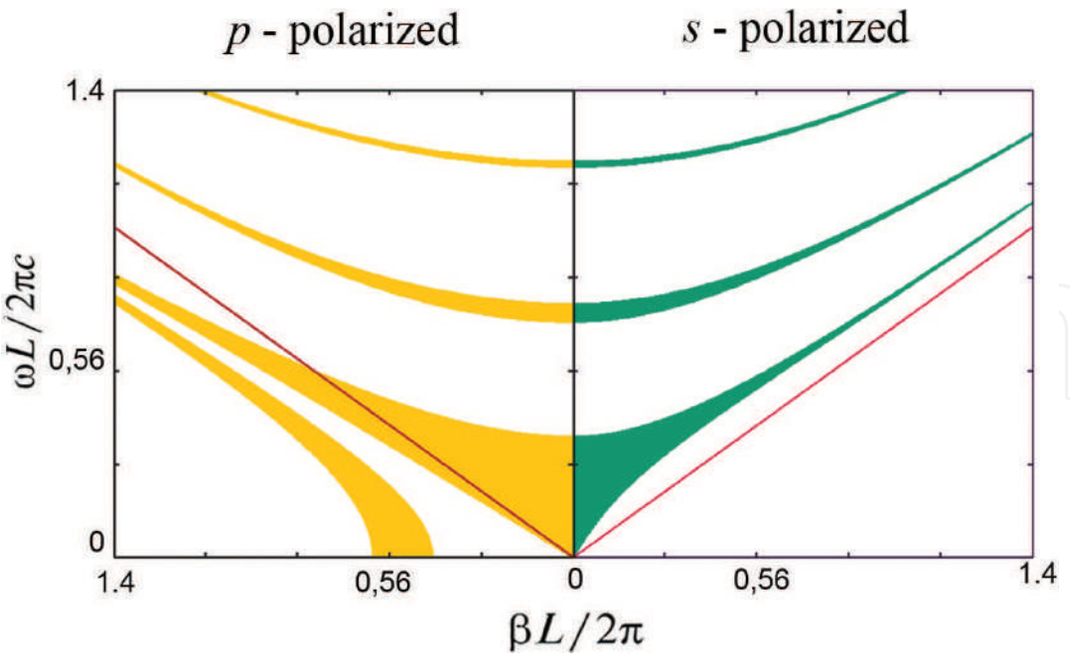

Figure 3. Dispersion diagrams for both polarizations.

With the advent of new artificial media (metamaterials) for which the permittivity and permeability are simultaneously negative, optoelectronics devices with new functionalities are developed. In this connection, it is expedient to consider a MPC, one of whose layers on the structure period is a metamaterial (e.g., $\varepsilon_2 < 0$, $\mu_2 < 0$).

In **Figure 4**, dispersion diagrams are calculated for the one-dimensional PC with alternative layers of magnetodielectric and metamaterial ($\varepsilon_2 < 0$, $\mu_2 < 0$). The following parameters were

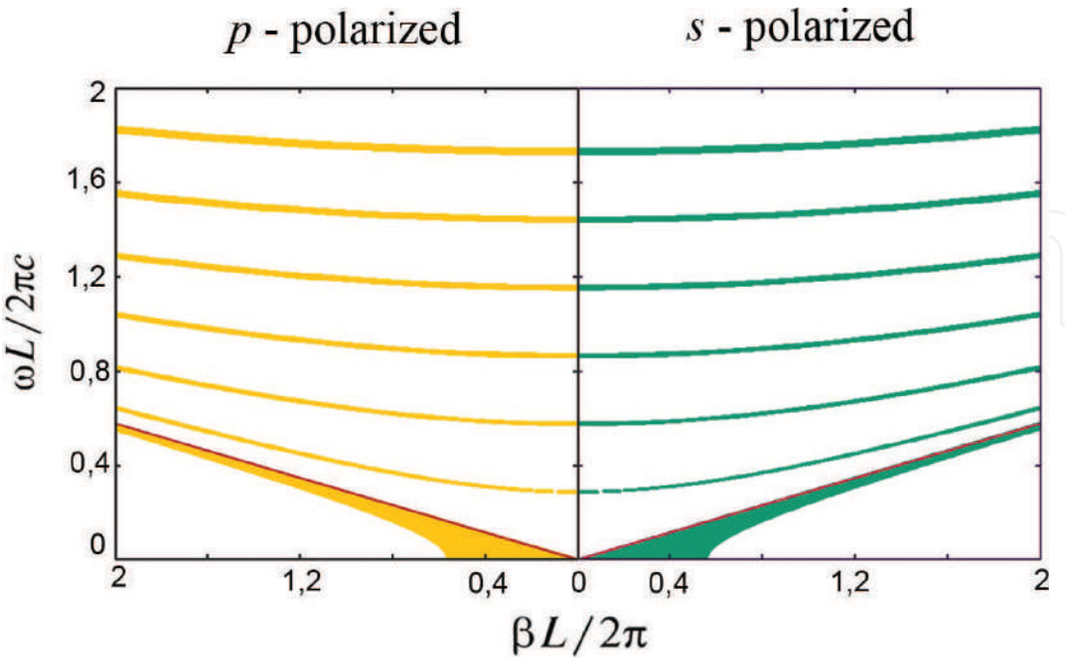

Figure 4. Dispersion diagram of the photonic crystal with metamaterial layer.

selected: $\varepsilon_1 = 4$, $\mu_1 = 3$, $\varepsilon_2 = -2$, $\mu_2 = -6$, and $a/L = 0.5$. **Figure 5a** and **b** shows the dispersion characteristics for such MPC at the values $\beta = 0$ and $\beta = 2\pi/L$, respectively. On the presented graphs, identical dispersion diagrams for both polarizations are seen. Therefore, it is a case of polarization indifference for the forbidden zones and transmission ones. For the presented case, the refractive indices of the layers are the same in absolute value and have phase difference of π, namely, $n_1 = \sqrt{\varepsilon_1 \mu_1} = \sqrt{12}$ and $n_2 = \sqrt{|\varepsilon_2| e^{-i\pi} |\mu_2| e^{-i\pi}} = e^{-i\pi}\sqrt{12}$. For this case, the complete Floquet-Bloch wave transmission in PC for two polarizations is possible.

It is clear that there are transmission bands only for surface slow waves (modified Zenneck-Sommerfeld waves) that are located below the light line $\omega\sqrt{12} = \beta c$. For bulk waves ($k^2\varepsilon_j\mu_j > \beta^2$), the transmission bands degenerate into curves. These curves are described by equation $(2\pi m)^2 = (k^2|\varepsilon_j\mu_j| - \beta^2)L^2$ ($m = 1, 2, \ldots$) for both polarizations.

Dispersion curves for real K' and imaginary K'' values (**Figure 5a** and **b**) show that the wave decay for both polarizations is the same. The propagation of waves is observed at discrete points on which the conditions $K'' = 0$ and $|\cos K(\beta)L| = 1$ are satisfied. These points are located outside the transmission bands of surface waves. The phenomenon of polarization indifference makes it possible to develop devices with a finite number of periods of a MPC in which a complete narrow-band propagation of the wave is possible simultaneously for a whole spectrum of discrete frequencies and both polarizations [34].

We now turn to an analysis of the propagation of waves in MPC consisting of a magnetodielectric and a semiconductor plasma layer [35]. It is advisable to consider two cases in the presence of gyrotropy of the medium ($\varepsilon_{a2} \neq 0$), when $\varepsilon_{\perp 2} > 0$ and $\varepsilon_{\perp 2} < 0$ for TE waves. We note that the dispersion characteristics for TM waves are the same as for a conventional magnetodielectric. Let us first consider the features of TE wave propagation in MPC when the plasma layer gyrotropy is such that condition $\varepsilon_{\perp 2} > 0$ ($\varepsilon_{a2} < \varepsilon_2$) is fulfilled. From an analysis of the solutions of the dispersion equation, it follows that in the periodic structure at such a value of the effective permittivity of a plasma medium, there can exist two modes of TE wave propagation. The first

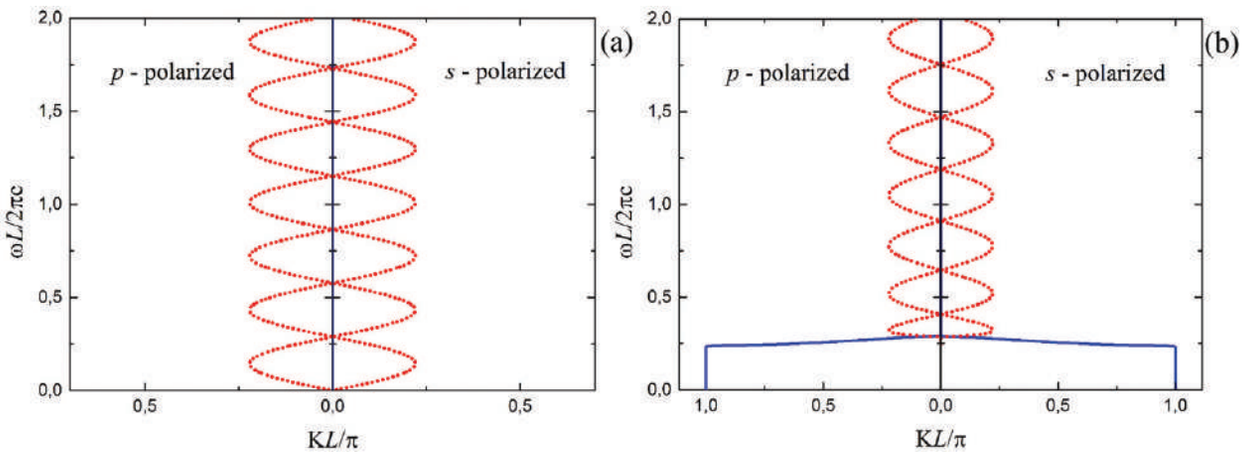

Figure 5. Dispersion characteristics for different values of longitudinal wavenumber: (a) $\beta = 0$; (b) $\beta = 2\pi/L$.

http://dx.doi.org/10.5772/intechopen.71273

mode is bulk waves whose domain of existence is determined by the simultaneous fulfillment of two conditions: $k^2\varepsilon_{\perp 1}\mu_{\parallel 1}-\beta^2>0$ and $k^2\varepsilon_{\perp 2}\mu_{\parallel 2}-\beta^2>0$. The second mode is the propagation mode of gyrotropic surface waves. This mode is observed when three conditions are fulfilled simultaneously: $k^2\varepsilon_{\perp 1}\mu_{\parallel 1}-\beta^2<0$, $k^2\varepsilon_{\perp 2}\mu_{\parallel 2}-\beta^2<0$, and $\frac{\xi_1}{\xi_2}\frac{\varepsilon_{\perp 2}}{\varepsilon_1}+\frac{\xi_2}{\xi_1}\frac{\varepsilon_1}{\varepsilon_{\perp 2}}+\frac{\beta^2}{\xi_1\xi_2}\frac{\varepsilon_1}{\varepsilon_{\perp 2}}\left(\frac{\varepsilon_{a2}}{\varepsilon_2}\right)^2<0$.

If the above conditions are satisfied, then the existence of real values of the Floquet-Bloch wave number other than zero is possible when the condition $|\cos K(\beta)L|\le 1$ is fulfilled for pure imaginary values of transverse wave numbers ξ_1 and ξ_2.

The results of calculations of the dispersion diagram are shown in **Figure 6**. The calculation was carried out with the following parameters: $a/L=0.8$, $\mu_1=\mu_2=\mu_{\parallel 1}=\mu_{\parallel 2}=1$, $\varepsilon_1=2$, $\varepsilon_2=4$, $\varepsilon_{a2}=3.2$, and $\varepsilon_{\perp 2}=1.44$. The solid line shows the light line for the first layer on the period of the structure. It can be seen from the figure that when the conditions$k\sqrt{\varepsilon_{\perp 2}\mu_{\parallel 2}}<\beta$, $k\sqrt{\varepsilon_1\mu_{\parallel 1}}<\beta$, and $\frac{\varepsilon_{\perp 2}}{|\varepsilon_{\perp 2}|}\left[\frac{\beta^2}{|\xi_1||\xi_2|}\frac{\varepsilon_1}{|\varepsilon_{\perp 2}|}\left(\frac{\varepsilon_{a2}}{\varepsilon_2}\right)^2-\left(\left|\frac{\xi_1}{\xi_2}\right|\frac{|\varepsilon_{\perp 2}|}{\varepsilon_1}+\left|\frac{\xi_2}{\xi_1}\right|\frac{\varepsilon_1}{|\varepsilon_{\perp 2}|}\right)\right]>0$ are satisfied, there exists a region of real values of the Floquet-Bloch wave number for which the gyrotropic surface wave regime is observed (more shaded area of the transmission zone).

In the case $\varepsilon_{\perp 2}<0$, as for PC with dielectric layers, the regime of a modified Zenneck-Sommerfeld surface wave can exist in MPC. However, in addition to that wave, there is also a gyrotropic surface wave for other parameters of the problem. Indeed, such a wave exists when both transverse wave numbers in two layers are pure imaginary $(\xi_1^2<0,\xi_2^2<0)$. Also under these conditions and $\varepsilon_{\perp 2}<0$, the condition $\frac{\beta^2}{|\xi_1||\xi_2|}\frac{\varepsilon_1}{|\varepsilon_{\perp 2}|}\left(\frac{\varepsilon_{a2}}{\varepsilon_2}\right)^2<\left|\frac{\xi_1}{\xi_2}\right|\frac{|\varepsilon_{\perp 2}|}{\varepsilon_1}+\left|\frac{\xi_2}{\xi_1}\right|\frac{\varepsilon_1}{|\varepsilon_{\perp 2}|}$ must be fulfilled, that is, opposite to the condition for positive values of the second-layer effective permittivity.

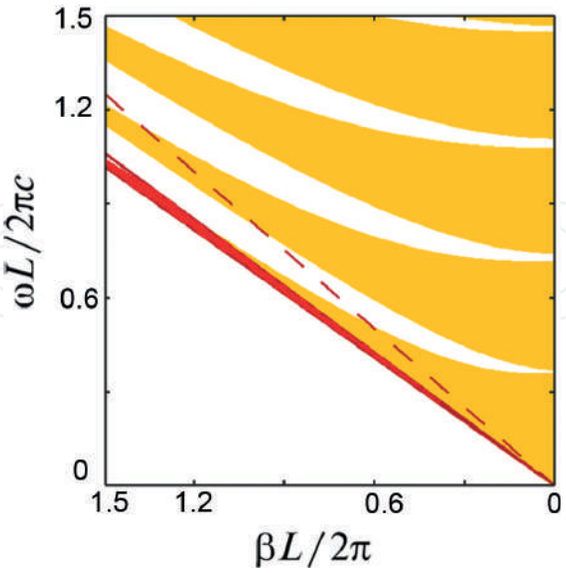

Figure 6. Band structure for TE polarization.

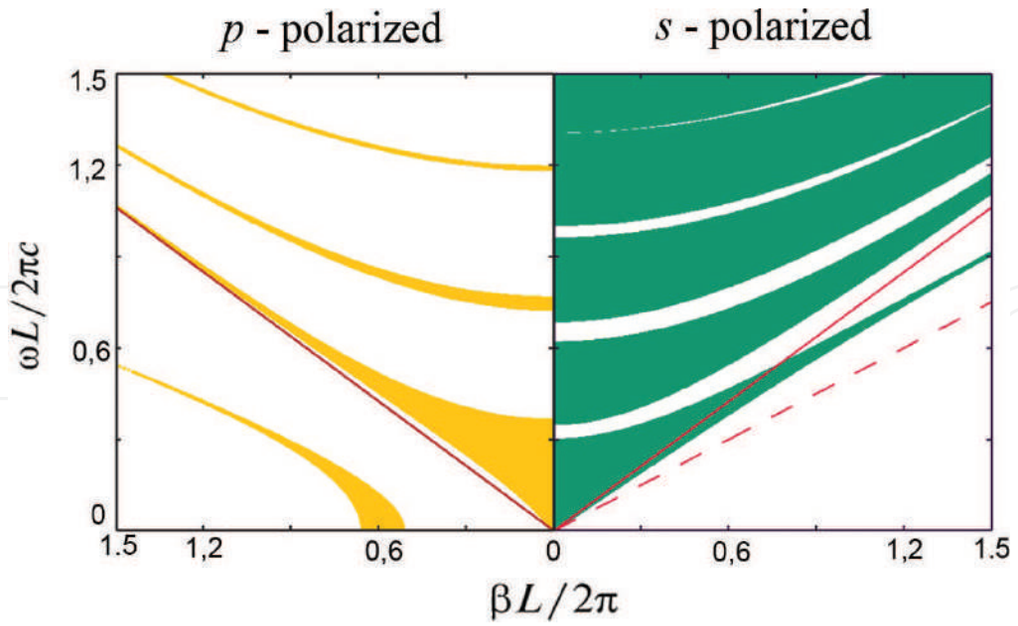

Figure 7. Dispersion diagrams of the magnetophotonic crystal containing plasma layers.

Figure 7 shows the dispersion diagrams for both polarizations in the case $\varepsilon_{\perp 2}<0$. Parameters of the problem were chosen as follows: $a/L=0.8$, $\mu_1=\mu_2=\mu_{\|1}=\mu_{\|2}=1$, $\varepsilon_1=2$, $\varepsilon_2=4$, $\varepsilon_{a2}=6.7$, and $\varepsilon_{\perp 2}=-7.2$. The solid line $k=\beta(\varepsilon_{\perp 1}\mu_{\|1})^{-1/2}$ separates the areas of the existence of bulk waves and surface waves for p-polarization. One area relates to the modified Zenneck-Sommerfeld waves, and the other one relates to the gyrotropic surface wave which also exists for positive values of the effective permittivity, as shown above. We note that in the transmission bands of TE waves in dispersion diagrams, there are two regions in which surface waves propagate.

The case of MPC with a magnetodielectric and ferrite layer is analogous to that considered earlier by virtue of the permutation duality principle. Let us now consider the following case, when both layers on the structure period are ferrite with different material parameters. In this case, modes of bulk wave's existence in the transmission bands can be observed when two conditions $\xi_1^2=k^2\mu_{\perp 1}\varepsilon_{\|1}-\beta^2>0$ and $\xi_2^2=k^2\mu_{2\perp}\varepsilon_{\|2}-\beta^2>0$ are fulfilled. Regime of surface waves is realized when opposite conditions ($\xi_1^2<0$, $\xi_2^2<0$) and also the additional condition are fulfilled:

$$\frac{\mu_{\perp 1}}{|\mu_{\perp 1}|}\frac{\mu_{\perp 2}}{|\mu_{\perp 2}|}\left[\left|\frac{\xi_1}{\xi_2}\right|\left|\frac{\mu_{\perp 2}}{\mu_{\perp 1}}\right|+\left|\frac{\xi_2}{\xi_1}\right|\left|\frac{\mu_{\perp 1}}{\mu_{\perp 2}}\right|-\frac{\beta^2}{|\xi_1\xi_2|}\left|\frac{\mu_{\perp 2}}{\mu_{\perp 1}}\right|\left(\frac{\mu_{a1}}{\mu_1}-\frac{\mu_{\perp 1}}{\mu_{\perp 2}}\frac{\mu_{a2}}{\mu_2}\right)^2\right]<0 \tag{24}$$

Note that this condition is equally suitable for both positive and negative values of the effective magnetic permeability of ferrite $\mu_{\perp j}$. Here, as in the case of the plasma semiconductor layer, the existence of gyrotropic surface waves is possible [36].

In **Figure 8**, we represent the dispersion diagrams of TM waves for the considered above MPC with two ferrite layers at the period of the structure. In the calculation, the following task parameters were chosen: $a/L=0.5$, $\mu_1=\mu_{\|1}=2$, $\mu_2=\mu_{\|2}=3$, $\varepsilon_1=2$, $\varepsilon_2=4$, $\mu_{a2}=2.9$,$\mu_{\perp 2}=0.197\mu_{a1}=0.1$, and $\mu_{\perp 1}=1.995$.

http://dx.doi.org/10.5772/intechopen.71273

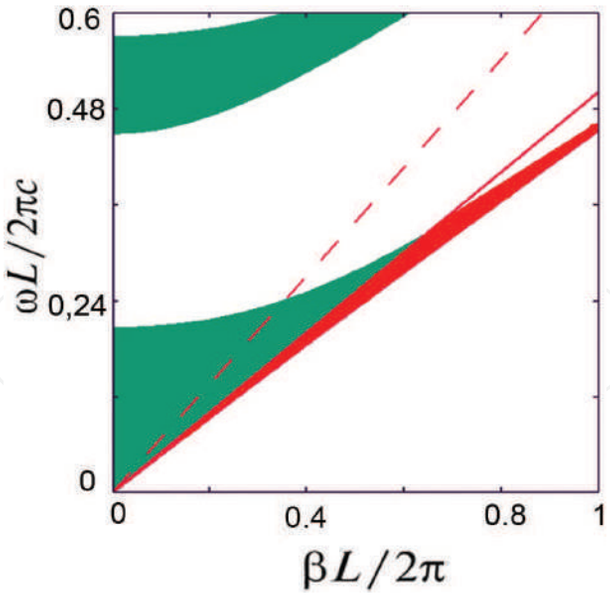

Figure 8. Band structure of the ferrite magnetophotonic crystal.

The solid line in the figure, below which the solutions of the dispersion equation are in the regime of surface waves, is determined by the equation $k=\beta(\mu_{\perp 1}\varepsilon_{\|1})^{-1/2}$. Analysis of the dispersion equation solutions and the conditions for the existence of surface waves show that for the chosen values of the material parameters in the ferrite MPC, there exists a range of parameters on the dispersion diagram that corresponds to the regime of propagation of the surface wave at the boundaries of the layers (in this figure it is marked as more shaded area in transmission zone). We emphasize that the regime of the surface wave is realized with positive values of the both magnetic permeabilities of the ferrite layers.

Figure 9 illustrates the case of the existence of a modified Zenneck-Sommerfeld wave for the case when the effective magnetic permeability of one of the layers is negative. Here, the dispersion diagrams are calculated with the following parameters of the problem: $a/L=0.85$, $\mu_1=\mu_{\|1}=2$, $\mu_2=\mu_{\|2}=3$, $\varepsilon_1=1.5$, $\varepsilon_2=1.8$, $\mu_{a2}=7.9$, $\mu_{\perp 2}=-17.8$, $\mu_{a1}=0.7$, and $\mu_{\perp 1}=1.755$.

Figure 10 illustrates the evolution of dispersion diagrams at change of ferrite effective magnetic permeability $\mu_{\perp 2}(\mu_{a2}=5.6;5.8;6.1)$ for $a/L=0.83$, $\mu_1=\mu_{\|1}=2$, $\mu_2=\mu_{\|2}=3$, $\varepsilon_1=4$, $\varepsilon_2=2$, and $\mu_{a1}=0.4$. A darker shade shows the transmission bands in which the conditions of existence of surface waves are fulfilled. The change of the bias magnetic field value leads to a significant change of the parameters of these areas. An increase in the value of the effective magnetic permeability $\mu_{\perp 2}$ owing to the magnitude μ_{a2} results in a change in the width and location of the transmission band of the modified Zenneck-Sommerfeld surface wave.

Figure 11 shows dispersion diagrams for the modified Zenneck-Sommerfeld surface wave of MPC with two ferrite layers on the structure period at change of width of the layer b ($b/L=0.3;0.5;0.7;0.8$) with $\mu_{\perp 2}<0$ and for the following parameters of the problem: $\mu_1=\mu_{\|1}=2$, $\mu_2=\mu_{\|2}=3$, $\varepsilon_1=4$, $\varepsilon_2=2$, $\mu_{a1}=0.4$, $\mu_{\perp 1}=1.92$, $\mu_{a1}=5.6$, and $\mu_{\perp 2}=-7.45$.

Increase of the second-layer width b leads to an expansion of existence area of surface waves with a simultaneous shift of the bandwidth toward the value $\beta=0$ (**Figure 11a** and **b**). The

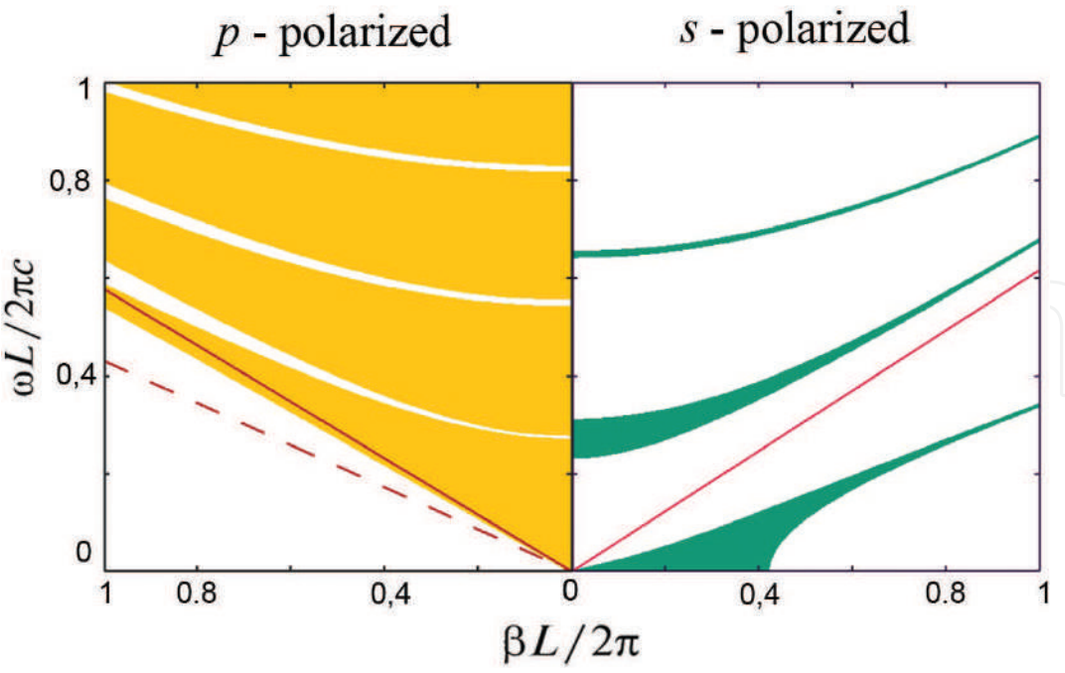

Figure 9. Dispersion diagrams of the ferrite magnetophotonic crystal for both polarizations.

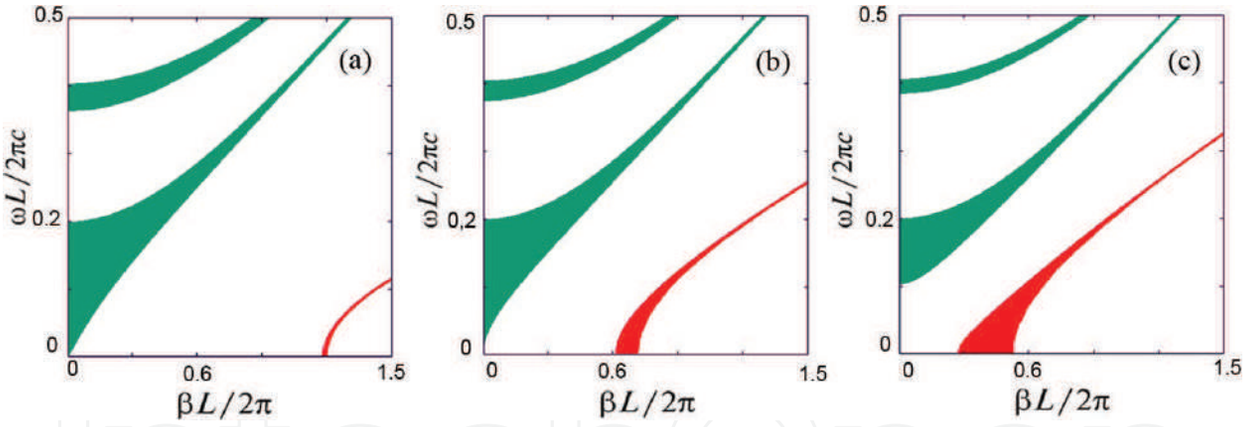

Figure 10. Dispersion diagrams for different values of bias magnetic field: (a) $\mu_{a2}=5.6$; (b) $\mu_{a2}=5.8$; (c) $\mu_{a2}=6.1$.

largest existence area of surface waves is realized in dispersion diagram for approximately equal values of the layer thicknesses. Further increase of the parameter *b* is accompanied by a displacement of this area to the opposite direction (**Figure 11c** and **d**). Thus the surface wave modes in a ferrite MPC are determined both by the material parameters of the system and by the width of the layers on the period of the structure.

Let us move on the dispersion diagrams for two bigyrotropic layers on the structure period. Taking into account the complete symmetry of the dispersion for TE and TM waves, the case of polarization indifference can be realized in this case. We will show this by example.

Figure 12 shows the dispersion diagrams for TE and TM waves for MPC consisting of two bigyrotropic layers on the period of the structure. **Figure 12a** corresponds to the following

http://dx.doi.org/10.5772/intechopen.71273

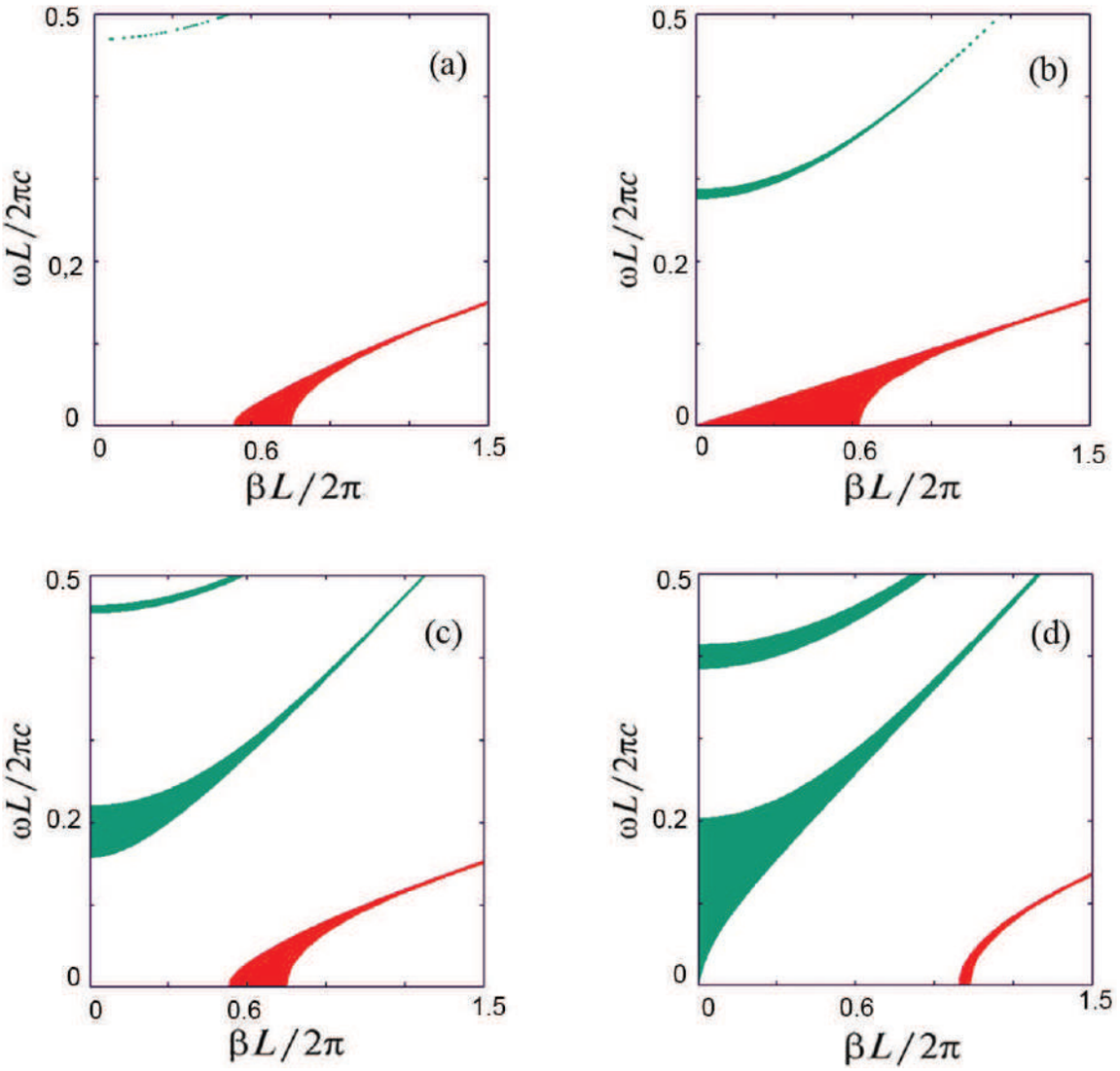

Figure 11. Dispersion diagrams for different values of second layer thickness: (a) $b/L = 0.3$; (b) $b/L = 0.5$; (c) $b/L = 0.7$; (d) $b/L = 0.8$.

values of the parameters: $a/L = 0.85$, $\mu_j = \mu_{\|j} = 2$, $\varepsilon_j = \varepsilon_{\|j} = 2$, $\varepsilon_{a1} = \mu_{a1} = 0.5$, $\varepsilon_{a2} = \mu_{a2} = 5.2$, $\mu_{\perp 1} = 1.875$, and $\mu_{\perp 2} = -11.52$. In **Figure 12b**, only the values of the effective permittivity and permeability of the second layer differ: $\varepsilon_{a2} = \mu_{a2} = 6.8$.

The solid lines in the figures distinguish the area of fast (upper part of figures) and slow wave (the lower part of figures). The complete identity of the dispersion diagrams for the transmission bands of both surface and bulk waves follows from the figures and formulas (18) and (23). By changing the bias magnetic field, it is possible to control the width and location of transmission bands for both polarizations.

Dispersion diagrams in **Figure 13** correspond to the case when only the surface wave transmission bands for both polarizations are realized. The parameters of the problem were chosen as follows: $a/L = 0.28$, $\mu_1 = \mu_{\|1} = 1.5$, $\mu_2 = \mu_{\|2} = 2$, $\varepsilon_1 = \varepsilon_{\|1} = 1.2$, $\varepsilon_2 = \varepsilon_{\|2} = 1.8$, $\varepsilon_{a1} = 4.95$, $\varepsilon_{a2} = 1.7$, $\mu_{a1} = 0.7$, and $\mu_{a2} = 5$. The polarization sensitivity of the MPC is realized in this case. Only the surface waves with certain polarization can propagate through the periodic structure for defined values of parameters k and β.

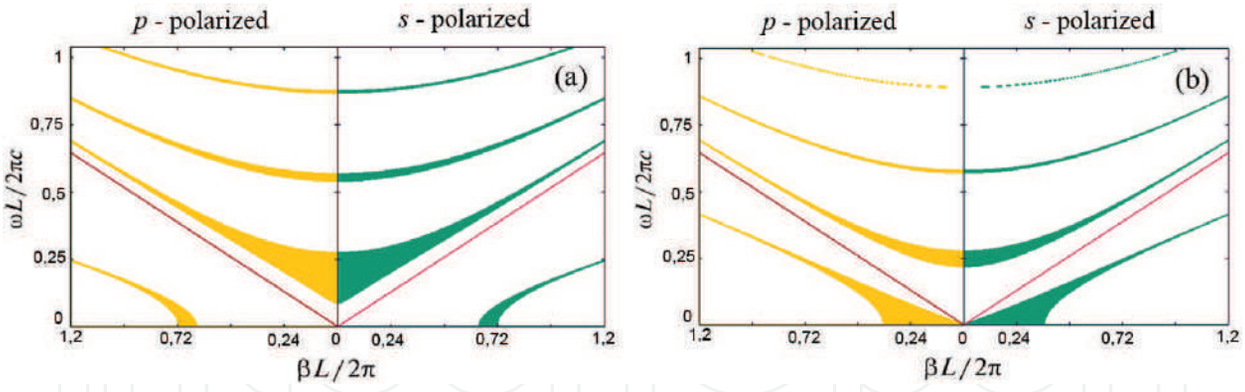

Figure 12. Dispersion diagrams of the bigyrotropic magnetophotonic crystal: (a) $\varepsilon_{a2} = \mu_{a2} = 5.2$; (b) $\varepsilon_{a2} = \mu_{a2} = 6.8$.

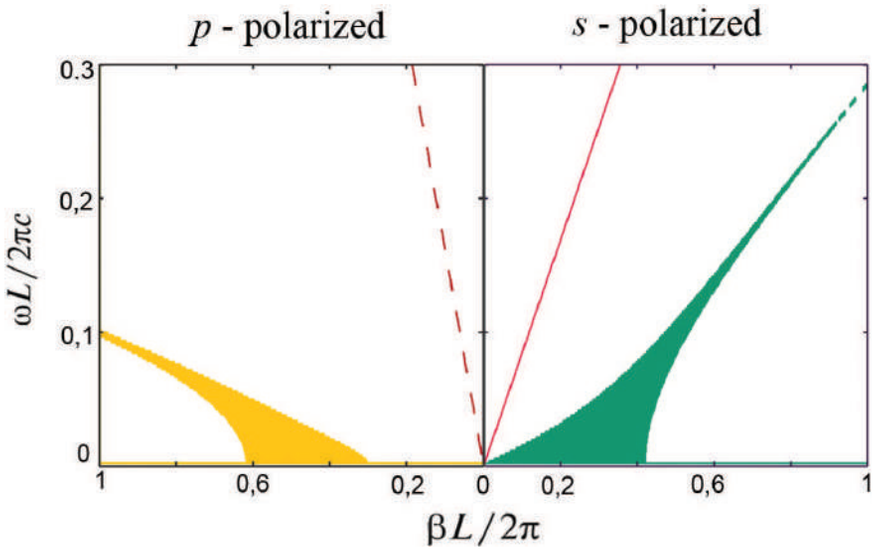

Figure 13. Transmission bands for surface waves in the bigyrotropic magnetophotonic crystal.

Therefore, we have considered the main features of the propagation of TE and TM waves in various magnetophotonic gyrotropic crystals. Important application of this one-dimensional PC theory is the problem of the electromagnetic waves scattering by a structures with limited number of periods.

4. Scattering of a plane wave by a MPC

In this section, the scattering of the plane wave on gyromagnetic MPC with N periods is considered. When a p-polarized plane wave is scattered on MPC with a limited number of periods, the problem is divided into three stages. At the first stage, the problem of scattering of a plane wave on the first gyromagnetic layer of MPC is solved. In the second stage, the coupling between the field coefficients of the first and last layers of the MPC is used in the problem for the MPC modes. And, finally, in the third stage, the problem of wave transmission from the last layer of the structure to the surrounding area is considered. Following

[37], we write out the final expression for the reflection and transmission coefficients for gyrotropic MPC:

$$R = \frac{[(n_{21}M_{11} + n_{22}M_{21})k_{11} + (n_{21}M_{12} + n_{22}M_{22})k_{21}]}{[(n_{11}M_{11} + n_{12}M_{21})k_{11} + (n_{11}M_{12} + n_{12}M_{22})k_{21}]} \tag{25}$$

$$T = \frac{1}{[(n_{11}M_{11} + n_{12}M_{21})k_{11} + (n_{11}M_{12} + n_{12}M_{22})k_{21}]} \tag{26}$$

Here, matrix M is the Nth power of an ABCD matrix. Other notations correspond to Ref. [37]. **Figure 14a** shows the dependences of the transmission coefficient modulus on the normalized frequency in the case of normal wave incidence ($\beta = 0$) on MPC with 20 periods in the regime of bulk waves. Calculation parameters are the same as in **Figure 7**.

There are three transmission bands in the frequency range under consideration. Each of these bands contains resonances which observed with respect to the frequency of the complete transmission of the wave (**Figure 14b** and **c**). Frequency resonances correspond to different modes of the periodic structure. The number of modes is determined by the number of periods of the structure ($N - 1$).

Figure 15 depicts the frequency dependences of the transmission coefficient modulus in the regime of the surface waves. In this case the incident angle of wave is greater than the angle of total internal reflection. We can see one transmission band in this case. Inset in **Figure 15** shows enlarged frequency dependence within this band. Complete propagation is observed for each resonant frequency of modes of the limited periodic structure.

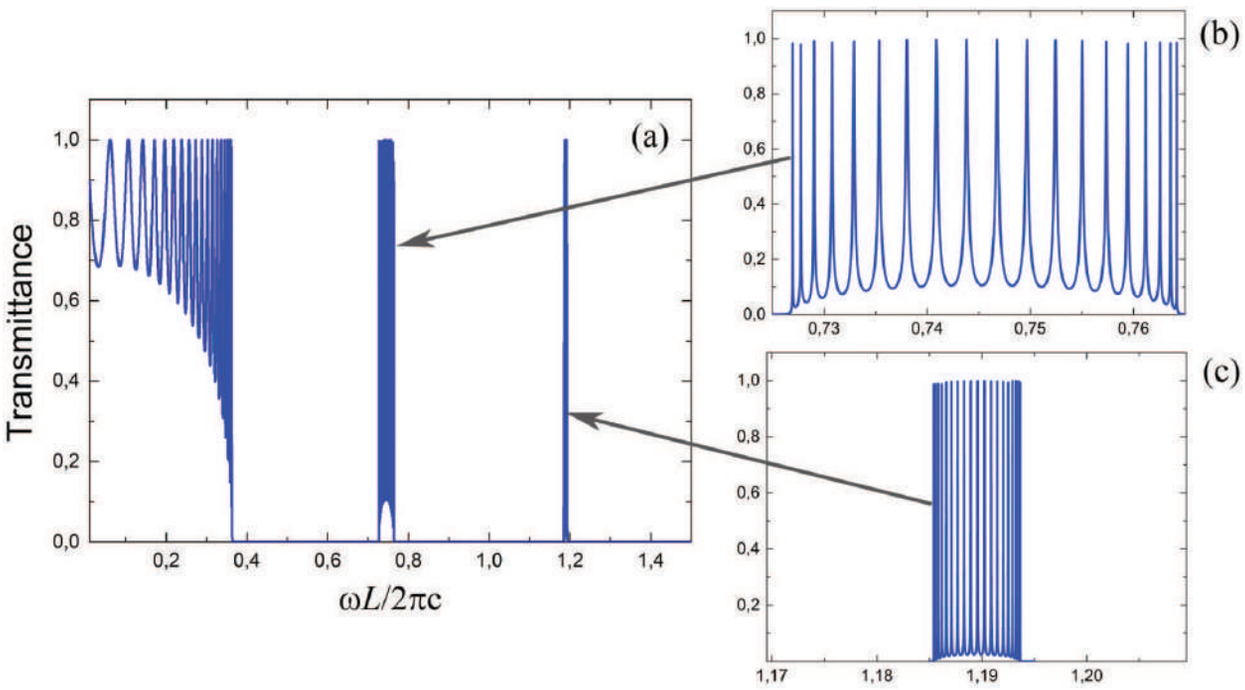

Figure 14. The transmittance vs frequencies for the case of normal incidence of wave: (a) spectral characteristic; (b) fine structure of spectral characteristic in second transmission band; (c) fine structure of spectral characteristic in third transmission band.

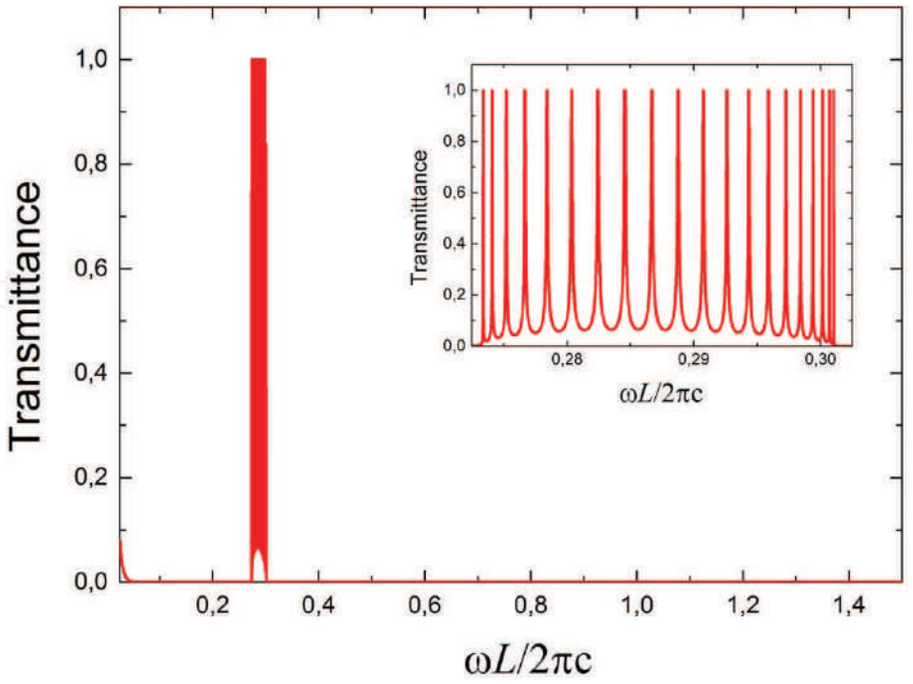

Figure 15. The transmittance vs. frequencies for the case of surface wave mode.

5. Conclusions

The electrodynamic problem is solved for the proper TE and TM waves of a MPC with two gyrotropic layers. The elements of the transmission matrix, the dispersion equation, and its solution are obtained analytically. An analysis of the dispersion properties of TE and TM waves for MPC is carried out, and features of the existence of fast and slow waves are revealed. Different regimes of gyrotropic surface waves are found. The conditions for the existence of surface waves are established for positive and negative values of the permittivity and permeability. Analytic expressions for the reflection and transmission coefficients for a limited MPC are obtained, and their analysis is performed for the regime of bulk and surface waves. Complete transmission of the wave through this structure is realized at resonant frequencies that correspond to different spatial distributions of the mode field in limited MPC.

Author details

Alexander A. Shmat'ko[1], Viktoria N. Mizernik[2], Eugene N. Odarenko[3]* and Viktor T. Lysytsya[1]

*Address all correspondence to: e.n.odarenko@gmail.com

1 V. N. Karazin Kharkiv National University, Kharkiv, Ukraine

2 V. N. Karazin Kharkiv National University, Scientific Physical-Technologic Centre of MES and NAS of Ukraine, Kharkiv, Ukraine

3 V. N. Karazin Kharkiv National University,Kharkiv National University of Radio Electronics, Kharkiv, Ukraine

References

[1] Yablonovitch E. Inhibited spontaneous emission in solid-state physics and electronics. Physical Review Letters. 1987;**58**(20):2059-2062. DOI: 10.1103/PhysRevLett.58.2059

[2] Sakoda K. Optical Properties of Photonic Crystals. 2nd ed. Berlin Heidelberg: Springer-Verlag; 2005. 258 p. DOI: 10.1007/b138376

[3] Lourtioz J-M, Benisty H, Berger V, Gerard J-M, Maystre D, Tchelnokov A. Photonic Crystals. Towards Nanoscale Photonic Devices. 2nd ed. Berlin Heidelberg: Springer-Verlag; 2008. 514 p. DOI: 10.1007/978-3-540-78347-3

[4] Massaro A, editor. Photonic Crystals - Innovative Systems, Lasers and Waveguides. Rijeka, Croatia: InTech; 2012. 358 p. DOI: 10.5772/2632

[5] Busch K, John S. Liquid-crystal photonic-band-gap materials: The tunable electromagnetic vacuum. Physical Review Letters. 1999;**83**(5):967-970. DOI: 10.1103/PhysRevLett.83.967

[6] Inoue M, Levy M, Baryshev AV, editors. Magnetophotonics from Theory to Applications. Berlin Heidelberg: Springer-Verlag; 2013. 228 p. DOI: 10.1007/978-3-642-35509-7

[7] Inoue M, Isamoto K, Yamamoto T, Fujii T. Magneto-optical faraday effect of discontinuous magnetic media with a one-dimensional array structure. Journal of Applied Physics. 1996;**79**(3):1611-1624. DOI: 10.1063/1.361005

[8] Inoue M, Arai K, Fujii T, Abe M. One-dimensional magnetophotonic crystals. Journal of Applied Physics. 1999;**85**(8):5768-5770. DOI: 10.1063/1.370120

[9] Lyubchanskii IL, Dadoenkova NN, Lyubchanskii MI, Shapovalov EA, Rashing T. Magnetic photonic crystals. Journal of Physics D: Applied Physics. 2003;**36**(18):R277-R287. DOI: 10.1088/0022-3727/36/18/R01

[10] Inoue M, Fujikawa R, Baryshev A, Khanikaev A, Lim PB, Uchida H, et al. Magnetophotonic crystals. Journal of Physics D: Applied Physics. 2006;**39**(8):R151-R161. DOI: 10.1088/0022-3727/39/8/R01

[11] Chernovtsev SV, Belozorov DP, Tarapov SI. Magnetically controllable 1D magnetophotonic crystal in millimetre wavelength band. Journal of Physics D: Applied Physics. 2007;**40**(2): 295-299. DOI: 10.1088/0022-3727/40/2/001

[12] Shramkova OV. Transmission properties of ferrite-semiconductor periodic structure. Progress In Electromagnetics Research M. 2009;**7**:71-85. DOI: 10.2528/PIERM09041305

[13] Abdi-Ghaleh R, Namdar A. Circular polarization bandpass filters based on one-dimensional magnetophotonic crystals. Journal of Modern Optics. 2013;**60**(19):1619-1626. DOI: 10.1080/09500340.2013.850540

[14] Aplet LJ, Carson JW. A faraday effect optical isolator. Applied Optics. 1964;**3**(4):544-545. DOI: 10.1364/AO.3.000544

[15] Kato H, Matsushita T, Takayama A, Egawa K, Nishimura M, Inoue M. Properties of one-dimensional Magnetophotonic crystals for use in optical isolator devices. IEEE Transactions on Magnetics. 2002;**38**(5):3246-3248. DOI: 10.1109/TMAG.2002.802511

[16] Chung KH, Kato T, Mito S, Takagi H, Inoue M. Fabrication and characteristics of one-dimensional magnetophotonic crystals for magneto-optic spatial light phase modulators. Journal of Applied Physics. 2010;**107**(9):09A930. DOI: 10.1063/1.3353020

[17] Vasiliev M, Kotov VA, Alameh KE, Belotelov VI, Zvezdin AK. Novel magnetic photonic crystal structures for magnetic field sensors and visualizers. IEEE Transactions on Magnetics. 2008;**44**(3):323-328. DOI: 10.1109/TMAG.2007.914675

[18] Romodina MN, Soboleva IV, Musorin AI, Nakamura Y, Inoue M, Fedyanin AA. Bloch-surface-wave-induced Fano resonance in magnetophotonic crystals. Physical Review B. 2017;**96**(8):081401(R). DOI: 10.1103/PhysRevB.96.081401

[19] Ardakani AG, Firoozi FB. Highly tunable bistability using an external magnetic field in photonic crystals containing graphene and magnetooptical layers. Journal of Applied Physics. 2017;**121**(2):023105. DOI: 10.1063/1.4973897

[20] Mehdian H, Mohammadzahery Z, Hasanbeigi A. Magneto-optical properties of one-dimensional conjugated photonic crystal heterojunctions containing plasma layers. Applied Optics. 2015;**54**(26):7949-7956. DOI: 10.1364/AO.54.007949

[21] Figotin A, Vitebskiy I. Electromagnetic unidirectionality in magnetic photonic crystals. Physical Review B. 2003;**67**(16):165210. DOI: 10.1103/PhysRevB.67.165210

[22] Chen Y, Wang X, Yong Z, Zhang Y, Chen Z, He L, et al. Experimental investigation of photonic band gap in one-dimensional photonic crystals with metamaterials. Physics Letters A. 2012;**376**(16):1396-1400. DOI: 10.1016/j.physleta.2012.01.044

[23] Aylo R, Nehmetallah G, Li H, Banerjee PP. Multilayer periodic and random metamaterial structures: Analysis and applications. IEEE Access. 2014;**2**:437-450. DOI: 10.1109/ACCESS.2014.2321661

[24] Abelès F. Recherches sur la propagation des ondes électromagnétiques sinusoïdales dans les milieux stratifiés. Annales de Physique. 1950;**12**(5):596-640 & 706-782. DOI: 10.1051/anphys/195012050596

[25] Yeh P, Yariv A, Hong C-S. Electromagnetic propagation in periodic stratified media. I. General theory. Journal of the Optical Society of America. 1977;**67**(4):423-438. DOI: 10.1364/JOSA.67.000423

[26] Gurevich AG. Ferrites at Microwave Frequencies. New York: Consultants Bureau; 1963 329 p

[27] Floquet G. Sur les équations différentielles linéaires à coefficients périodiques. Annales scientifiques de l'École Normale Supérieure. 1883;**12**:47-88

[28] Bloch F. Über die Quantenmechanik der Elektronen in Kristallgittern. Zeitschrift für Physik A. 1929;**52**(7–8):555-600. DOI: 10.1007/BF01339455

[29] Rayleigh L. On the maintenance of vibrations by forces of double frequency, and on the propagation of waves through a medium endowed with a periodic structure. Philosophical Magazine S. 5. 1887;**24**(147):145-159

[30] Brillouin L. Wave Propagation in Periodic Structures. New York, London: McGraw-Hill Book Company; 1946 247 p

[31] Bass FG, Bulgakov AA. Kinetic and Electrodynamic Phenomena in Classical and Quantum Semiconductor Superlattices. New York: Nova Science Publishers; 1997 498 p

[32] Sommerfeld A. Ueber die Fortpflanzung elektrodynamischer Wellen längs eines Drahtes. Annals of Physics. 1899;**303**(2):233-290. DOI: 10.1002/andp.18993030202

[33] Zenneck J. Über die Fortpflanzung ebener elektromagnetischer Wellen längs einer ebenen Leiterfläche und ihre Beziehung zur drahtlosen Telegraphie. Annals of Physics. 1907;**328** (10):846-866. DOI: 10.1002/andp.19073281003

[34] Li J, Zhou L, Chan CT, Sheng P. Photonic band gap from a stack of positive and negative index materials. Physical Review Letters. 2003;**90**(8):083901. DOI: 10.1103/PhysRevLett.90.083901

[35] Shmat'ko AA, Mizernik VN, Odarenko EN, Yampol'skii VA, Rokhmanova TN, Galenko A. Yu. Dispersion properties of a one-dimensional anisotropic magnetophotonic crystal with a gyrotropic layer. In: Advanced optoelectronics and lasers (CAOL), IEEE 7th International Conference on; 12–15 Sept.; Odessa, Ukraine. 2016. p. 123-125. DOI: 10.1109/CAOL.2016.7851399

[36] Mizernik V. N, Shmat'ko A. A. Surface Magnon-Polariton modes in the open transmission resonator partially filled ferrite. In: 20th Int. Crimean Conference "Microwave and Telecommunication Technology"; 13–17 Sept.; Sevastopol, Ukraine. 2010. p. 643-644. DOI: 10.1109/CRMICO.2010.5632685

[37] Shmat'ko A.A., Mizernik V.N., Odarenko E.N., Rokhmanova T.N. Bragg reflection and transmission of light by one-dimensional Gyrotropic Magnetophotonic crystal. In: Advanced Information and Communication Technologies (AICT-2017) 2nd International Conference on; 4–7 July; Lviv, Ukraine. 2017. p. 1-5